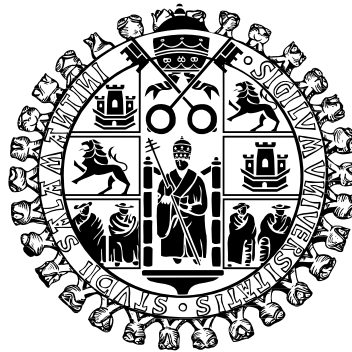# Ultrafast Laser Microprocessing of Transparent Dielectrics

New Schemes for the Fabrication of Photonic Devices

Gabriel Roberto Castillo Vega

Applied Physics Department
Universidad de Salamanca

This dissertation is submitted for the degree of
Doctor in Physics

July 2017

Abstract

Ultrafast laser microprocessing of transparent materials has attracted an increasing research interest due to the unique properties of laser-matter interaction at ultrashort time scales. In particular, the possibility to produce controlled local modifications of the refractive index in dielectrics opened the door to the microfabrication of 3D integrated photonic circuits. In this work, new strategies for the optimization of the techniques for the fabrication of optical waveguides in crystalline materials as well as as for their characterization are presented. The use of these strategies is a contribution to the technological development for the fabrication of integrated complex photonic devices. The fabricated photonic structures are based on Type II modifications in crystals and different techniques were used such as *Stressed induced waveguides* and *Depressed cladding waveguides*. In the case of stressed induced waveguides a new approach in which an interferometer was used to generate two femtosecond laser beams that, focused with certain lateral separation inside the crystal, produced two simultaneous parallel damage tracks with a single scan. On the other hand, the fabrication of waveguides arrays based on depressed cladding waveguides is presented. The arrays consist of divergent hexagonal waveguides with different separations between the waveguides at the exit of the crystal. The results show a good performance of the fabricated structures and suggest a promising potential use in photonic applications such as photonic lanterns, which can be easily implemented in other transparent materials. It is also presented a novel kind of structures called photonic lattice-like structures which emulates in shape, the photonic crystal fibers. These structures present attractive characteristics such the fact of being able to manipulate the cross section along the waveguide by introducing axial defects which allows beam manipulation in a controlled and reproducible manner. This important characteristic offers the possibility of fabricate monolithic structures. A study of the ultrafast laser-induced modifications of femtoseconds pulses in the nanostructured polycrystalline YSZ ceramic, a very promising material for bio-medical applications, as well as the study and the integration of optical waveguides in this material is also presented. In addition, properties such as the ablation threshold and the nonlinear optical properties were characterized. Finally, a preliminary study of the temporal features of ultrashort pulses propagating to different types of waveguides is presented.

Table of contents

List of figures

List of tables

Chapter 1

Introduction

1.1 What is ultrafast laser microprocessing?

Ultrafast laser microprocessing is a process by which pulses from a femtosecond laser, also known as ultrafast laser, are used to micro-structure the surface or the bulk (inside) of solid materials. One of the most interesting features of this kind of lasers is the high peak intensities that can be reach when are tightly focused. These intensities are in the range of 10^{12} - 10^{15} W/cm^2 which can easily induce nonlinear absorption in transparent materials. Therefore, if the focus is set inside a transparent material (see Fig. 1.1) the nonlinear absorption can be confined to a region near to the focal volume allowing ultrahigh precision modifications and 3D microprocessing of the material [1]. In particular, the interaction of femtosecond pulses with transparent dielectrics has attracted a lot of interest in the last two decades mainly due to the possibility to induce localized refractive index changes to create complex photonic structures inside the material keeping the surface intact [2–14]. Nowadays, this technique is known as **Ultrafast laser inscription** (ULI) and is has been consolidated as a three dimensional (3D) photonic device fabrication technology. In this section a brief review of the state of the art is introduced, besides the scientific and technical aspects that have motivated the present work as well as the basis of the objectives that has been set to achieve.

1.2 Motivation and background

Ultrafast laser inscription is characterized by an energy transference from the strong optical field of the laser to the material through a process known as optical breakdown [16] which causes the ionization of a large number of electrons. As a result, the energy acquired by the electrons is transferred to the material. As this energy is deposited and converted to thermal energy, the
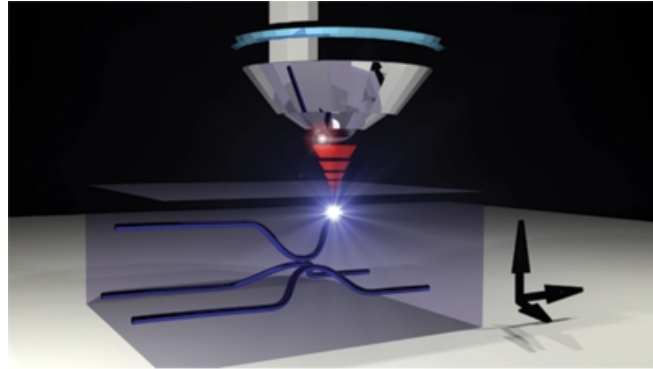
Fig. 1.1 Schematic image of ultrafast laser inscription process; nonlinear absorption occurs at the laser focus, resulting in highly localized energy deposition. 3D photonic structures can be fabricated inside a transparent material [15].

material may undergo structural or phase modifications, leaving behind local changes such as the refractive index. This principle was used by Davis et al. in [2] to inscribe for the first time an optical waveguide inside a transparent material by direct femtosecond laser irradiation. For this purpose, they focused the laser beam inside a sample of fused silica and it was moved with respect to the focus, thus generating a trace in which positive contrast of the refractive index had been achieved, and in which light could be coupled and propagated. Since this pioneer work, ultrafast laser inscription spread to a variety of transparent materials [17–24]. Since then research and development with regard to the fabrication of photonic devices based in optical waveguides has rapidly advanced until today.

In general, two main types of modifications can be induced in transparent dielectrics by the irradiation with femtosecond pulses that can be exploited for waveguide fabrication. In the first one, the refractive index change is created just at the focal volume of the incident beam. This approach was the first in being investigated and, in general, it requires the use of low pulse energies (a few nJ), therefore it can be carried out with only the use of a femtosecond oscillator [6]. This is the most common technique for the fabrication of waveguides in glasses. The waveguides fabricated by this technique have been used for the implementation of complex devices such as coupled waveguide arrays where the structures are in close proximity allowing the interaction between modes of adjacent waveguides [25, 26] or Bragg gratings [27]. The second one involves the use of amplified laser pulses with energy typically in order of mJ. In this case a severe damage track along the focal volume is produced inducing a refractive index decrease over the damage. Furthermore, a local increase of the refractive index is induced in the surrounding area of the damage. This increase can be easily manipulated by making a second irradiation at some microns of the first one. As a result, the refractive index change

can be easily increased or shaped. This technique is used for the fabrication of waveguides in crystals. This approach is specially used for the fabrication of active devices [25] with attractive characteristics such as preservation of the spectral and anisotropy properties [28, 29] as well as the resistant to high temperatures [30]. This type of modification can be also used to fabricate the so-called depressed cladding waveguides. For this kind of waveguide, a large number of irradiations parallel to each other are carried out, delimiting an area of the material that is not irradiated where the irradiated area acts as a boundary for the light [31]. Further details about the type of waveguide fabricated by ULI process will be discussed in Chapter 2. Fig. 1.2 shows waveguides fabricated with different femtosecond laser induced modifications. The mechanisms responsible for the ultrafast laser inscription, as well as its optical properties, depends on the material properties and on the irradiation conditions, such as pulse energy, pulse duration, repetition rate, polarization, focusing conditions and translation speed. All these parameters can be optimized in order to fabricate the desired kind of waveguide with certain properties, that is to say, mono/multi-mode, refractive index profile, or optical losses [32].
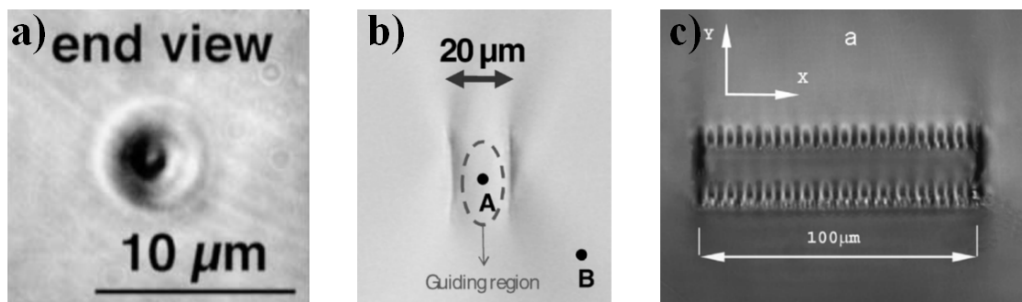
Fig. 1.2 Optical micrograph of the cross section of waveguides fabricated using different femtosecond laser induced modifications. a) Waveguide fabricated in glass with the use of a femtosecond oscillator (unamplified pulses) [33]. b) Waveguide fabricated in a transparent ceramic by two parallel damaged tracks using amplified femtosecond pulses [34]. c) Depressed cladding waveguide fabricated in a Nd:YAG crystal by several parallel damaged tracks [31]

Nowadays ultrafast laser inscription (ULI) has been established as one of the most fast and efficient techniques for the fabrication of 3D embedded structures in transparent optical materials [35–41] unable to carry out with any other conventional technique such as ion implantation, chemical vapor deposition, ion proton exchange or sputtering among others, which are based on photolitographic process [23]. In this sense, ULI process presents many advantages compared with standard techniques, for example, it is a single-step process that does not needs either a mask or a post-development processing. Although, the fact that most of the photonic structures fabricated by ULI do not present yet the high quality standards obtained by the traditional methods, it must be stressed that ULI offers important and attractive characteristics,

being one of the most interesting the possibility to directly fabricate or inscribe any 3D arbitrary microstructure at any deep of the sample. In addition, it is also possible to inscribe structures with different functionalities integrated as a monolithic structure. Additionally, in the last years, ULI has also been employed as an important tool for the fabrication of optofluidic components designed in compact architectures for lab-on-a-chip applications [42]. The advantages of 3D inscription capability make of ULI an important fabrication technique with impact in a wide variety of applications in different areas ranging from astrophotonics, optical communication, biophotonics, quantum optics and informatio processing [43–45]. ULI has been probed to be an excellent waveguide fabrication method for a wide range of materials, including amorphous glasses, single crystals, polycrystalline ceramics, and organic polymers.

Numerous passive devices fabricated by ULI have been reported, benefiting from the 3D fabrication capability. Some of these devices are for example, power splitters [46, 47], couplers [6, 48] , Mach-Zehnder interferometers [7, 49] or Bragg gratings [50]. In the field of active devices, Sikorski et al. [5] reported the first optical amplifier based on a waveguide inscribed by a femtosecond laser (on a silicate glass doped with Nd). On the other hand, Osellame et al. [51] demonstrated for the first time, the fabrication of active waveguides that presented internal gain in a glass doped with ions of Er and Yb. Furthermore, they presented the first waveguide laser (at 1533.5 nm) [9] and an amplifier over the entire optical communications C-band (1530-1565) [52]. Furthermore, a variety of exciting works have been developed in transparent dielectrics implementing multiple geometries and configurations that offers a wide range of possibilities for versatile applications in diverse areas of interest. Some of this interesting works are continuous wave or pulsed waveguide lasers [53–55], amplifiers [56, 57], microfluidics chips [58, 59] and quantum photonic devices [60].

In summary, 3D photonic structures in transparent materials fabricated by ULI are an essential part of a great variety of photonic devices, which are important for applications in different fields. The possibility of confining light and fabricate active photonic devices (such as waveguide lasers or frequency converters) integrated into these kind of materials, allows the design of compact experiments, until recently unsuspected. On the other hand, it should be noted that although the fundamentals of ULI are well understood and have been extensively studied in literature, much work remains to be done in terms of the optimization of the waveguide fabrication techniques as well as the technological development for the fabrication of complex devices. The work presented here has tried to contribute new knowledge in both aspects.

1.3   Methodology

Overall, the fabrication of the waveguides was firstly done by testing the effect of laser irradiation at different pulse energies, sample depths and focusing conditions (numerical aperture). Once these tests were performed and analyzed with different microscopy techniques, the waveguides were produced with the most appropriate parameters for the type of fabrication technique to be used. After the waveguides had been fabricated, their guiding properties were analyzed by coupling a low power laser, with which images of the confined modes were taken. For the ultrashort pulse coupling into the waveguides, it was necessary to change the focusing optics and setup a specific system. Regarding to the studies on each specific material, the variation of the laser parameters such as pulse energy, beam size and speed scan allowed to induce changes in the optical properties of the material such as refractive index. Once the irradiation parameters were identified, waveguides structures were fabricated in different transparent dielectrics such as crystals and ceramics.

1.4   Objectives

The main objectives of this thesis work are the following:

- *To get advance in the techniques for the microfabrication of waveguides in optical materials which are currently the "state of the art" in this field.*

- *To propose and demonstrate new schemes of fabrication and integration of photonic elements in optical materials, such as crystals and ceramics.* New geometries and structuring techniques are proposed to improve certain properties of the waveguides, such as maximum supported power, propagation losses or modal profile quality.

- *To design and analyze the possibility to fabricate waveguides for applications in the field of ultrashort laser pulses.* Waveguides integrated in optical materials have been mainly used in the continuous regimen, yet there are just a few studies on the possibilities that they offer in the control of femtosecond pulses. In this work a preliminary study of the temporal features of ultrashort pulses propagating to different types of waveguides is done.

- *To study the ultrafast laser-induced modifications of femtoseconds pulses in the nanostructured polycrystalline YSZ ceramic as well as the study and the integration of optical waveguides in this material* This ceramic has a great variety of applications in demanding environments and only recently has been considered for optical applications. In

this work, in addition to the ultrafast laser inscription of waveguides in this material a characterization of the optical and nonlinear optical properties is presented.

1.5   Organization of the thesis

This thesis is composed of seven chapters,

In *Chapter 2* the basic concepts of ultrafast laser microprocessing of materials are discussed. The basic experimental arrangement used for such processing is described in addition to the basic differences between the microprocessing with long-duration pulses (ns) and ultra-short pulses (ps-fs) as well as the physical mechanisms involved in the interaction. Furthermore, the different approaches for the fabrication of photonic devices using ultrashort lasers are also presented.

In *Chapter 3* the experimental techniques used during the development of this thesis are introduced. These include the experimental setup for the fabrication of the waveguides, as well as the setups and techniques necessary for the characterization of the fabricated waveguides.

Chapter 4 presents a study of the response of the polycrystalline nanostructured YSZ ceramic to ultrashort laser pulses irradiation. A study of the micromachining properties as well as an analysis of its nonlinear optical properties is presented. In addition, the fabrication of waveguides inside this material with the aim to determine its characteristics to be used as an optical material is also introduced.

Overall, *Chapter 5* presents the results and analysis concerned with new approaches for the fabrication and implementation of photonic devices directly written en transparent dielectrics by femtosecond laser irradiation. In particular, the simultaneous two-beam femtosecond laser technique, depressed cladding waveguides arrays and waveguides with photonic lattice-like structures are presented.

Chapter 6 analyzes the effect of ultrashort laser pulses over the fabricated structures. In this chapter, a system to characterize the propagation of ultrashort laser pulses (spectrally and temporally)through ultrafast laser inscribed waveguides by analyzing the dispersion properties is proposed.

Finally, *Chapter 7* reports the general conclusions about this thesis work.

Chapter 2

Ultrafast laser microprocessing of materials

Ultrafast laser microprocessing of materials consists of using femtosecond pulsed lasers to micro-structure the surface of absorbing materials or the bulk (inside) of transparent materials. Depending on the duration of the pulses, there are important differences in the interaction of the pulses with the material and therefore in the processing results. Throughout this chapter the basic concepts of ultrafast laser processing of materials will be discussed. The basic arrangement used for such processing will be described, in addition to the basic differences between the microprocessing with long duration pulses (ns) and ultra-short pulses (ps-fs) as well as the physical mechanisms involved in the interaction.

2.1 Basic components of an ultrafast laser microprocessing stage

Generally, the microprocessing of materials may be carried out using nanosecond (10^{-9}s), picosecond (10^{-12}s) or femtosecond (10^{-15}s) pulsed lasers. As far as this thesis work is concerned, the processing was carried out on transparent dielectric crystals using amplified femtosecond pulses. Typically, a Ti:sapphire laser oscillator emits pulses centered around 800 nanometers at repetition rates in the order of megahertz with a duration in the range of 50 to 100 femtoseconds and per pulse energies of a few nJ. Laser oscillators with larger per pulse energy exist , but to achieve energies of the order of μJ and even mJ, it is necessary to amplify the output of the oscillator. The amplification reduces the repetition rate of the laser to the kilohertz range due to the impossibility to pump the laser crystal at such high frequency at the power level required for the amplification, as a result, the interaction with the material changes,

particularly with regard to the induced modifications during the interaction. Due to the short duration of ultrashort pulses there is not time for heat coupling during the irradiation, confining the modifications to the focal volume inside the material, in which permanent or very stable refractive index changes can be created [61].

Ultrafast laser microprocessing of materials can be carried out either by using an amplified laser pulses system or directly using the output of an oscillator. When the microprocessing is performed using only an oscillator, with only a few nJ per pulse, it is necessary to use large numerical aperture (N.A.) lenses to achieve the high intensities necessary to induce structural changes in the sample. However, there are some advantages derived from the high repetition rate of the oscillator, where the thermal effects may favor the processing [33]. On the other hand, a system of amplified pulses does not require a tightly focusing to reach high intensities, since it possesses per pulse energies larger than those of an oscillator. Therefore, it is possible to make use of lenses or microscope objectives with a smaller numerical aperture [62].

A basic arrangement for laser microprocessing of materials consists of a lens or microscope objective and a three-axis micrometer translation station in which the sample is placed. Thus, the station is moved with respect to the beam focus, creating continuous structures on the surface or in the bulk of the sample. Fig. 2.1 shows a typical experimental arrangement of a laser microprocessing stage.

Although there are a large number of aspects that differ in the interaction of the laser with the material, arrangements for the microprocessing of transparent materials and absorbent materials are essentially the same. Laser parameters and properties of the material determine the interaction and hence the results of the microprocessing. The per pulse energy, repetition rate, wavelength and pulse duration are properties that play a key role in the optical interaction of the pulses laser with the material. On the other hand, specific properties of the material such as the bandgap and thermal properties determine whether laser microprocessing is possible and how the resulting structures look and behave. In the next section the physical mechanism by which the material absorbs energy from the laser will be discussed.

2.2   The physics of ultrafast laser processing

The interaction of ultrashort laser pulses with materials differs from interaction with long pulses or continuous wave light in two ways. Firstly, energy deposition occurs on a time scale that is shorter compared to any other relaxation process. The energy of the laser is absorbed by the electrons, and the thermalization takes place only after the laser pulse. Secondly, the intensity of a ultrashort pulse, even at moderate energy, is high enough to induce large nonlinear absorption
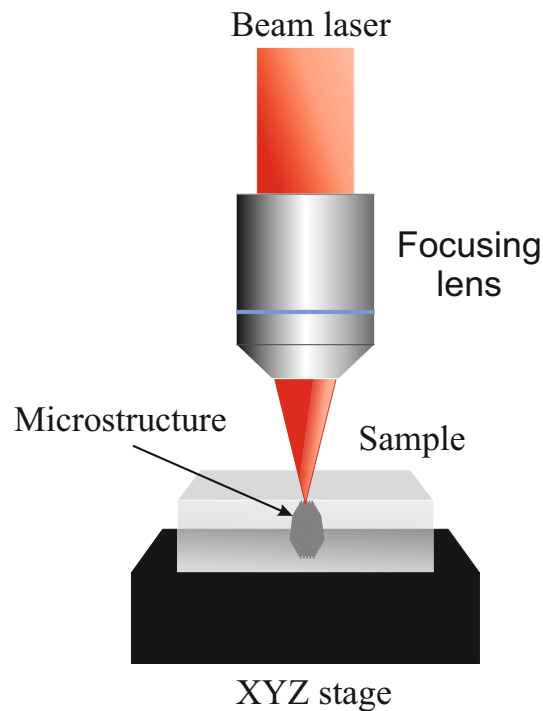
Fig. 2.1 Basic experimental setup for the ultrafast laser microprocessing of materials. The laser beam is focused by a microscope objective or lens onto the surface of an absorbent material or in the bulk of a transparent material. The sample is placed on a xyz stage and is moved with respect to the focus to obtain the desired structure.

processes in materials that do not normally absorb the wavelength of the laser (transparent materials).

2.2.1　Linear absorption

The linear absorption of ultrashort pulses is not entirely different from the linear absorption of any other optical field. In dielectric materials, for example, the highest energy level occupied by an electron (in the valence band) is separated by an energy gap (the bandgap) of the lowest empty energy level in the conduction band. If the photon energy exceeds the energy of the bandgap, light can be absorbed by the material, causing electrons in the valence band to cross the conduction band (left side Fig. 2.2). In metals, for example, the conduction band is partially occupied, leaving energy levels slightly higher than those occupied. In this case, photons can be absorbed through free charges absorption, a process by which an electron gains energy by absorbing it from a photon, and gains momentum, through an interaction with a phonon

(wave generated by a vibration of the material lattice) to move to a higher energy level in the conduction band [63].

Linear absorption   **Nonlinear absorption**

Multiphoton   **Avalanche**

Conduction Band

Band Gap

Photon   **Free electron**

Energy   Hole

Valence Band

Time
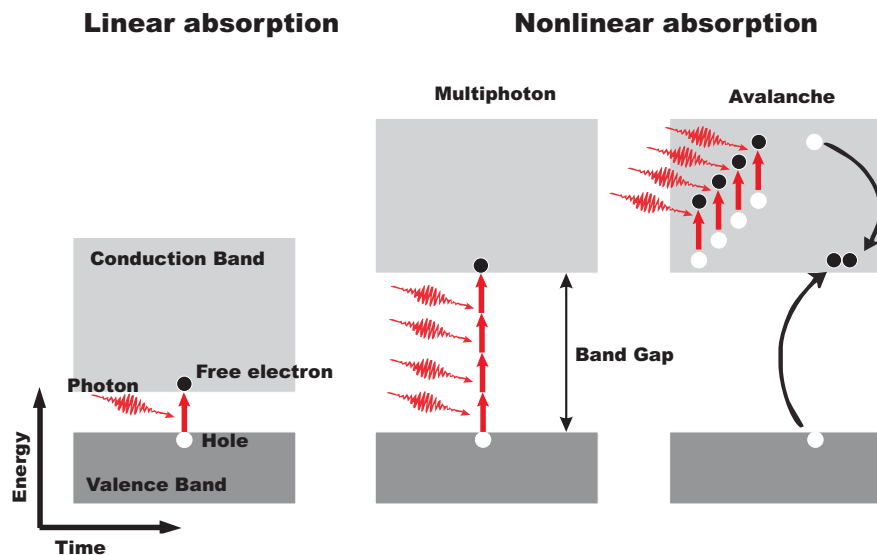
Fig. 2.2 Schematic diagram of the physical mechanisms that take place during ultrafast laser microprocessing [62].

2.2.2   Nonlinear absorption

In materials that are transparent to the wavelength of the laser, a single photon of light does not possess the energy required to excite an electron from the valence band to the conduction band and the absorption of the laser energy can occur through nonlinear processes. If enough energy is deposited in the material through nonlinear absorption, ablation (removal of material) in the case of the surface or permanent structural changes inside the material may occur. Because absorption is nonlinear, and therefore, the probability of absorption is a nonlinear function of the intensity of the laser, the absorption can be confined to the bulk of a transparent material by just focusing the laser beam within the sample, producing a larger intensity in the focal volume around the waist of the beam, than in the surface.

There are two mechanisms of nonlinear excitation that play an important role in this nonlinear absorption, photoionization and ionization by avalanche. In photoionization, the electrons are excited directly from the valence band to the conduction band by the intense field of the laser. Depending on the frequency and intensity of the laser, there are two different regimes of photoionization, multiphoton ionization and tunnel ionization [64].

In tunneling ionization, the electron can be ionized because the electric field of the laser disturbs the atomic potential creating a potential barrier that the electron can cross through tunneling effect. Strictly speaking, the high electric field of the laser pulse lowers the Coulomb potential energy barrier allowing the electron to cross from the valence to the conduction band [**?**].

Multiphoton ionization involves the simultaneous absorption of multiple photons by one electron (central part of Fig. 2.2). In this case, the total energy of the absorbed photons must exceed the energy of the bandgap, that is, $n\hbar\omega \geq E_g$ where E_g is the energy of the bandgap, ω is the laser frequency, $\hbar$ the Planck constant, and n is the minimum number of photons required for ionization. On the other hand, Multifotton absorption requires n photons to simultaneously interact with an electron, therefore, the probability of absorption will be given by the density of photons n. Because the photon density is proportional to the laser intensity I, the probability for multiphoton absorption is given by I^n [65].

In avalanche ionization, a free electron, at the bottom of the conduction band and exposed to an intense optical field, is accelerated acquiring kinetic energy. When its total energy exceeds the minimum conduction band, it may ionize another electron from the valence band, which results in two electrons in the minimum conduction band (right part of Fig. 2.2). These electrons can, in turn, be accelerated by the electric field of the laser, whereby the process is repeated. This causes an avalanche, where the density of free electrons grows exponentially [**?**].

It should be mentioned that avalanche ionization requires some "seed" electrons in the conduction band of the material. For ultrashort laser pulses, photoionization during the initial portion of the pulse provides these seed electrons for avalanche ionization during the rest of the pulse [66]. Electron density grows through avalanche ionization until the electron plasma frequency is close to that of the laser (critical plasma density). This high plasma density strongly absorbs energy by absorption of free charges. For ultra short pulses, the absorption described above occurs on a time scale that is shorter compared to the time scale for transferring the energy to the lattice, decoupling thermal processes from the lattice [62].

2.3   Energy relaxation

As discussed above, the first interaction of the laser radiation occurs with the electronic states of the valence and conduction bands. The time to deposit energy on these states is determined by the duration of the pulse. Then, the deposited energy is redistributed over several states of energy of the system, therefore, it is transferred from the electrons to the lattice. To understand the difference of the interaction of ultrashort pulses and long pulses with matter, it is convenient

to consider the characteristic time scales. Considering that the electronic relaxation time of the ionized solid takes a few picoseconds (and even nanoseconds), two distinct regimes of interaction can be distinguished [67].
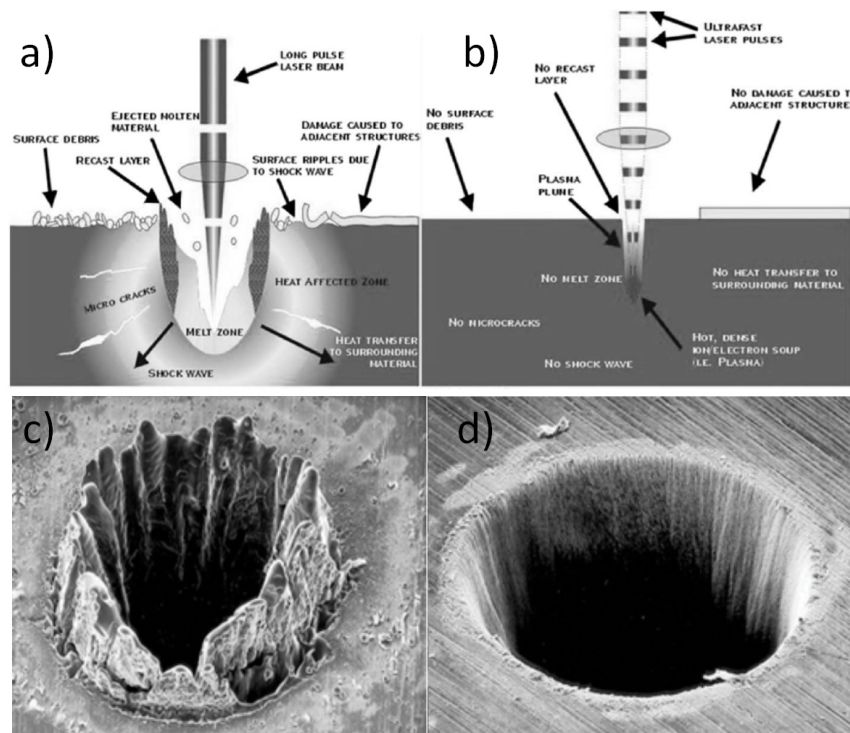
Fig. 2.3 Effect of laser ablation using (a) ns pulses and (b) fs pulses[68]. Comparative example of the use of ns laser pulses (c) versus fs laser pulses (d) when drilling micro holes in stainless steel [69, 70].

Nanoseconds regime

Here the pulse duration is larger than the electronic relaxation time of the material. In this case, there is a possibility of energy coupling in the form of heat in the vicinity of the focal volume. As a result, the material melts and a part of this is evaporate generating an ablation cloud that is expelled from the interaction zone. This type of radiation generates significant collateral damages in the material (transformations in the vicinity of the irradiated zone) of thermal and mechanical type.

Picoseconds and Femtoseconds regime

In this regime the pulse duration is shorter than the electronic relaxation time. In this case, the laser pulse is extinguished before the optical energy transformed into heat propagates

beyond the volume of interaction. In this way energy is confined to the volume of interaction minimizing collateral damages. Due to this reason ultrafast laser microprocessing allows to achieve high precision processing by forming microstructures of high quality. Fig. 2.3 shows a comparison of the microprocessing using long duration pulses versus ultrashort laser pulses.

2.4 Processing regimes

Depending on the processing conditions, the thermal relaxation of the material may be given in certain conditions. At the moment in which laser-matter interaction begins, the energy accumulated in the focal volume diffuses thermally. During this process the material may be in a melting state, depending on the processing conditions. Finally the material re-solidifies, therefore, some of its properties change locally. The time scale in which thermal diffusion occurs, and more precisely the time required for the material to cool completely at room temperature, is an important characteristic in the ultrafast laser microprocessing of materials since it defines the shape and size of the resulting structure.

The regime of processing is classified depending on the laser system used in the processing in *low repetition rate* and *high repetition rate* [71]. As far as this thesis is concerned, the fabrication of waveguides was carried out in the low repetition rate regime. In the first case, the processing is carried out with a amplified laser system. In this case, the repetition rate is typically in the order of the KHz and therefore, the emitted pulses by the system are separated by milliseconds, which in most of the cases depending of the material properties, exceeds the time required for heat to diffuse out of the focal volume. Hence, the material in the focal volume returns to room temperature before the next pulse arrives. Consequently, thermal effects by heat accumulation do not play an important role in the processing. This regime is also known as nonthermal regime. In the second case (thermal regime), the heating produced by one pulse that strikes the sample overlaps with the heating produced by the subsequent pulse, generating a cumulative effect in the focal volume. Here, the repetition rate of the emitted pulses by the laser oscillator is of the order of MHz, hence, the pulses are separated by a time interval of a few nanoseconds which is significantly shorter than the time for heat to diffuse out of the focal volume ($\approx 1\mu$s) in most of transparent dielectric materials. As a consequence, there is no time enough to dissipate the energy deposited between each pulse outside the focal volume, which cause a heat accumulation in the neighborhood causing changes around the focus. In this case, the pulses of the oscillator constitute a heat source in the focal volume [72, 73]. Fig. 2.4 shows the differences between the laser processing using amplified and unamplified laser systems. The transition between both regime can be easily calculated by the critical frequency equation given by [74]:

$$f_{crit} = \frac{\alpha}{d^2}, \tag{2.1}$$

where α is the thermal diffusivity of the material and d is the diameter of focal spot. As an example, laser annealing effect [75] has been demonstrated for waveguides fabricated at high repetition regime as well as an improvement of the performance by reducing the propagation losses [76].
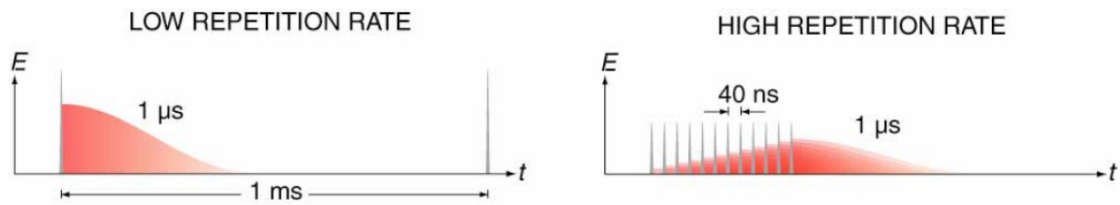
Fig. 2.4 Differences between the laser processing of using low repetition an high repetition rates laser systems. In the first case, the energy deposited in the focal volume diffuses before the next pulse arrives. In the second one, energy is accumulated due to the short duration between the pulses [71].

2.5 Geometries used for ultrafast laser inscribed waveguides

Another important parameter that must be considered in the fabrication of waveguides by ULI is the inscription geometry (see Fig. 2.6). For instance, there are two main configurations, *longitudinal inscription* and *transverse inscription*. In the first case, the sample is translated parallel to the beam propagation axis. In this case, the diffraction limit and the working distance of the focusing optics determines the size of the structure [77]. On the other hand, in the transverse inscription geometry the sample is moved perpendicular to the beam propagation. The size of the structure is not limited by the working distance of the focusing lens which allows the fabrication of more complex structures. This kind of geometry is the most used for the fabrication of photonic devices.

2.6 Scanning speed

In the fabrication of waveguide by ULI another important parameter that must be taken into account is the scanning speed. The number of pulses that impinge on each point of the sample is determined by the velocity at which the sample is translated with respect to the focus.

LONGITUDINAL   TRANSVERSE
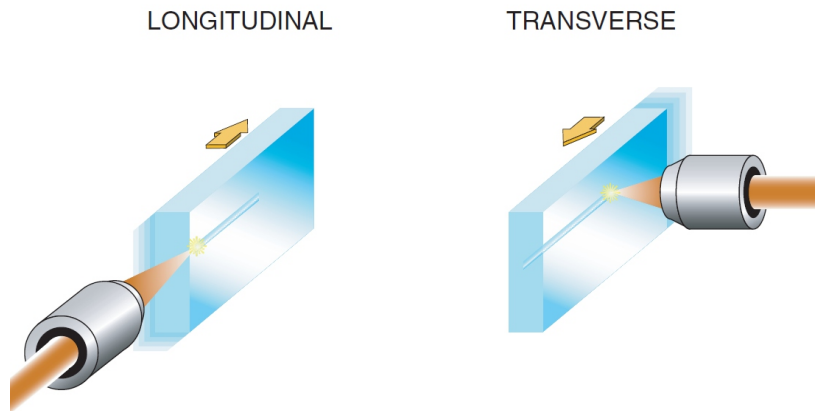
Fig. 2.5 Geometries used for ultrafast laser inscription of waveguides in transparent materials [78].

Some characteristics of the waveguide structure such as the diameter is directly related to this parameter. The slower the scanning speed, the more pulses strike the same spot. As a consequence, the radius to which the material is heated above the focal volume increases and that determines the diameter of the final structure [78]. The number of pulses that strikes the sample can be easily estimated by

$$N = \frac{d \cdot f}{v},$$ (2.2)

where d is the diameter of the focal spot, f is the repetition rate and v is the scanning speed. As an example Fig. **??** shows the effect of the scanning velocity in a Nd:YAG ceramic.

E=0.42 μJ
v= 10 μm/s   50 μm/s   100 μm/s   500 μm/s
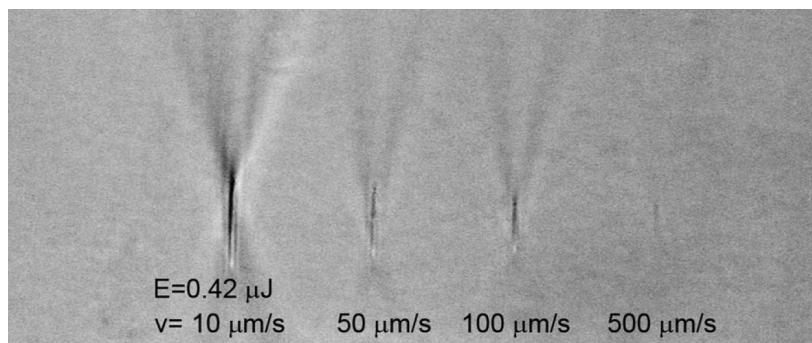
Fig. 2.6 Optical micrograph of a series of tracks produced in a Nd:YAG crystal by 120-fs pulses showing the effect of the scanning velocity. The tracks was produced by focusing the laser beam 150 μm beneath the sample surface [61].

2.7   Types of ultrafast laser inscribed waveguides

As mentioned before, ultrafast laser microprocessing consists of the modification or ablation of a material when an intense short pulse is focused in the surface or bulk of a material. In the case of transparent dielectrics (such as a large number of glasses and crystals), besides to being able to interact with the surface of the material, it is possible to do so at any depth of the sample. To do this, the pulsed beam is focused inside the sample: if the intensity reached in the focal zone is large enough, the same processes of nonlinear absorption and strong field ionization that take place on the surface of a material during laser ablation are induced, generating a plasma of free electrons but in this case inside the material. The effect or footprint that leaves that plasma once relaxes is varied and depends on both the irradiation conditions and the type of material. In general, we can speak of a modification of the refractive index, either in the area directly irradiated by the laser, or in the surrounding area, always on the scale of a few microns.

In the particular case of waveguides in transparent materials, which is the kind of photonic device on which this work is focused, there is a well accepted classification. The classification depends on the induced refractive index changes in the irradiated zones. These modifications are classified as *Type I* and *Type II*. In the first case, the modifications can lead to both increment and decrement of the refractive index. These kind of modification are soft and sometimes reversible under high temperatures. The type II modifications are associated with a decrement of the refractive index in the irradiated zone which are generally in the form of damaged tracks an by an increase around the tracks. These are structural modifications that are not reversible [59].

In turn, waveguides fabricated by ultrafast laser inscription are classified according to the type of modification and the geometry used to achieve light confinement by using either positive or negative refractive index changes [61, 79]. Fig. 2.7 shows different types of ultrafast laser inscribed waveguides.

2.7.1   Directly written waveguides

It is talked about directly written waveguides for photonic structures based on Type I modification. In some materials and with certain irradiation conditions (typically low per pulse energies and low scan speeds), a positive refractive index change (Δn) just in the focal volume of the beam is induced [2]. Therefore, if a path with the focused beam within the sample is describes, a channel with a larger refractive index than the unprocessed material, by which light can be confined can be created. This positive change ($\Delta n > 0$) allows the direct fabrication of 3D photonic structures with feasible geometries. This approach is the most common technique for the fabrication of waveguides in optical glasses, but is infrequent in crystalline materials. These

kind of modification have been widely used for the fabrication of passive pohtonic devices such as Y-junctions, directional couplers or gratings [59, 60, 80–82]. Several mechanisms have been proposed to explained the change in the refractive index in this kind of waveguides [83]. A first possible mechanism is the formation of color centers [84]. The femtosecond pulse irradiation produces a number of color centers in the material that absorb in the UV, modifying the refractive index of the material over the wavelengths of interest through the Kramers-Kroening mechanism. An alternative mechanism is a thermal mechanism. The energy deposited by the laser melts the material in the focal volume and the subsequent dynamics of rapid resolidification and cooling of the material generates density variations, which causes changes in the refractive index [33, 85]. A third mechanism is a photoestructural change directly induced by the femtosecond pulses, which results in a rearrangement of the chemical bonds of the lattice in the material, inducing an increase in density [86]. All these mechanisms play an important role in the refractive index change and it is difficult to know their contributions separately.

2.7.2 Stressed induced waveguides

In waveguides based in Type II modifications or commonly called stress induced waveguides the material is irradiated with higher per pulse energies (micro-Joules) so that there is a severe damage in the focal volume causing a negative refractive index change ($\Delta n < 0$). As a collateral effect to the plasma created during the irradiation, a mechanical wave that compresses the material around the focus is formed, creating an increase of the refractive index. To further increase the refractive index and favor the confinement of light, two parallel irradiation separated by a few microns are usually made with the laser, between which the waveguide is formed [28, 87]. This is the most usual laser inscription technique in crystals. Waveguides based in Type II modifications have important characteristics, for example, the core is located in regions between the damaged tracks, therefore the material of the core is not significantly affected, as a consequence, the luminescence and nonlinear properties of the material in that zone are well preserved. These characteristics make of this waveguides the most used for the fabrication of active devices such as waveguide lasers [88–95] and frequency converters in both CW and pulsed laser regimes [96–100]. It should be to pointed it out that in this case the mechanisms responsible for the change in the refractive index are well understood [88] in comparison with waveguides based in Type I modifications.

2.7.3   Depressed cladding waveguides

Depressed cladding waveguides are fabricated with type II modifications but light confinement does not rely in mechanical stress. For this type of waveguide, a large number of irradiation parallel to each other (with $\Delta n < 0$), are performed with the laser, delimiting an area of the material that is not modified, where the irradiated area acts as a boundary for light [31]. The damage tracks are close to each other (generally 3-4 μm) and the core is away from the tracks. This kind of waveguides has atracted a lot of interest in the last years mainly due to fact that can be made with any geometry and dimensions, light is confined for any polarization in many cases, and as well as the stressed waveguides they do not disappear at high temperature, thus, can be used for high power applications. In addition, depressed cladding waveguides have been proved to be a very efficient structures for mid-IR waveguide laser applications mainly due to the ease of manipulate the cross section of the waveguide. Furthermore, in this case the core remains unirradiated which is atractive for active devices. A variety of photonic devices with atractive characteristics have benn demonstrated in transparent dielectrics such waveguide lasers and frecuency converters [101–104] as well as photonic structures in the near-IR and mid-IR ranges [105–107].
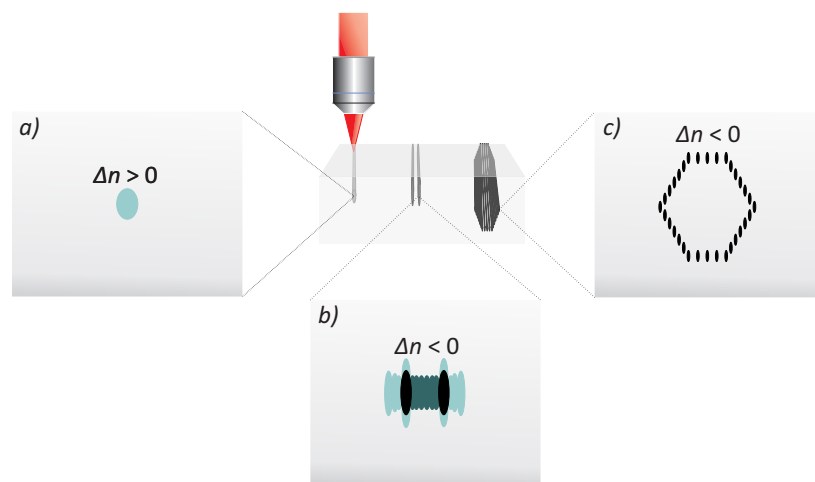
Fig. 2.7 Cross section of different types of waveguides written according to the induced refractive index change (Δn). Blue color represent an increment of the refractive index of the material while black color represents a decrement. a) Type I: the waveguide is directly written and the light is confined over the irradiated zone. b) Type II, the core of the waveguide is in between two damaged tracks of $\Delta n < 0$. Type III or depressed cladding waveguide. The light is confined in a unmodified region and ligth is trapped by several damaged tracks of $\Delta n < 0$.

2.8 Theoretical background

In the context of material processing using pulsed lasers, fluence and irradiance are very important parameters to be determined. For its definition, we start from the expression for the electric field of a Gaussian laser pulse, assuming also a Gaussian beam profile given by [108]:

$$E(r,t) = E_0 e^{i\omega t} e^{-\frac{r^2}{\omega_0^2}} e^{-\frac{t^2}{\tau^2}}, \tag{2.3}$$

where E_0 is the amplitude of the electric field, ω_0 is the beam radius at $1/e^2$, τ is the pulse duration (FWHM), ω is the oscillation frequency of the electric field, r is the radial coordinate and t is the temporal variable. The *intensity* or *irradiance* can be defined as the amount of optical energy per unit time per unit area, measured in a time t in some point of the space. This can be re-written as

$$I(r,t) = \frac{1}{2}\sqrt{\frac{\varepsilon}{\mu}} E(r,t) E^*(r,t), \tag{2.4}$$

where ε and μ are the electrical permittivity and the magnetic permeability of the medium respectively and E^* is the complex conjugate of the electric field. Substituting Eq. (2.3) into Eq. (2.4) the intensity associated to a Gaussian pulse is given by

$$I(r,t) = \frac{(E_0)^2}{2}\sqrt{\frac{\varepsilon}{\mu}} e^{-\frac{2r^2}{\omega_0^2}} e^{-\frac{2t^2}{\tau^2}} = I_0 e^{-\frac{2r^2}{\omega_0^2}} e^{-\frac{2t^2}{\tau^2}}, \tag{2.5}$$

where

$$I_0 = \frac{(E_0)^2}{2}\sqrt{\frac{\varepsilon}{\mu}} \tag{2.6}$$

The intensity is the relevant magnitude for the nonlinear processes to take place. However, there is another magnitude that is frequently used in materials microprocessing that is the laser fluence (J/cm^2). The mean fluence is defined as the pulse energy divided by the cross section of the beam. As the beam shape is not flat, it is very convenient to define a local fluence that is the fluence at each point of a transverse plane to the propagation direction. It can be obtained from (2.3) by integrating in time the intensity from $t = -\infty$ to $t = +\infty$, that is, integrating the total pulse duration. In this way it is obtained that the *local fluence* for a Gaussian pulse is given by

$$F_p(r) = (E_0)^2 \frac{\tau}{2}\sqrt{\frac{\pi}{2}\frac{\varepsilon}{\mu}} e^{-\frac{2r^2}{\omega_0^2}} = I_0\sqrt{\frac{\pi}{2}}\tau e^{-\frac{2r^2}{\omega_0^2}} \tag{2.7}$$

If instead of calculate the integral with respect to time, it is carried out with respect to space, the *instant power per pulse* can be obtained which is given by

$$P_t = \int_0^\infty I(r,t) 2\pi r dr = (E_0)^2 \frac{\pi \omega_0^2}{4} \sqrt{\frac{\varepsilon}{\mu}} e^{-\frac{2t^2}{\tau^2}} = I_0 \frac{\pi \omega_0^2}{2} e^{-\frac{2t^2}{\tau^2}}. \tag{2.8}$$

On the other hand, if a double integral in time and space is carried out, the *per pulse energy* is obtained

$$E_{tot} = \int_{-\infty}^\infty \int_0^\infty I(r,t) 2\pi dr dt = (E_0)^2 \frac{\pi \omega_0^2 \tau}{4} \sqrt{\frac{\pi}{2} \frac{\varepsilon}{\mu}} = I_0 \left(\frac{\pi}{2}\right)^{\frac{3}{2}} \omega_0^2 \tau. \tag{2.9}$$

It is convenient to express the fluence of a pulse (F_p) in terms of the total energy (E_t) and not in terms of the electric field (E_0); this because the total per pulse energy is easy to measure experimentally, which is not the case with the amplitude of the electric field. From Eq. 2.9 it can be obtained that

$$\frac{2E_{tot}}{\pi \omega_0^2} = (E_0)^2 \frac{\tau}{2} \sqrt{\frac{\pi}{2} \frac{\varepsilon}{\mu}}, \tag{2.10}$$

and

$$\frac{2E_{tot}}{\pi \omega_0^2} = I_0 \sqrt{\frac{\pi}{2}} \tau \tag{2.11}$$

Finally, replacing into Eq. 2.7, the *per pulse fluence* is obtained which is expressed as

$$F_p(r) = \left(\frac{2E_{tot}}{\pi \omega_0^2}\right) e^{-\frac{2r^2}{\omega_0^2}}. \tag{2.12}$$

It should be remarked that this definition is valid only for Gaussian pulse profiles and Gaussian beams.

2.8.1 Focusing a femtosecond pulse with Gaussian beam profile

The intensity at the waist of the beam produced by a laser pulse is determined the focusing conditions. For Gaussian beams, the radius of the beam waist, ω_f, for which the intensity is reduced by a factor of e^2 with respect to the intensity at the center of the beam profile is given by [108]

$$\omega_f = \frac{2\lambda f}{\pi \omega_0}, \tag{2.13}$$
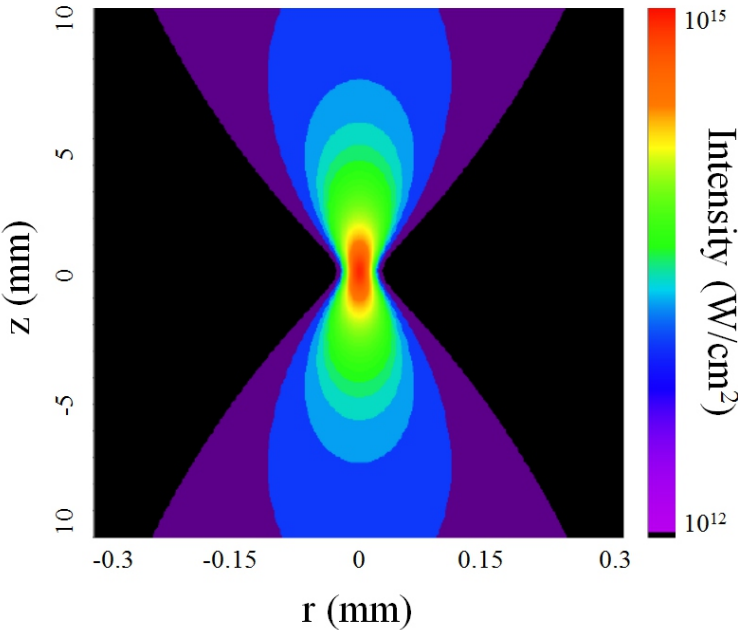
Fig. 2.8 Contour plot for a femtosecond laser beam with a $\lambda = 800$ nm, a per pulse energy of 1 mJ, pulse duration of 50 fs, focused by a 250 mm focal length with a beam size at the lens of 10 mm. The maximum peak intensity is reached at the minimum size of the beam.

where ω_0 is the radius of the incident beam on the lens, λ is the wavelength of the laser and f is the focal distance of the lens. The length around the focus at which the minimum radius of the beam remains constant is indicated by the Rayleigh length, z_0. This is defined as the distance along the beam propagation axis for which the intensity of the beam decreases by a factor of $\sqrt{2}$, and has the form

$$z_0 = \frac{\pi \omega_f^2}{\lambda}, \tag{2.14}$$

If it is assumed that the intensity of the laser $I(I_0, r, z, t)$ of a focused pulsed beam can be expressed as a Gaussian spatial profile with a Gaussian temporal envelope, then we can write it as [109]

$$I(I_0, r, z, t) = \frac{I_0}{1 + (z/z_0)} \exp\left(\frac{2r^2}{\omega_f^2[1 + (z/z_0)^2]}\right) \cdot e^{\frac{-2t^2}{\tau^2}}, \tag{2.15}$$

where τ is the temporal width of the FWHM pulse. As an example Fig.2.8 shows a contour plot intensity for a femtosecond laser pulse. As it can be seen in the contour plot, the smaller the volume generated by the lens when focusing the beam the larger peak intensity is achieved. This characteristic makes possible that femtosecond pulse could be focused inside a transparent material leaving the surface intact due to the fact that nonlinear effects are only induced in the focal volume.

It should be stressed that this is valid for free propagation but is not valid when focusing inside a material, which is the case of interest in thefabrication of waveguides, since the beam is distorted by passing through the air-material interface and the pulse experiences linear dispersion as it propagates within the material. In addition there are nonlinear (second and third order) propagation effects, as well as ionization, which make the beam propagation very complex, thus, it is necessary to use very elaborated numeric models.

Chapter 3

Experimental techniques

In general, the experiments consisted in the laser irradiation of different transparent dielectrics for the fabrication of optical waveguide structures. In this chapter, the experimental techniques used for the microprocessing and characterization of the structures presented in this work will be reviewed and analyzed. The theory and details of the different experiments to characterize such structures are also introduced.

3.1   Laser microprocessing stage

For the development of this work, the equipment from the *Laboratorio de Láseres Pulsados* of the Universidad de Salamanca was used. The main system of this laboratory is a Ti:sapphire laser with CPA (*Chirp Pulse Amplification*) technology. The laser consists of two outputs: the first one is obtained after a regenerative amplifier that emits pulses of 120 fs at a central wavelength of 795 nm, per pulse energy of 1 mJ and repetition rate of 1 KHz. The second one, can reach a maximum per pulse energy of 50 mJ with a repetition rate of 10 Hz. These systems are used for a variety of experiments in the laboratory. With regard to this work, the laser irradiation was carried out using the first output which corresponds to the *Laboratorio de Microprocesado de Materiales con Láser*. This laboratory is equipped with a high precision processing stage composed by elements as power control system, electronic shutter, 4-axis micro-positioners, focusing lenses and beam control optics. The central wavelength can be modified with a second (400 nm) and third (266 nm) harmonic generation setup. The micro-positioners are controlled by computer through an home-made automation software and allows the simultaneous operation of the shutter and the power control system.

3.2   Waveguides fabrication

When an ultra-short laser pulse is focused inside a transparent material the intensity reached in the focal volume can be high enough to induce nonlinear absorption through a combination of multiphoton absorption, avalanche ionization and tunnelling ionization [**?**]. If enough energy is deposited in the material through this nonlinear absorption, permanent structural changes are induced only in the focal volume. Therefore, by simply translating the sample with respect to the focus and using a continuous train of pulses it is possible to induce permanent refractive index changes in the material in a reproducible and controlled manner. In this work this technique was used in order to fabricate the optical waveguides structures inside different transparent materials.

In Fig. 3.1 the experimental arrangement used for the fabrication of the waveguides is shown. A femtosecond laser system (Spitfire, Spectra Physics) that emits 120 femtosecond pulses at a central wavelength of 800 mm with a 1 KHz repetition rate was used. A motorized half-wave plate followed by a linear polarizer, and a calibrated neutral density filter, were used to fine tune the pulse energy. For the waveguide inscription transversal geometry was used in which the laser beam propagation is perpendicular to the written structures [62]. The beam was focused through a lens or microscope objective; the numerical aperture of the lens is chosen depending on the required design of a structure in particular. The sample is placed in a 3-axes motorized stage (Micos, PLS-85) with a resolution of 0.1 μm and it is moving with a constant speed along the *y* axis and perpendicular to the incident beam.
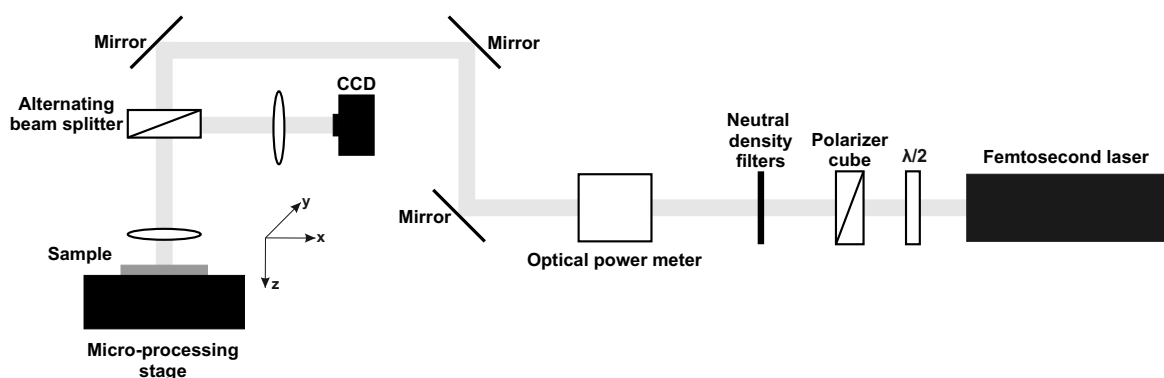
Fig. 3.1 Experimental setup for the fabrication of optical waveguides using a fs laser. The sample is perpendicularly moved with respect to the laser beam

3.3 First considerations

The fabrication of optical waveguides by laser irradiation consists firstly in finding the fabrication parameters that are able to produce the desired kind of modification (Type I, Type II), maximize or minimize the effect of the induced stress and prevent mechanical fractures in the sample. The fabrication is carried out in a first instance by testing the effect of laser irradiation at different pulse energies, sample depths and focusing conditions. Once, these tests have been performed and analyzed with different microscopy techniques, the structures are produced according to the most suitable parameters for the type of technique to be used. However, there is important considerations to take into account before to start a laser irradiation. Before a laser irradiation, a design of a prototype that includes all the preconceived ideas is made. Once, the design has been simulated or proved, the next step is to elaborate a program that prints, all the necessary instructions to carry out the movement of the micropositioners in order to generate the desired structure. After that, the first step in laser microprocessing of materials, is a correct localization of the waist of the focused beam at the surface of the sample. This process ensures a correct position of the sample with respect to the focused beam to generate an homogeneous laser scanning.

3.4 Localization and visualization of the focused beam

As previously mentioned, when working in laser materials processing, one of the fundamental aspects consists in the localization and visualization of the waist of the focused beam at the surface of the irradiated material; this allows a correct positioning of the sample with respect to the beam ensuring that the sample is perpendicular to the laser beam. For this purpose, an imaging system formed by the microprocessing lens a beam-splitter and a CCD camera with an objective focused to infinite is usually employed. The theory of operation is based on Gaussian beam propagation in which, the wavefront in the beam waist is plane. Therefore, a reflection produced by a planar surface situated in this position makes that the reflected beam follows exactly the same path and form of the incident beam. If the reflecting surface is slightly displaced with respect to the beam waist, of the order of a Rayleigh length (resolution of the system), the incident wavefront over the surface is not plane, therefore, the reflected light will make that the beam converge or diverge (see Fig. 3.2).

The schematic set-up used to locate the beam waist over the surface sample, while this is moved along the beam propagation axis is shown in Fig. 3.3. The set-up is composed by two convergent lenses, the first one that focus the beam over the sample (microprocessing lens) and a second one that acts as an objective focusing the reflected beam over a CCD camera. Once

the beam has been localized the sample is translated along the direction of propagation (z axis) until the waist of the beam is localized, i.e. where the spot size in the CCD camera is minimum.
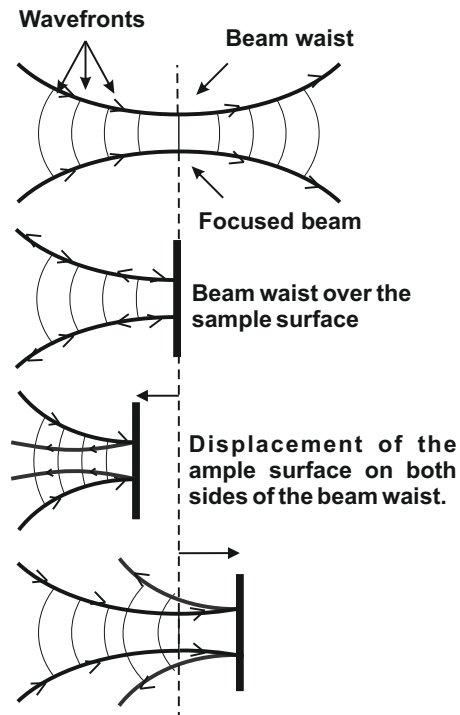
Fig. 3.2 Reflection of a Gaussian beam over a surface located in different positions of the beam path.
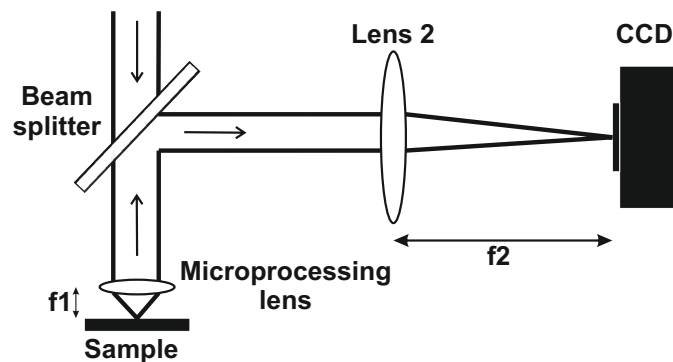
Fig. 3.3 Schematic diagram of the experimental setup for the location and visualization of the waist beam over the sample.

3.5 Optical waveguide characterization

The characterization of optical waveguides in an essential step in the fabrication process. It is necessary to evaluate and corroborate that the fabricated waveguides exhibit attractive characteristics for some specific applications. Some of the parameters that are usually characterized are: propagation loss, coupling loss, as well as the guided-modes, mode profiles, the index refractive contrast etc. This characterization is generally used as a feedback to improve the design and the fabrication process of the waveguides. In this section, the main characterization techniques used in the development of this work will be introduced.

3.5.1 Coupling light into waveguides

The most extensively used method for coupling light into waveguides due to its simplicity, efficiency and versatility is the *end-fire coupling* technique. This technique consists in launching a beam from a source into one end face of the waveguide by means of a microscope objective or an optical fiber. In both of the cases the guided light from the opposite end is recorded using a microscope objective in combination with a CCD camera as it is shown in Fig. 3.4. One of the main features of the end-fire coupling is the fact that allows to visualize and confirms the guiding properties through the visualization of the supported modes.

The experimental setup is typically composed by three micro-positioners stages. All the optical components as the microscope objectives and the sample with the fabricated waveguides are separately mounted in the micro-positioners in order to achieve a stable alignment. The whole process of coupling consists in manually positioning the waveguides. Firstly, the output face of the crystal is focused by moving the positioner and using as a reference the edge of the sample. This can be done by either illuminating with a white light source or a beam laser focused on the input face of the sample. In a first instance, the cross-section image of the sample can be visualized onto a screen instead the CCD. Thus, by moving the sample through its positioner, it is possible to localize and see the fabricated structures. Then, by translating the sample with respect to the focused input beam it is possible to observe very intense "points" of light that correspond with the modes of the waveguide.
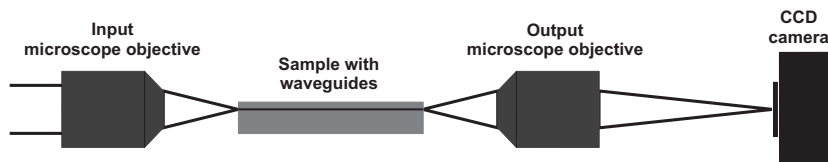
Fig. 3.4 Schematic diagram of the end-fire coupling.

3.5.2 Loss measurements

Loss in a waveguide is one of the most important parameter due to the fact that allows to determine if a waveguide is usefulness for a specific application. In general, loss in optical waveguides are mainly due to four main terms [110]:

- **Propagation losses**. These could either be due to inherent effects of the material as absorption, scattering, radiation, and impurities of the material due to their fabrication process or could be due to non-linear effects. These optical phenomena have an impact on the quality of the waveguides and depend on the fabrication parameters.

- **Fresnel losses**. These are produced by the reflections generated at the input and output ends of the waveguide and they are always present at the interface between two media having different refractive indices.

- **Coupling loss**. This is due to the degree of similarity between the mode of the excitation source and the mode of the waveguide. The difference between the distributions of intensity of the transverse fields of the incident beam and the mode of the waveguide causes that the coupling or overlapping of the modes would not be complete. As a consequence, there is a lost of power.

- **Misalignment**. This is due to the relative position of the optical axis of the incident beam with respect to axis of the waveguide.

In conclusion, loss produced in a waveguide can be summarized as the sum of coupling loss, loss produced by the propagation of light in the structure, Fresnel losses, and the misalignment on each degree of freedom between the optical axis of the excitation source with respect to the axis of the waveguide. Assuming that loss induced by misalignment are experimentally minimized by maximizing the output power (i.e. angular and longitudinal contributions may be considered negligible), the insertion loss are given by [59]:

$$\text{Insertion loss (dB)} = \text{coupling loss (dB)} + \text{propagation losses (dB)} + \text{Fresnel losses (dB)}$$

$$(3.1)$$

Insertion losses are estimated by calculating the transmittance of the waveguide taking into account transmittance of the optical components. Therefore, by measuring the output P_{out} and input P_{in} power of the system the insertion losses can be easily estimated by Eq. (3.2).

$$L_{in}(\text{dB}) = -10 \log \left(\frac{P_{out}}{P_{in}} \right) \tag{3.2}$$

For the coupling efficiency between modes the well-known overlap integral is used, given by [110]:

$$\eta(\text{dB}) = -10 \log \left(\frac{\iint |E_1 E_2|^2 dx dy}{\iint |E_1|^2 dx dy \iint |E_2|^2 dx dy} \right), \tag{3.3}$$

with x and y being the transverse coordinates, which expresses the coupling between the electric fields $E1$ and $E2$ of the excitation source and the waveguide modes, respectively.In practice, the use of (3.3) can be complicated and time consuming. This can be simplified in a practical expression based on the Gaussian beams. If the mode profile is eccentric but symmetric and assuming perfect alignment, which is a good approximation in the case of this work, the overlap integral gives [111]:

$$\eta(\text{dB}) \approx -10 \log \left[\frac{4}{\left(\frac{\omega_x}{\omega_0} + \frac{\omega_0}{\omega_x} \right) \left(\frac{\omega_y}{\omega_0} + \frac{\omega_0}{\omega_y} \right)} \right], \tag{3.4}$$

where ω_0 is the waist of the input beam and ω_x and ω_y are the waist of the propagated modes in the waveguide measured along the horizontal en vertical direction respectively. The waist of the transverse modes is calculated from the images obtained by the CCD (see Appendix ??) On the other hand, Fresnel losses can be obtained from the refractive index of the material through

$$F_{loss}(\text{dB}) = -10 \log[1 - R] = -10 \log \left[1 - \left(\frac{n_0 - n_1}{n_0 + n_1} \right)^2 \right], \tag{3.5}$$

where n_0 is this case, represents the refractive index of air and n_1 represents the refractive index of the material in which the waveguide has been fabricated. It is important to point out that Eq. (3.5) must be expressed as $2F_{loss}$ due to the fact that Fresnel reflections occur in both input and output faces of the waveguide.

Finally, once the contribution of every element of Eq. (3.1) have been determined, propagation losses (P_{loss}) can be easily extracted. This can be either expressed in dB or dB/cm by taking the ratio from the obtained value to that of the waveguide length.

It should be pointed out that this loss characterization is only valid for single mode waveguides. However, there are alternative characterization methods that can be used in order to characterize multi-mode waveguides. In the next section a suitable method that can be applied to both single and multi-mode waveguides is introduced.

3.5.3 Scattered light imaging method

Another technique that can be applied for measuring the propagation loss in waveguides is the scattered light imaging method, which considers that scattering centers are uniformly distributed along the waveguide, where light is propagated [112, 113]. The method consists in recording the exponential decaying light scattered along the waveguide by placing a top view imaging system as it is showed in Fig. 3.6. After the light propagation is imaged, the software *imageJ* is used to extract the information of the scattered light intensities versus position or propagation length. In other words, a intensity profile is taken from the image. The propagation of light can be defined by the equation:

$$I(z) = I_0 e^{-\alpha z}, \tag{3.6}$$

where I_0 is the incident intensity at the waveguide input at position ($z = 0$), z is the coordinate along the propagation direction, and α is the loss coefficient (propagation loss) expressed in cm^{-1}. In order to extract the loss coefficient, Eq. (3.6) can be rewritten taking the natural logarithm of both sides as:

$$\ln(I) = \ln(I_0) - \alpha z \tag{3.7}$$

The propagation loss can be then easily calculated as the slope of a linear function of $\ln(I)$ by simply fitting a linear function to the data. It is important to point it out that a calibration with a scale is performed for the characterization in order to obtain α in units of loss/cm instead loss/pixel. Once the a vector of integrated intensity versus position (intensity profile) has been generated, and the propagation loss has been extracted, this can be converted to units of dB/cm by using the following equation [114]:

$$Loss\left(\frac{dB}{cm}\right) = 4.34\alpha\left(cm^{-1}\right),\qquad(3.8)$$

Alternatively, the propagation loss in units of dB/cm can be directly obtained from the linear fitting by changing the axis of ordinates of the intensity profile into dB. Fig 3.5 shows an optical image of a waveguide where it is possible to observe the exponential decaying light scattered together with its intensity profile used for the calculation of the propagation loss.
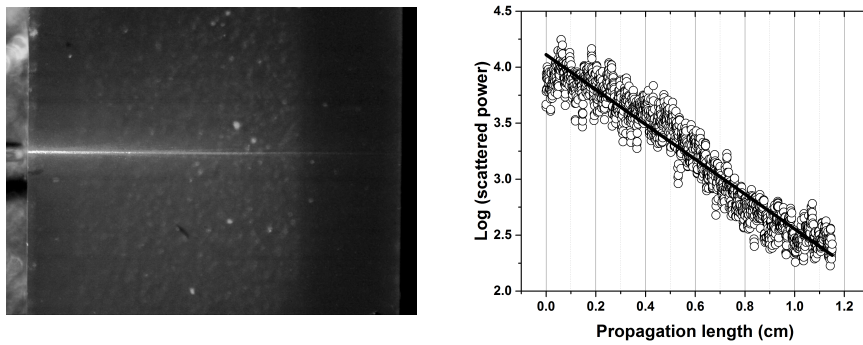
Fig. 3.5 Scattered light image together with its associated intensity profile and linear fit.

3.5.4 Waveguide characterization setup

A schematic diagram of the waveguide characterization used in this work is shown in Fig. 3.6. A continuous wave laser beam with a wavelength of 633 nm from a linearly polarized single mode He:Ne laser is used. In order to evaluate the optical modes and losses for both TM (vertical) and TE (horizontal) orthogonal polarizations a half-wave plate is used to control the polarization of the beam incident on the waveguide. An iris is used to control the size of the incident beam and hence the numerical aperture (NA) of the beam; this is very useful when white light is coupled into the waveguides. A beam splitter directs the beam onto a moveable screen used to monitor that the beam reflected by the sample is collimated (see Section 3.4). This step is carried out to verify that the beam is being focused at the input face of the waveguide. The laser beam is focused through a 10X microscope objective. The waveguide modes are recorded by imaging the output face of the waveguides through a 20X microscope objective onto a CCD camera. Input and output focusing lenses are placed in 3-axis micropositioners stages while the sample is placed in a 5-axis micropositioners for a good optimization of the output power.
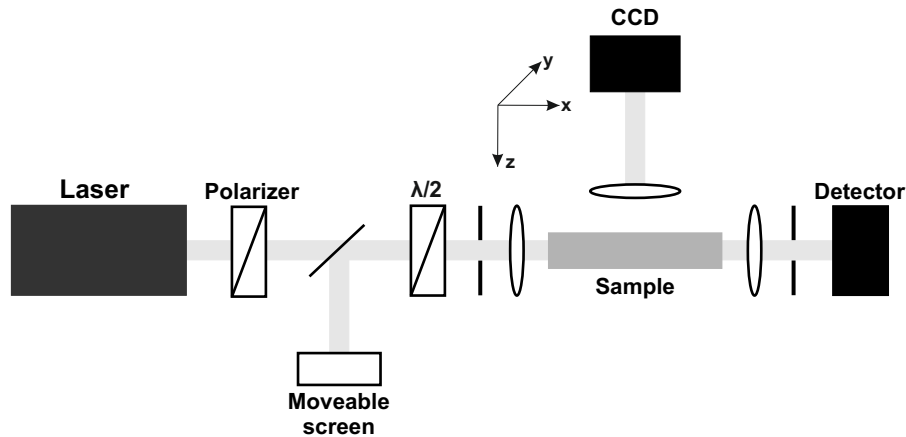
Fig. 3.6 Schematic diagram for the characterization of the written structures.

Loss measurements were conducted by using a calibrated photodiode. In this case, an iris was placed in front of the detector in order to suppress light transmitted through the bulk outside of the waveguide. The polarization dependence of the waveguides was carried out employing a half-wave plate to control the polarization of the incident laser beam and recording the output power at every position of the plate. This can be also carried out by recording the mode images on the CCD and making an image processing to obtain the intensity of the illuminated pixels. For this purpose, the free software *ImageJ* can be used, the process is explained in Appendix??.

Insertion losses were always obtained by measuring the input and output powers, taking into account transmission loss of the microscope objectives. Fresnel reflections at the crystal interfaces were also taken into account. In order to obtain a further characterization of loss, the scattered light imaging method was employed. For a more precise visualization of the waveguide modes, all the images were processed using an algorithm written in *MATLAB*. The code can be found in the Appendix (??). Fig. 3.7 shows an image of a mode before and after the imaging process. It is important to point out that saturation in images must be avoid in order to obtain a correct processing of the images.

3.6 Refractive index measurements

3.6.1 Refractive index contrast

Determination of the refractive index contrast (Δn) produced in the waveguides by the femtosecond laser inscription is based on a trigonometric method which involves an experimental estimation of the numerical aperture (NA) of the waveguide from the far-field pattern [115].
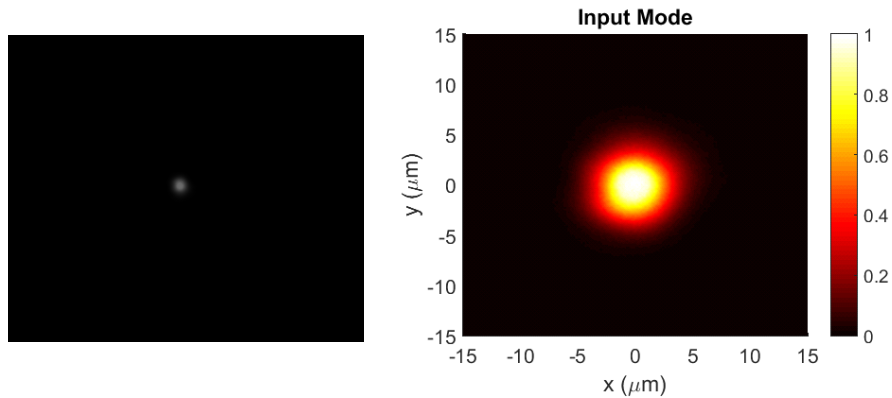
Fig. 3.7 Images of a near-field taken with the CCD camera before and after the image processing.

For this purpose, the experimental arrangement for waveguide characterization previously mentioned was used. Once a mode waveguide has been exited and visualized in the CCD, the next step consists in removing one of the microscope objectives and display the far-field pattern from the waveguide on a screen which is positioned a known distance D from the output face of the waveguide. In this case, a CCD camera can be used instead a screen for a more precise measurement. The pattern size A is then measured from the image taken from the CCD by fitting a Gaussian function to its intensity profile. The experimental setup together with an optical image of a far-field pattern of a waveguide is shown in Fig, 3.8. The numerical aperture is estimated from the trigonometrical relationship given by Eq. (3.9) [115], where A represents the $1/e^2$ half-width of the measured intensity profile. Finally, assuming in a rough estimation a step-index profile the refractive index contrast can be calculated from Eq. (3.10) [116], with θ as the maximum incident angle at which the transmitted power occurs without any change, while n, in a first approximation, is the refractive index of the material.
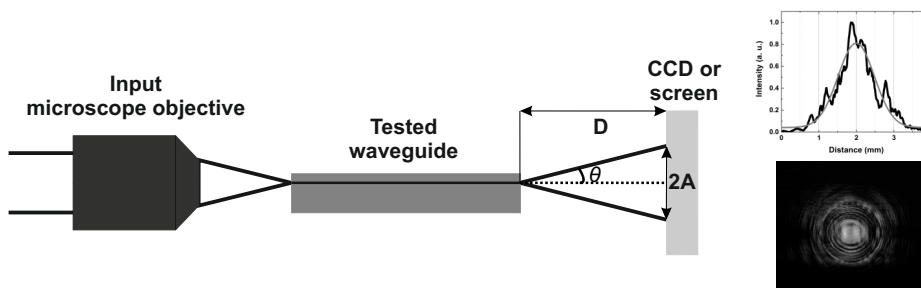
Fig. 3.8 Experimental arrangement for trigonometric waveguide numerical aperture measurement.

$$NA = \sin\theta = \frac{A}{[A^2 + D^2]^{\frac{1}{2}}} \tag{3.9}$$

$$\Delta n \approx \frac{\sin^2\theta}{2n} \tag{3.10}$$

3.6.2   Inverse Helmholtz technique

The inverse Helmholtz technique also known as the propagation-mode near-field method [117], is a non-destructive method that allows to estimate the refractive index distribution of a waveguide from the mode field intensity by an inversion of the Helmholtz equation [118]. That is to say, the guided modes of a waveguide can be found by solving the Helmholtz equation, which shows the relationship between the refractive index profile of a waveguide and the field distribution of the modes. Since the modes are a solution of the Helmholtz equation, by taking an image of the near-field intensity modes, the refractive index distribution can be estimated carrying out an inverse process. Some of the main advantages of this technique is the fact that does not require a previous knowledge of the refractive index distribution as well as special symmetries of the cross section of the waveguide. Nonetheless, this technique can only be used for single mode waveguides where only the fundamental mode is excited and for small magnitudes of the refractive index contrast.

Considering a single mode optical waveguide with small Δn, the optical field strength of the fundamental mode of excitation, $E(x,y)$ can be describe by the Helmholtz equation or also known as the scalar wave equation given by [119]:

$$\nabla^2 E(x,y) + \left[k^2 n^2(x,y) - \beta^2\right] E(x,y) = 0, \tag{3.11}$$

where $n(x,y)$ is the refractive index profile transversely across the waveguide, β is the propagation constant given by $\beta = n_{eff}k$, with n_{eff} as the refractive index of the guided mode and $k = \frac{2\pi}{\lambda}$ as the free space wave number. Rearranging the Helmholtz equation for $n(x,y)$ it gives:

$$n^2(x,y) = \left(\frac{\beta}{k}\right)^2 - \frac{\nabla^2 E(x,y)}{k^2 E(x,y)} \tag{3.12}$$

By measuring the near-field intensity of the mode $I(x,y)$ the normalized E-field distribution $E(x,y)$ of the mode can be deduced neglecting the spatial phase of the field. Furthermore, making the substitution for intensity, $E(x,y) = \sqrt{I(x,y)}$, and introducing the refractive index profile through $n(x,y) = n_B + \Delta n(x,y)$ for small $\Delta n(x,y)$ [120]:

$$\Delta n(x,y) = \frac{\beta^2}{2n_B k^2} - \frac{n_B}{2} - \frac{\nabla^2 \sqrt{I(x,y)}}{2n_B k^2 \sqrt{I(x,y)}},$$

(3.13)

where the first two terms on the right hand are an unknown constant. Therefore, the mode field intensity $I(x,y)$ can be used in order to determine the refractive index profile $\Delta n(x,y)$ of the waveguide with an arbitrary constant. This constant can be found by matching the refractive index of the waveguide to that of the bulk material (n_B) [121]. Thus, under the approximation that Δn is small and $n_B \approx \frac{\beta}{k} \approx n_{eff}$, Eq. (3.13) yields:

$$\Delta n(x,y) = \frac{\nabla^2 \sqrt{I(x,y)}}{2n_B k^2 \sqrt{I(x,y)}}$$

(3.14)

As it was previously mentioned this method is based on the measurement of the near field intensity mode of the waveguide. Using the definition given by [122], Eq. (3.14) can be adapted to the measured mode intensity, $I(x,y)$, by means of the normalized electric field intensity given by:

$$A(x,y) = \sqrt{\frac{I(x,y)}{I_{\max}}}$$

(3.15)

Consequently, Eq. (3.14) can be rewritten as [123]:

$$\Delta n(x,y) = \frac{\nabla^2 A(x,y)}{2n_B k^2 A(x,y)}$$

(3.16)

It is important to note that due to the second order differential in Eq. (3.16), the calculated refractive index profile is highly sensitive to noise in the measured data. Hence, multiple images of the near-field mode should be taken and averaged in order to obtain more precise refractive index profiles. Moreover, the measured data should be smoothed to remove high frequency noise by using 2D low pass digital filters, the process is well explained in [122]. In order to calculate the refractive index profile of the structures fabricated in this work, an algorithm was

written in *MATLAB*. The code can be found in the Appendix (??). Fig. 3.9 shows an image of a measured near-field mode profile of a Type II waveguide together with its corresponding refractive index profile calculated by the inverse Helmholtz technique.
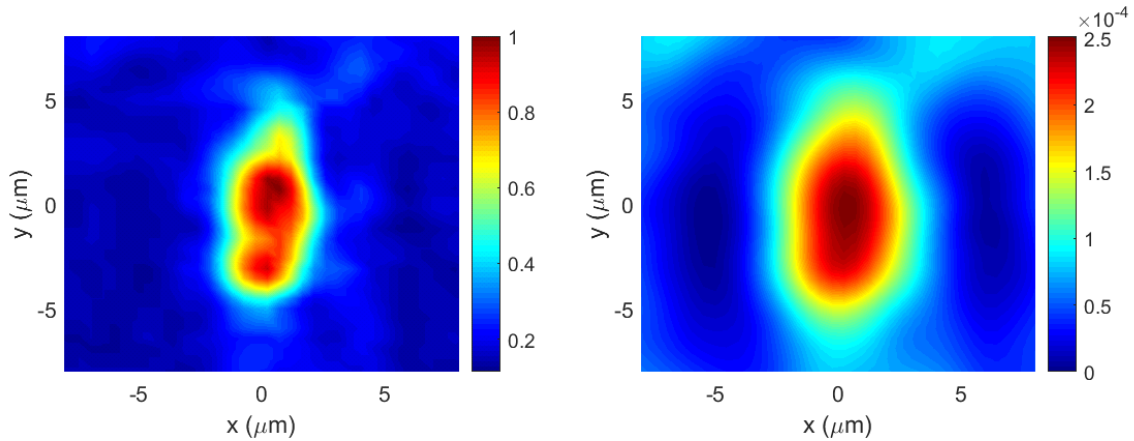
Fig. 3.9 Left: Mesured near-field mode profile of a Type II waveguide. Right: Corresponding refractive index profile recovered by the inverse Helmholtz rechnique.

3.6.3   Waveguide modes simulation

For the modeling of the fabricated optical waveguides the simulation software *COMSOL Multiphysics* was used. This software is based on the *finite element method (FEM)* which is a numerical technique for finding approximate solutions to boundary value problems for partial differential equations [124]. One of the most attractive features of this software is the fact that it does not require an in-depth knowledge of mathematics or numerical analysis. A more detailed description of this modelling software can be found in the *COMSOL Multiphysics References Guide*.

Concerning to the waveguide simulations, depending on the geometry of the structure the simulations were performed by designing a geometry that matched the laser induced tracks of the fabricated waveguide. Fig. 3.10 shows an example of a modeled depressed-cladding waveguide structure with a hexagonal shape. In Fig. 3.10 it is also possible to see an optical micrograph of the cross section of an example of a waveguide fabricated in this work in a YAG crystal. For the modelling of the waveguides the refractive index of each track was assumed to be a real value and uniform across the cross section of a single track. It is important to point it out that in most of the simulations some parameters such as the track size or the refractive index contrast between the cladding and the core Δn were experimentally extracted. The simulation can also be used to corroborate the measured value of Δn. Another important point to take into

account is the fact that a *perfectly matched layer (PML)* was used in the simulations in order to truncate the computational domain and minimize the effects of boundary reflections [125]. For this purpose, a circular PML surrounding the cross section of the waveguide structures was always used as it can be clearly seen in Fig. 3.10. Further information about the simulation process for optical waveguides can be found in the *RF Module Model Library* of COMSOL.
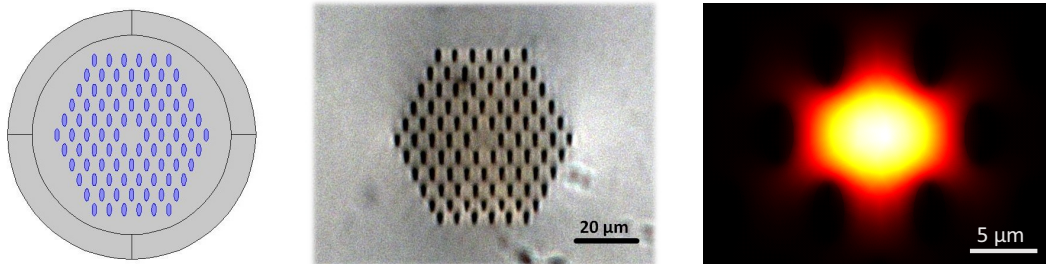
Fig. 3.10 Left: Cross section of a modeled depressed cladding waveguide. Center: Optical micrograph of the cross section of a waveguide structure fabricated in a YAG crystal. Right: Simulated mode.

Chapter 4

Study of nanostructured YSZ ceramic

One of the objectives of this work is based on the analysis of the response of a nanostructured ceramic to ultrashort laser pulses irradiation with the aim to determine its characteristics to be used as an optical material for integrated optics as well as for biophotonic applications. This ceramic is Yttria Stabilized Zirconia (YSZ) which is a material that currently have a wide variety of applications in different areas ranging from biomedicine to engineering and scientific research. Due to its excellent mechanical and chemical properties such as high hardness, high tolerance to thermal shock, high melting point, good phase stability, and excellent oxidation resistance [126], YSZ is used in the fabrications of tooth crowns [127], as a refractory in jet engines [128], thermal barrier coating in gas turbines [129–131], production of solid oxide fuel cell [132], etc. However, only recently has been considered as a material for optical applications [133, 75].

As a matter of fact, this material has been recently proposed as a cranium implant material , enabling the replacement of segments of cranial bone for optical access to the brain to deliver and/or collect light from it [134]. Nonetheless, there is still a lack of knowledge concerning to its optical properties as well as the response to the femtosecond laser irradiation. Therefore, the characterization of its properties will allow to design suitable experiments combining both optical and biocompatibility properties in a reproducible and controlled manner.

In this section, the results of the the response to femtosecond laser irradiation of nanostructured yttria stabilized zirconia (YSZ) ceramic is presented.

4.1   Ceramic fabrication

For the fabrication of the ceramic, commercial nanocrystalline 8YSZ powder (Tosoh Corporation, Tokyo, Japan) with a reported grain size of 50 nm was used. The ceramics were prepared using the current activated pressure assisted densification (CAPAD) technique. These

were prepared in a graphite die with 19 mm inner diameter. Monitoring of the temperature
was carried out by using a ground built N-type thermocouple placed in a hole drilled halfway
through the thickness of the die. The CAPAD process is done in a custom built apparatus
that has been described in [135]. The pressure in the system is raised to 106 Mpa before a
current was applied. Once the pressure has reached, the current heated the sample to 1200
°C using a heating rate of 200 °C/min. Samples were then held for a period of time at final
pressure and temperature. Finally, the samples were polished for optical quality. Fig. 4.1 shows
a SEM image and a photograph of a ceramic. More detailed information about fabrication and
characteristics has been reported in [136]. Tab. 4.1 shows some important characteristics of the
YSZ ceramic.

Table 4.1 Properties and characteristics of the YSZ ceramic

Material	Crystalline structure	Grain size	Fracture toughness
$Z_rO_2 - 8mol\%Y_2O_3$	cubic	50 nm	$3.1 \, MPa \cdot m^{-1/2}$
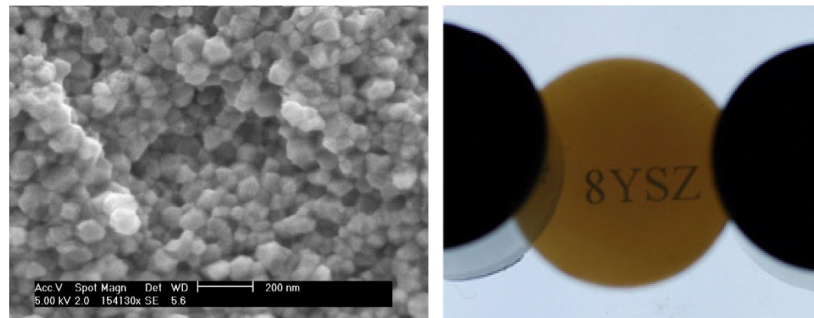
Fig. 4.1 (Left) SEM micrograph of the 8YSZ sample produced via CAPAD with a grain size
of 50 nm (scale bar in the picture corresponds to 200 nm), (Right) Photograph of the same
8YSZ on top of backlit text showing transparency of the ceramic and elevated ≈ 2.5 cm off the
surface. Pictures taken from [135].

4.2   Laser ablation of transparent YSZ ceramic

4.2.1   Motivation

LAser ablation is a process by which it is possible to remove material from the surface of a
sample by means of a focused laser beam. In the case of pulsed lasers, the process is carried
out by controlling parameters of the laser such as pulse energy, pulse duration or focusing

conditions. This precise control makes this technique a valuable tool in research and industrial applications. Consequently, it is always interesting to characterize the ablation characteristics of a material in order to be able to design experiments where the laser ablation is performed to produce the micromachining of a sample for certain applications.

4.2.2   Ablation experiments

The ablation experiments were carried out in the facilities of the *Centro de Láseres Pulsados Ultracortos Ultraintensos* (CLPU) in Salamanca. For this study, a sample annealed in air for 8 hours at 750 °C was used. The ablation tests were performed in air using an amplified Ti:Sapphire laser system, which produced pulses with 120 fs duration, a maximum per pulse energy of 7 mJ, repetition rate of 1 kHz and central wavelength of 795 nm. The laser beam, with a $1/e^2$ radius of 5.5 mm was focused by using a lens with a focal distance of 100 mm. The pulse energy was controlled by an attenuator composed by a half-wave plate and a two Brewster linear polarizers. Several sets of laser irradiations were done in the sample, consisting of pulse trains with different number of pulses (from 5 to 10000). Each set of irradiations was done with a different pulse energy that was varied from 10 to 350 μJ.
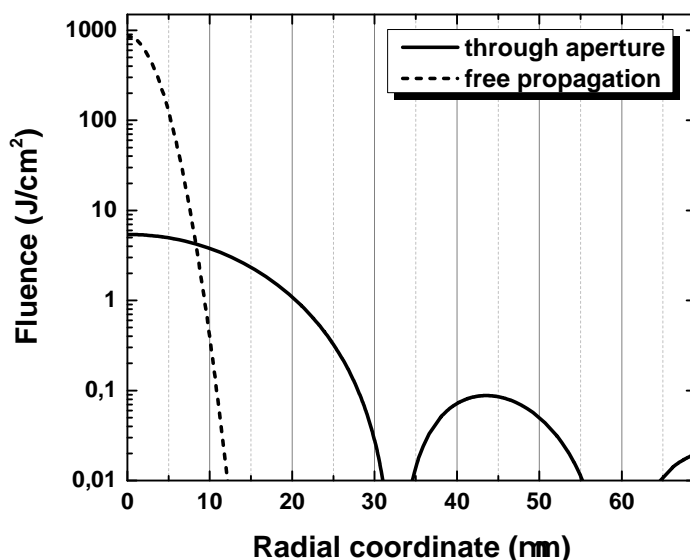
Fig. 4.2 Calculated incident fluence profiles through aperture (solid) and for free propagation (lines) beams respectively for a pulse energy of 350 μJ.

In order to induce symmetric craters with a large diameter, a circular aperture of 3 mm of diameter was placed before the focusing lens. As it is well known a circular aperture blocking a

beam, induces a diffraction pattern (Airy rings). In this case, this can be used to characterize the incident laser beam through the induced ablated craters. When the ablation threshold is below the first diffraction maximum, the first Airy ring is produced on the surface of the sample for a low number of pulses. On the other hand, if the ablation threshold value is higher than the first diffraction maximum, the first maximum appears after a hundred of pulses due to incubation effects or accumulation dependance of damage [137]. Therefore, by measuring the radius of the ablated craters, it is possible to calculate the fluence of the focused beam by directly correlating the measured radius of the craters with the radius of calculated profile fluence [138]. In order to carry out this procedure a simulation of the propagation of a Gaussian beam through a circular aperture and through a lens was made by using Fresnel diffraction. Fig. 4.2 shows the calculated fluence profile for a freely propagated beam and a beam diffracted through a circular aperture for a pulse energy of 350 μJ. As it can be seen, there is a difference of two orders of magnitude between the value of peak fluence for the freely and truncated beam. It is also possible to observe the first maximums of the diffraction pattern with their corresponding values of fluence.

4.2.3   Results and discussion

Ablated craters

Fig. 4.3 shows an optical micrograph of a series of craters made by means of femtosecond pulses in the YSZ sample with applied pulse energy of 350 μJ (5.41J/cm^2). The craters were made by 5, 10, 20, 50, 100, 1000 and 10000 pulses beginning from left to right. It was found as a minimum condition to induce ablation over the surface of the sample a pulse energy of 80 μJ (1.23 J/cm^2) with a number of pulses of 10000. An important characteristic that was found over the ablated craters was the fact that for a number of pulses between 50 and 10000 color rings surrounding the craters begin to appear. The colors could be due to an oxidation process where each color corresponds to a different oxidation phase of the material, induced by the concentric rings of the diffraction pattern, which have a corresponding fluence below the ablation threshold; heat provided by the pulse laser and oxygen taken from the environment contribute for the oxidation of the material. Another explanation of the colors could be a compaction of material due to mechanical waves. As it is well known, ultrahigh peak irradiances are reached by ultrashort laser pulses. Nonlinear absorption, multiphoton ionization and plasma generation are the typical dominating processes of the interaction, leading to high temperatures and pressures. If these temperatures occur inside the sample, the heated material expands, creating a pressure front or even a shock wave. This induces a strain distribution around the irradiated region, leaving behind a local density change in the material. Consequently, colors are only present

for craters made by a large number of pulses mainly due to the larger depth of these craters. Consequently, a greater amount of evaporated material (ablation) cannot escape to the exterior creating more pressure surrounding the walls of the craters. One last explanation could be a deposition of ablated material over the surface of the sample. The evaporated material forms a transparent thin layer over the surface, producing an interference pattern.
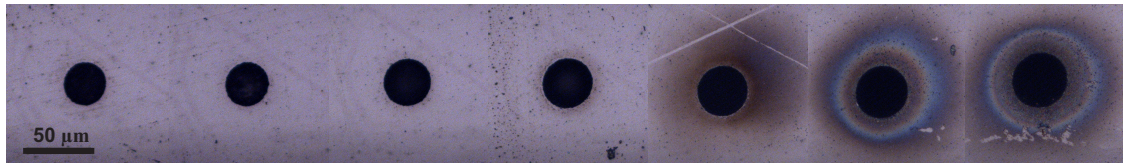
Fig. 4.3 Optical micrograph of ablation craters made by 5, 10, 20, 50, 100, 1000 and 10000 pulses in YSZ ceramic for a pulse energy of 350 μJ and an aperture with a diameter of 3mm.

Ablation threshold

Fig. 4.4 shows the calculated fluence profile together with the measured crater radius and its corresponding threshold fluence value. For each incident pulse energy, the measured crater radius is represented in the fluence profile as a point on the corresponding curve, with the horizontal axis given by the measured radius, and the vertical axis giving the corresponding fluence at this radius. In order to determine the ablation threshold, a horizontal line was fitted to the experimental points, being the ordinate of this the ablation threshold. This method was used to find the ablation threshold for a series of different number of applied pulses. Tab. 4.2 lists the found ablation threshold values for different number of applied pulses. As expected, the ablation threshold tends to decrease as the number of pulses increases, which can be explained by the effect of damage accumulation or incubation process [137].

Table 4.2 Values of ablation threshold for different number of applied pulses.

Number of pulses	Ablation threshold (J/cm^2)$\pm$ 0.03
5	1.97
10	1.85
20	1.53
50	1.22
10^2	1.21
10^3	1.00
10^4	0.92
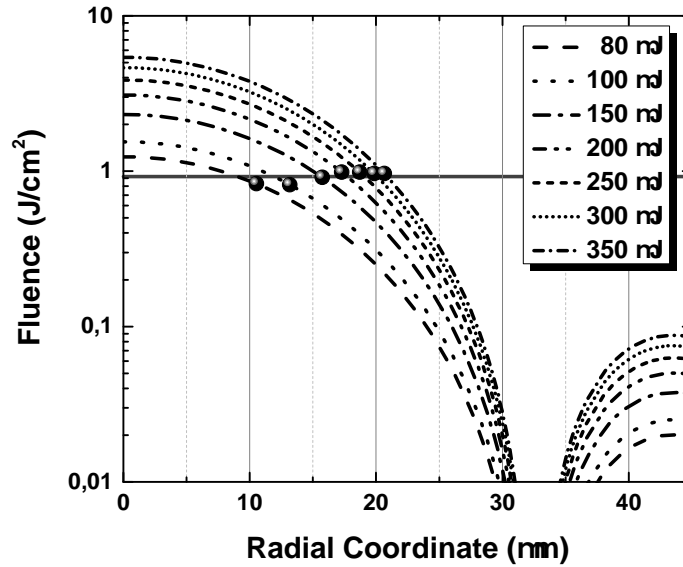
Fig. 4.4 Calculated fluence profiles, measured crater radius and their corresponding threshold fluence values for 10000 applied pulses.

Single-shot threshold, incubation coefficient and ablation rates

Once the threshold fluence for a different number of applied pulses has been determined, the incubation coefficient can be calculated from obtained data by fitting the equation [139]:

$$F_{th}(N) = F_{th}(1) \cdot N^{S-1}, \tag{4.1}$$

where $F_{th}(N)$ is the fluence ablation threshold for a given number of applied pulses, N is the number of pulses, $F_{th}(1)$ is the single-shot threshold fluence, and S the incubation coefficient, which quantifies or gives a measure of the degree of incubation behavior. Fig. 4.5 shows the measurements of threshold fluence values versus the number of applied pulses together with the fitting of the data to the Eq.(4.1). Another important parameter to determine is the single-shot ablation threshold which indicates the minimum fluence value to induce ablation over the surface of the sample with a single pulse. This is generally found by making irradiations using a single pulse and analyzing the irradiated zone. In this case, laser system only was able to delivery a minimum of 5 pulses. Therefore, in order to obtain the single-shot ablation threshold, the single-shot fluence threshold was obtained from the fit of Eq.(4.1) to the data.

Depth of the craters was estimated by using an optical microscope, by focusing respectively on the edge and the bottom of each ablation crater. A $100 \times$ microscope objective was used to
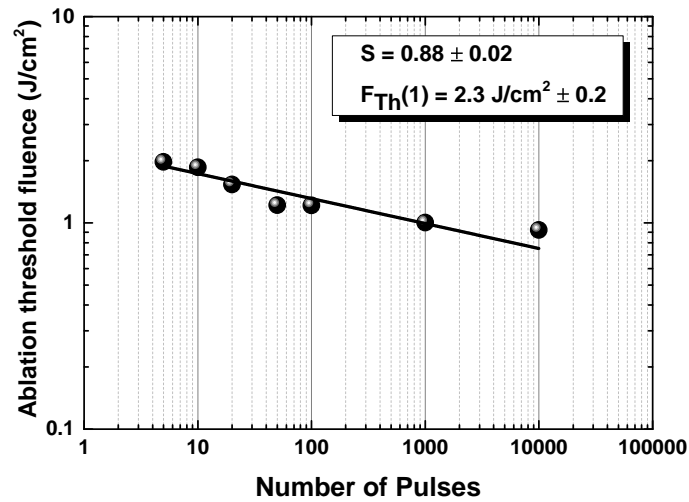
Fig. 4.5 Ablation threshold fluence versus the number of applied pulses together with the best fit values of incubation coefficient and single-shot ablation threshold.

this end in order to minimize the error when focusing a given position of the sample. Measuring of the depths of the ablation craters gives important information about the response of the material to femtosecond laser irradiation. By plotting the depth as a function of the number of applied pulses, the average amount of removed material can be found. Fig. 4.6 shows the measured ablation depths versus the number of applied pulses for a peak fluence of 5.41 J/cm^2 (350 μJ). As it can be seen there is a linear dependence with respect to the number of pulses. Therefore, from the slope of the fitting line, the so-called ablation rate can be determined at the given fluence. It is important to point it out that craters made by 1000 and 10000 pulses were not taken into account due to we could not obtain a precise measurement due to their larger depth. Results of the ablation rate for different values of applied energy are presented in Tab. 4.3.

Table 4.3 Values of ablation rates for different peak fluences.

Peak fluence (J/cm^2)	Ablation rate (nm/pulse) $\pm$ 7.0
2.31	199.0
3.09	276.1
3.86	293.9
4.63	346.7
5.41	347.3
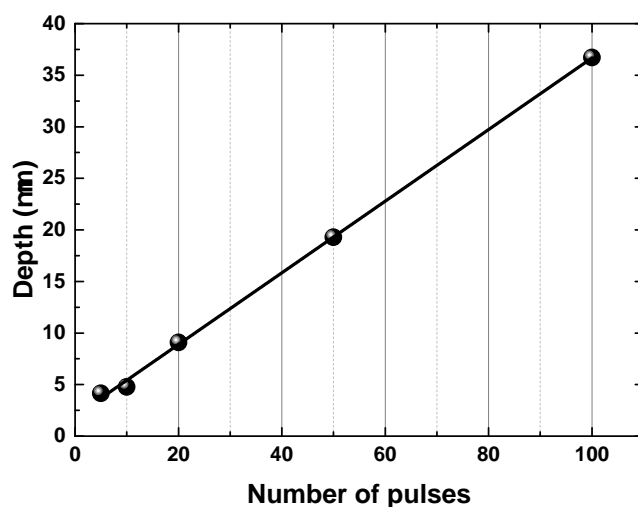
Fig. 4.6 Depth of ablation craters versus the number of applied pulses for a peak fluence of 5.41 J/cm^2 (350 μJ).

4.2.4   Conclusion

In summary, a femtosecond laser ablation study of the transparent nanostructured YSZ ceramic was carried out. Parameters as the ablation threshold from the measurements of the ablated crater diameters as a function of the applied pulses using a diffracted Gaussian beam was determined. The incubation coefficient as well as the single-shot threshold were also found. Finally, from the measurements of the ablated hole depths, the ablation rate for different values of applied fluence were also found . All of these measurements provide important information on the material response to femtosecond laser irradiation allowing the development of high precision ablation experiments in the YSZ ceramic.

4.3   Nonlinear optical properties of YSZ ceramic

4.3.1   Motivation

In the last years, the interest in finding optical materials that possess nonlinear optical properties has attracted a lot of interest mainly due to the possibility to use them in the development of devices that can be incorporated to conventional optical communication systems. Materials that exhibit this kind of properties are very attractive because of their potential for applications such as three dimensional optical data storage, two-photon fluorescence imaging, optical power limiting, optical modulation, optical switching, optical signal reshaping, stabilizing fast fluctuations of laser power, telecommunications, human eye protection etc. [140].

In this section, a study of nonlinear optical properties of nano-structured Yttria stabilized Zirconia (YSZ) ceramic is presented. The nonlinear absorption and refraction coefficients were resolved using the Z-scan technique with an amplified femtosecond laser. Samples with different annealing time were used in order to determine the impact over the nonlinear optical properties of the ceramics. Components of the complex third-order optical susceptibility were also estimated.

4.3.2   The Z-scan technique

Different techniques to characterize the nonlinear optical properties of materials such as third harmonic generation [141, 142], degenerate four-wave mixing [143, 144], interferometry techniques [145], beam self-bending [146], etc., have been developed and each of them have their own difficulty and exactitude, in addition to provide distinct information about the nonlinear optical properties of a given material. In spite of this, just a few techniques provide information about the components of the nonlinear refraction and absorption in a fast and simple manner and with a high degree of accuracy. One of the most famous and used because of its simplicity and versatility and due to it allows to determine the sign of the nonlinearity with only observe the experimental data without the need of any mathematical method, is the well-known Z-scan technique, developed by Shake-Bahae et al. [147] in 1990. The Z-scan technique is based on phase changes produced by the nonlinear propagation inside a transparent material, which are translated to energy changes measured by a detector in the far field. The changes, induced by nonlinear effects, are produced by moving the sample through the propagation axis of a focused Gaussian beam. In other words, the transmittance of the sample is recorded as a function of the sample position relative to the focus beam. When an aperture is placed in front of the detector (Closed Z-scan) the system is sensitive to phase changes; due to the nonlinear refraction the material acts as a lens, focusing and defocusing the beam as the sample is moved

through the focus. This is traduced as a change in transmittance in the field of the aperture, in this case the system is sensitive to both nonlinear refraction and absorption. On the other hand, if the aperture is removed (Open Z-scan) the system is only sensitive to changes caused by nonlinear absorption, hence, the nonlinear absorption coefficient can be inferred from the experimental data. Fig. 4.7 shows the schematic of the experimental setup of Z-scan.
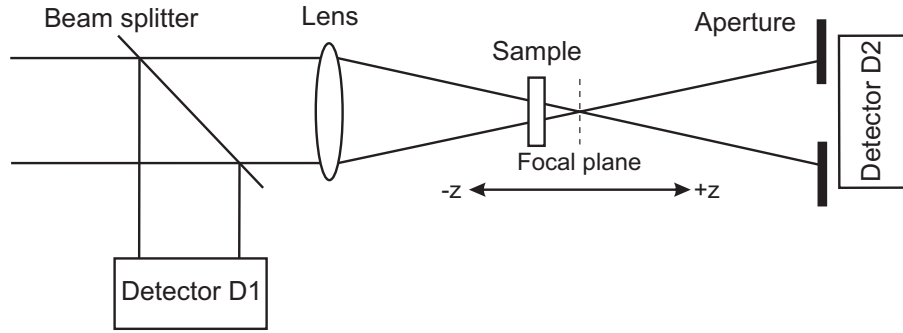
Fig. 4.7 Schematic of the experimental setup of Z-scan, where the transmittance is given by the ratio of D2/D1 as a function of the sample position.

When a Z-scan experiment is carried out the acquired data or curve correspond to the normalized transmittance $T(z)$. This is the transmittance of the sample as a function of its position relative to the beam focus, for the case of an open Z-scan this is given by the relation [147]:

$$T(z) = \frac{1}{Aq_0(z)} \int_{-\infty}^{\infty} \ln[1 + q_0(z) f(\tau)] d\tau, \tag{4.2}$$

where $f(\tau)$ is a function of time that describes the temporal profile of the laser pulse which can be $f(\tau) = e^{-\tau^2}$ or $f(\tau) = sech^2(\tau)$ for a Gaussian and hyperbolic secant pulses respectively. A is a normalization constant $f(\tau) = \int_{-\infty}^{\infty} f(\tau) d\tau$ equal to $\sqrt{\pi}$ for Gaussian and 2 for hyperbolic secant pulses, while $q_0(z)$ is a parameter that characterizes the strength of the nonlinearity given by

$$q_0(z) = \frac{\beta I_0 L_{eff}}{1 + z^2/z_R^2}, \tag{4.3}$$

where β is the nonlinear absorption coefficient of the material, I_0 is the peak irradiance at the focus and $L_{eff} = (1 - e^{-\alpha L})/\alpha$ is the effective propagation length of the material which is related to the linear absorption coefficient (α) and the thickness sample (L). If linear absorption of the sample at the used wavelength is negligible $L_{eff} \approx L$. By using Eq.(4.2) and Eq.(4.3) the nonlinear absorption coefficient β can be determined from the experimental data measurements of the transmittance. The parameter $q_0(z)$ is obtained by fitting Eq.(4.2) to the experimental data and then β can be ambiguously deduced by using Eq.(4.3). However, the numerical solution of Eq.(4.2) is a complicated procedure making the analysis of Z-scan difficult and time-consuming. Alternatively, a criterion that can be assumed is that of a temporally square profile, in which the temporal dependence of the pulse can be omitted. Then the normalized transmittance can be expressed as:

$$T_{open}(z) = \frac{\ln[1 + q_0(z)]}{q_0(z)}, \tag{4.4}$$

On the other hand, the normalized transmittance for a closed Z-scan experiment in its simplified form is given by [148]

$$T_{closed}(z) = 1 - \frac{4x(\Delta\Phi_0)(1-S)^{0.25}}{(x^2 + 9)(x^2 + 1)}, \tag{4.5}$$

with $x = z/z_R$, S the aperture transmission and the on axis phase shift defined as

$$\Delta\Phi_0 = \frac{2\pi I_0 L_{eff} \gamma}{\lambda \sqrt{2}}, \tag{4.6}$$

where I_0 is the on axis irradiance at focus (i.e., $z = 0$), λ the wavelength of the laser and γ is the nonlinear refraction coefficient given in m^2/W.

4.3.3   YSZ samples

It was previously reported that linear optical properties of this material such as linear absorption coefficient, depends on oxygen stoichiometry [136]. This stoichiometry can be readily controlled by the exposure of the samples to reducing or oxidizing atmospheres. In this case in particular, annealing the YSZ ceramics in air, diffuses oxygen back into the sample, removing the oxygen vacancies which induce a chance in the linear optical properties of the samples when these are annealed for different times. In order to evaluate the effects of annealing on

the nonlinear optical properties of the ceramics we used samples with different annealing time. Fig. 4.8 shows samples at different annealing times.
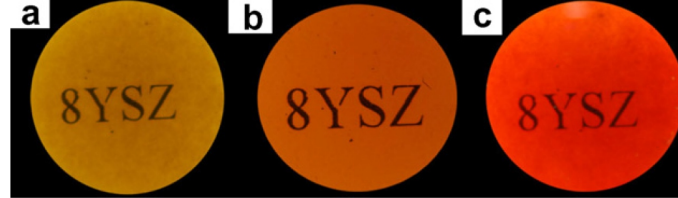
Fig. 4.8 Photograph of YSZ ceramics on a light table on top of text showing varying colors of samples held for various annealing times. Picture taken from [135].

4.3.4   Z-scan characterization

Z-scan experiments of the ceramics were performed using an amplified Ti:Sapphire laser with a central wavelength of 795 nm, repetition rate of 1 KHz, a maximum per pulse energy of 1 mJ and a pulse duration (FWHM) of about 120 femtoseconds. The laser beam was focused by using a converging lens with a focal distance of 20 cm. A diaphragm was place before the lens in order to approximate the beam to a truncated Gaussian and control the value of the Rayleigh length. The laser beam waist (ω_0) was estimated to be about 25 μm (HWe^{-2}M) with a corresponding Rayleigh length (z_R) of 2.5 mm. Samples with thickness of about 0.8 mm (less than Rayleigh length) were used in order to simplify experimental data analysis [147]. Better results were found for experiments carried out with an input irradiance from 1.3×10^{11} W/cm^2 to 7.1×10^{11} W/cm^2 corresponding to a per pulse energy between 1.5 and 8 μJ. Samples were moved across the propagation axis (z axis) by a computer controlled stage. The z-scan setup was calibrated with a sample of fused silica, whose β and γ are known from literature.

The experimental setup used for the measurements of the third-order optical nonlinearities is similar to that shown in Fig. 4.7. In this case, the arrangement allows the simultaneous monitoring of the far-field beam intensity directly transmitted by the sample (open Z-scan), and the far-field light transmitted by the sample through a diaphragm (closed Z-scan) placed at a distance of more than 4 times away from the focal plane. The transmitted light in both open and closed Z-scan was detected by a CCD camera that spatially integrates and translates the intensity images to optical power.

4.3.5   Results and discussion

Fig. 4.9 shows a typical experimental open Z-scan curve for a ceramic with 10 min annealing time together with the fitting curve and the obtained best value of the nonlinear absorption. It

can be seen that there is a minimum of the transmittance on focus in contrast with the position of the sample away from it. This curve is well known and studied and in literature [147] and corresponds to nonlinear absorption and sometimes called two-photon absorption (TPA). Therefore, according to Fig. 4.9, it is possible to assure that this material exhibits TPA. It was found that the two-photon absorption coefficient (β) for a sample with 10 minutes of annealing time is about 0.037 cm/GW. It is important to point it out that there is also a case where transmittance is larger on focus than away from focus, referred to as saturable absorption but, there was not evidence of this behavior for the ceramics and the values of irradiance used in this study.
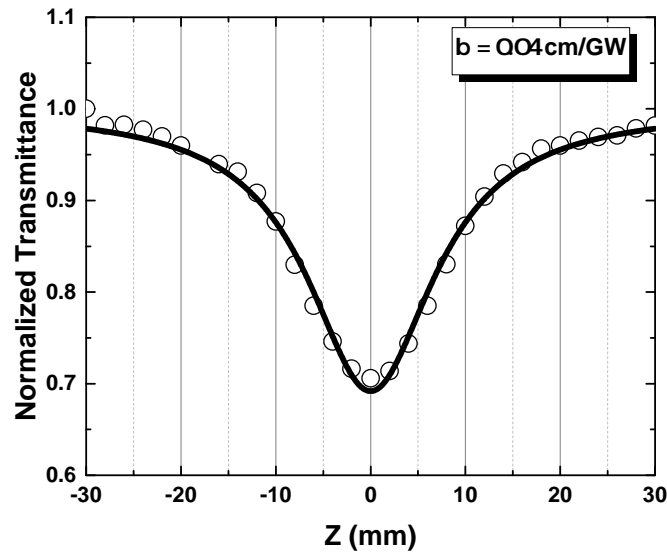
Fig. 4.9 Experimental results of open Z-scan for a sample with 10 min.of annealing time. Corresponding values of T(z) together with the fitting curve and the obtained best value of β.

On the other hand, the nonlinear refraction (NLR) of the YSZ ceramic was also estimated performing the closed Z-scan experiment. In this case, it is common that NLR coefficient (γ) of a material that exhibits TPA and NLR simultaneously would be calculated by extracting the effects of TPA from the closed Z-scan curve, according to the method described in [147]. The procedure basically consists in taking the ratio between the NLR curve and the TPA curve. This results in a purely refractive case curve from which γ can be extracted. Since the YSZ ceramic presents nonlinear absorption it was necessary to carry out this procedure for every measure of the NLR of the ceramics. Fig. 4.10 shows the closed-aperture Z-scan curve together with the fitting curve of Eq.(4.6) to the data and the obtained best value of γ for a ceramic with 10 minutes of annealing time. In this case γ was measured to be 3×10^{-15}cm^2/W. From the

curve it is possible to deduce that this material presents a positive NLR, which can be easily analyzed by just observing the shape of the curve, which presents a prefocal transmittance minimum (valley) followed by a postfocal maximum (peak).
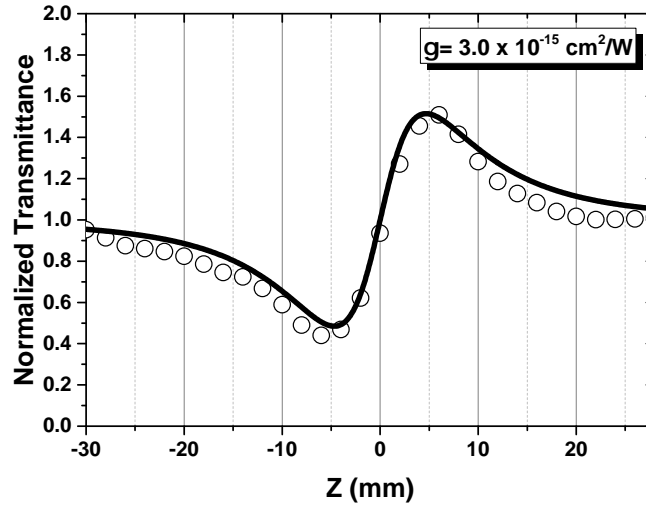
Fig. 4.10 Experimental results of closed Z-scan together with the fitting curve and the obtained best value of the NLR coefficient γ for a sample with 10 minutes of annealing time.

Since the beam used in these experiments approximates to a truncate Gaussian beam, the expressions used to fit the experimental results of the Z-scan experiments are an approximation. Therefore, this requires a statistical method to corroborate that the data are correct and give a more precise measurement. For this purpose, an additional equation for the normalized transmittance given by Eq.(4.7) was used.

$$T_{closed}(z) = 1 - A\frac{x}{(x^2+9)(x^2+1)}, \tag{4.7}$$

where z_0 and A are the parameters for the fitting. With $A = \frac{8\pi}{\lambda\sqrt{2}}\gamma L(1-S)^{0.25}I_0$. Thus, to obtain the value of the NLR a series of measurements obtaining A as function of the intensity I_0 are taken. In this way a value of A for each value of intensity is obtained, and the value of γ can be easily extracted from a linear fitting from:

$$A = mI_0, \tag{4.8}$$

Where the slope m corresponds with the NLR of the material with independence on the intensity. Fig. 4.13 shows experimental data for values of A as a function of the intensity. It is possible to see clear lineal dependence between the data which assures a precise measurement of the values for the NLR. From the linear fitting a slope of 5.39178×10^{-11}. By combining the definition of A previously mentioned and Eq.(4.8) a value of $3.2 \times 10^{-15} \mathrm{cm}^2/\mathrm{W}$ was obtained for the sample with 10 min of annealing time. This value is of the same order of magnitude and is in good agreement with the first value of γ previously mentioned of $3 \times 10^{-15} \mathrm{cm}^2/\mathrm{W}$. Hence, from this result, it can be concluded that there is a good estimation of the nonlinear coefficients of the YSZ ceramic.
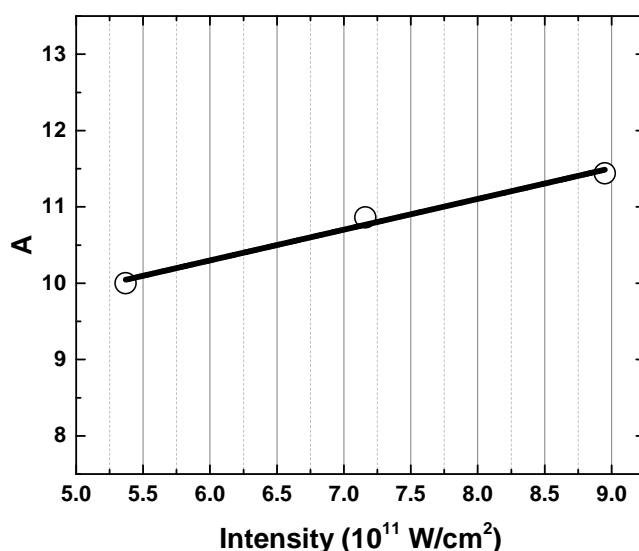
Fig. 4.11 Experimental results of closed Z-scan for the parameter A as a function of the intensity I_0.

Annealing time influence

Concerning to the influence of annealing time on the nonlinear optical properties of the ceramics, β and γ for a ceramic with 30 minutes of annealing time was also estimated. Table. 4.4 presents the results in samples with different annealing time (i.e. different linear optical properties). It was found that as the annealing time increases, there is a decrease in the nonlinearities. This could be mainly due to oxygen vacancy concentration (color centers); samples with lower annealing time presents a higher concentration of color centers which generally absorbed at UV wavelengths. Since femtosecond pulses around 800 nm are used, it is logic to assume that TPA

is occurring at UV wavelength. This, leads to a larger TPA for ceramics with lower annealing time. However, the value of the TPA coefficient can be easily controlled by annealing the ceramics in air at different times [136]. On the other hand, a reduction in the value of n_2 as the annealing time decreases was also found. The explanation for this behavior is not so obvious, but a possible reason could be that for samples with higher oxygen vacancies concentration, there are more external process as the thermo-optical process, that contributes to the value of the nonlinear refractive index.

Table 4.4 Values of non-linear absorption coefficient and non-linear refraction coefficient for ceramics with different annealing time together with their corresponding third-order optical susceptibility.

Ceramic	β(cm/GW)$\pm 8\%$	γ(cm^2/W)$\pm 13\%$	$\chi_R^{(3)}$(m^2/V^2)	$\chi_i^{(3)}$(m^2/V^2)
10 min.	0.04	3.0×10^{-15}	5.1×10^{-21}	4.3×10^{-22}
30 min.	0.02	0.2×10^{-15}	0.3×10^{-21}	2.2×10^{-22}

It must be pointed it out, that the values of β are relatively low (one order of magnitude lower) in comparison with other materials considered for optical waveguide devices in telecommunications [148, 149] which opens the possibility of considering this material for applications in this areas, where low values of the nonlinear absorption are desirable. In contrast, the values of γ presented by the YSZ ceramics are in the same range of a great variety of glasses and crystals.

Tab.4.4 also presents the calculated components of the third order optical susceptibility ($\chi^{(3)} = \chi_R^{(3)} + i\chi_i^{(3)}$), where the real and imaginary part are related to γ and β respectively. The components were calculated according to the following expressions given in SI units [140]:

$$\begin{aligned}
\chi_R^{(3)} &= (4/3)n_0^2\varepsilon_0 c\gamma, \\
\chi_i^{(3)} &= (n_0^2\varepsilon_0 c\lambda/3\pi)\beta,
\end{aligned} \tag{4.9}$$

where n_0, ε_0, and λ are the linear refractive index of the material, the electric permittivity of free space (8.85×10^{-12}F/m), and the wavelength respectively. Since the ceramics using in this study present linear absorption, alternative equations for absorbing media proposed in [150] were also used in order to correctly estimate the values of $\chi_R^{(3)}$ and $\chi_i^{(3)}$. It was found that in this case, the calculated values of the nonlinear optical susceptibility do not differ from the calculated using the traditional expressions given by Eq.(4.9).

Finally, the fact that used samples that possesses linear absorption indicates that a significant thermal contribution to the nonlinearity could be present. In order to estimate this contribution
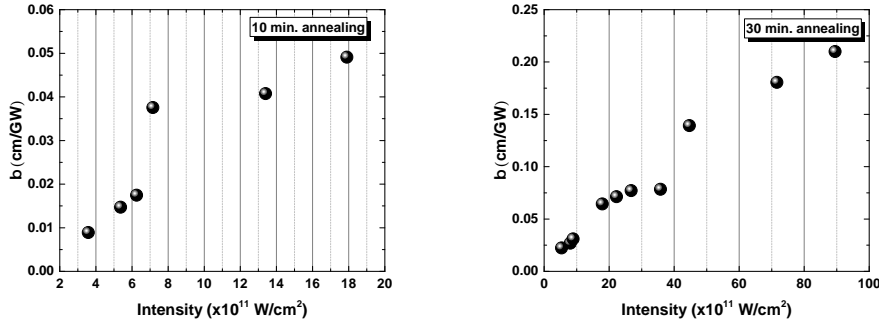
Fig. 4.12 Nonlinear absorption as a function of the peak intensity for ceramics with different annealing time.

the thermal contribution to the nonlinear index of refraction in terms of the thermo optic coefficient (dn/dT) was calculated through the relation [151]

$$\gamma^{therm} = \frac{dn}{dT}\frac{\alpha_0 \tau_p}{\rho c_v},\tag{4.10}$$

where, α_0 is the linear absorption coefficient, τ_p is the pulse duration, ρ is the density, and c_v is the specific heat. Calculation of the thermal contribution for a ceramic with 10 min annealing results in $\gamma^{therm} \approx 7 \times 10^{-18} \mathrm{cm}^2/\mathrm{W}$, were $\alpha_0 = 21.2 \mathrm{\ cm}^{-1}$, τ_p=120 fs, and values of $dn/dT = 7.2 \times 10^{-6} \mathrm{\ K}^{-1}$ and $\rho c_v = 2.59 \mathrm{\ J/Kcm}^3$ for cubic YSZ [152] were used. This is three orders of magnitude lower than the obtained value of γ, and thus is not significant in this case.

Additionally, a study to investigate the dependence of the nonlinear absorption with the intensity was carried out. For this purpose, a series of measurements of β for different values of intensity were done. The results of these measurements are shown in Fig. 4.12. From this figure, it is possible to see a linear dependence of the nonlinear absorption with the peak intensity even for intensities as high as $10^{12} \mathrm{W/cm}^2$.

To gain insight about this behavior an analysis of the dependence of $q_0(0)$ on I_0 was carried out in order to corroborate if more than two photons absorption was involved in the process. For this purpose a quadratic function as well as a third order function were fitting to the data. As an example Fig. **??** shows a curve of $q_0(0)$ versus I_0 for a 30 min annealing time sample. The best fitting was found for a quadratic function which is clearly indicative that in this case the two photon absorption is the dominant mechanism involve in the process. Additionally, data of $T(0)$ as a function of $I(0)$ was plotted in order to obtain a value of β independent on the intensity. Fig. **??** shows the experimental data together with the best fit of $T(0)$ for a sample

with an annealing time of 30 minutes. In this case a value of $\beta = 0.04 \pm 12\% cm/GW$ was found. This value is in the same order of magnitude and is consistent with the values presented in Table. 4.4.
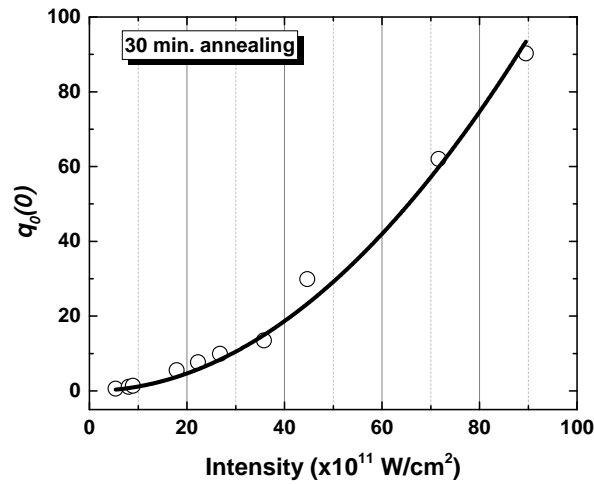
Fig. 4.13 Experimental data of $q_0(0)$ versus I_0 for a sample with 30 min. of annealig time together with the best fit of a quadratic function
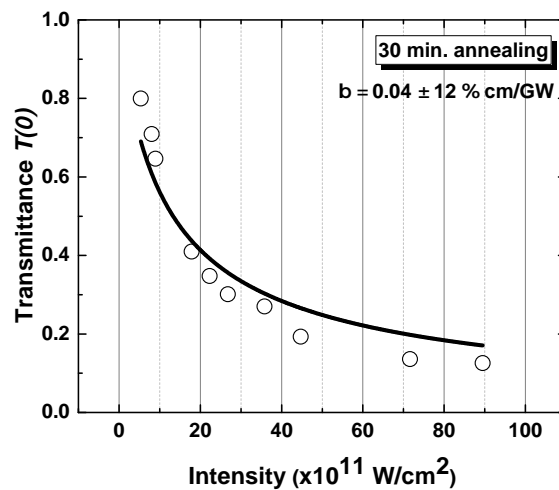
Fig. 4.14 Experimental data of $T(0)$ versus I_0 for a sample with 30 min. of annealig time together with the best fit of $T(0)$.

4.3.6   Conclusion

In conclusion, the nonlinear optical properties of YSZ ceramic have been estimated. An inverse dependence between the oxygen vacancy concentration in the ceramics and the nonlinear optical coefficient was found. Oxygen vacancies constitutes absorption centers, therefore by annealing ceramics in air, it is possible to control the value of the nonlinear optical properties of the ceramics. It has been also estimated the components of the complex third-order optical susceptibility. Taking into account the nonlinear properties of the YSZ ceramics, this could be considered as a material for optical communications.

4.4 Ultrafast laser inscribed waveguides in YSZ ceramic

4.4.1 Motivation

In recent years transparent ceramics have attracted significant attention for optical applications such as laser host materials, solid state lighting and light manipulation. Due to their great thermal and chemical properties and relatively efficient fabrication compared to single crystals, transparent ceramics are materials of great interest for optical applications. The fabrication of optical waveguides in these kind of materials has prompted a great variety of investigations and successful demonstrations of inscribed waveguides in different kind of ceramics. In this section, a study of femtosecond inscribed waveguides in YSZ ceramic is presented as well as their characterization.

4.4.2 Experiments

Waveguide fabrication

For this study a polycrystalline YSZ ceramic sample made from nano-sized (50 nm crystals) zirconia stabilized with 8 mol.% yttria (8YSZ)was used. The sample was cut in the form of a thin slab and all its faces were polished up to optical quality. For the fabrication process of the waveguides, the laser system mentioned in section 3.2 which emits 120-fs pulses with central wavelength of 795 nm operating at 1 kHz repetition rate was used. The laser beam was focused 150 μm below the sample surface using a 20$\times$ microscope objective with a numerical aperture (NA) of 0.4 and a focal distance of 10 mm. The sample was translated perpendicularly to the laser beam with constant speeds within the range from 15 to 50 μm/s, and the pulse energy varied between 6.4 and 96 μJ. The laser polarization was kept perpendicular to the scanning direction. The experiments consisted in the fabrication of double scan waveguides through type II modification. For this purpose parallel tracks separated by 15 and 20 μm were inscribed to form 2.2 mm long waveguides.

Characterization of the inscribed waveguides

In this case, the ability of the inscribed structures to behave as optical waveguides was investigated by coupling a He-Ne laser (633 nm) into the waveguides through a single mode optical fiber. Loss characterization of the waveguides was carried out according to the method described in section 3.5.2. The intensity distribution of the supported modes of the waveguides were recorded by imaging the backside of the sample through a 40$\times$ microscope objective onto a CCD camera. The transmittance measurements of the waveguides were conducted by

replacing the CCD camera by a calibrated photodiode. In addition, an iris was placed in front of the detector to suppress light transmitted through the bulk outside of the waveguide.

4.4.3   Results and discussion

Fig. 4.15 shows an optical micrograph of how the input face of the written structures in the YSZ ceramic looks like. The input face of each inscribed structure is composed of two parallel damaged tracks separated either by 15 or 20 μm, whose dimensions vary depending on the laser fabrication parameters. It was found that waveguides fabricated at higher energy present a better optical confinement in comparison to those obtained at low energies. It was also found that the structures written at lower scan speeds also present a better waveguiding. These features could be mainly due to a larger induced stress generated by the fact that when using higher per pulse energies (i. e. higher per pulse peak irradiances), more powerful pressure fronts and shock waves that compact the material are generated. On the other hand, by using lower writing speeds, a larger per unit area number of pulses strike the sample, and hence the average of deposited energy is higher in such a case than the one at faster scan speeds.
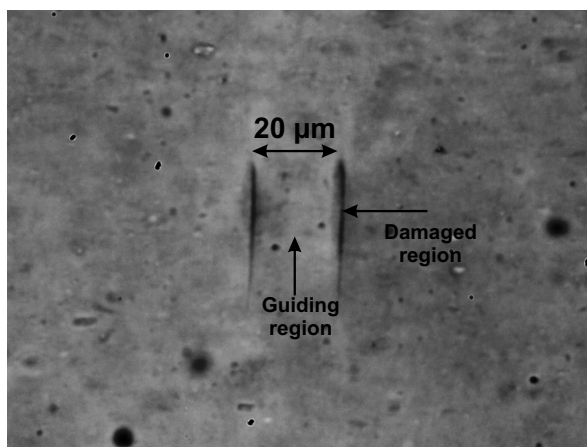
Fig. 4.15 Optical micrograph of the input face of a double-line waveguide fabricated in the YSZ ceramic at 96 μJ/pulse and scanning speed of 15 μm/s.

Fig. 4.16 (a) and (b) show an image of the near-field modes for track separations of 20 and 15 μm, respectively. We found that only structures fabricated with a separation distance of 15 μm between tracks present a single-mode behavior, as it is shown in Fig. 4.16 (b). An interesting feature that must be noticed is that light confinement is not only possible by the channel waveguide formed between the damaged tracks, but remarkably light confinement is also possible in the close proximity of a single track, i. e., on the top corner of the waveguide as it is demonstrated in Fig. 4.16 (c). We can clearly see in Fig. 4.16 (c) how there is a propagating

single mode on top of the damage track. This waveguiding feature has been reported previously for waveguides written in different crystals [153–155]. In those previous studies this effect has been attributed to the laser induced strain distribution around the focal volume, which creates material compaction, giving place to the refractive index change that forms the waveguide.

It is worth noticing that the waveguide structure formed outside of the channel waveguide exhibits distinct features like single-mode propagation, it supports a smaller dimension's mode, which in fact is much more symmetrical in comparison to the elongated channel waveguide modes. We found, that the light transmittance through this structure is lower than the one obtained for the channel waveguides. Fig. 4.16 (d) shows a top view optical micrograph during the coupling of light into the channel waveguide written at 96 μJ/pulse and a constant speed of 50 μm/s. As it can be seen, there is a good light confinement in the waveguide. However, the waveguide presents a strong attenuation along the propagation axis. This is mainly due to the optical features of the YSZ sample, which are determined by color centers (material defects), and hence by its linear optical absorption coefficient (20 cm^{-1} at 633 nm) [136].
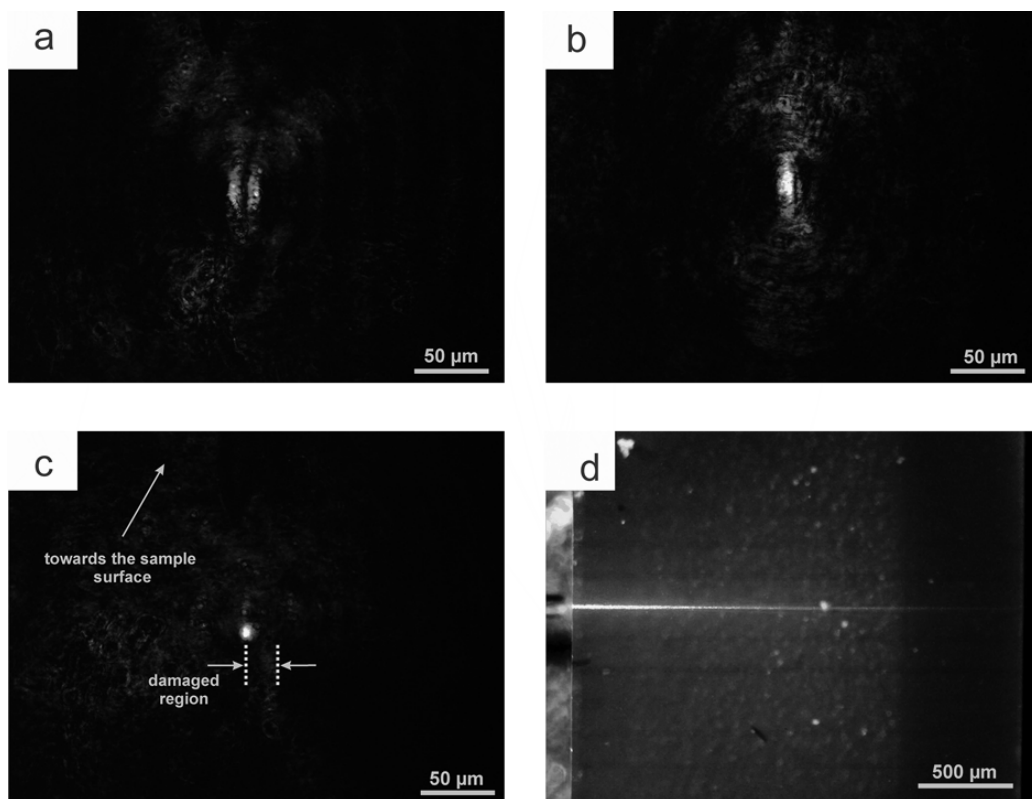
Fig. 4.16 CCD image of the transverse light intensity distribution at the end face of (a) 20 and (b) 15 μm width double scan waveguide and (c) single track structure. (d) Top view optical micrograph during light coupling into the channel waveguide.

Waveguides properties

For the loss characterization of the waveguides, the method described in section 3.5.2 was used. An average value for coupling losses of $\approx$80% was obtained for all the waveguides. Considering the Fresnel reflections of 5% at each output face of the waveguides, the propagation loss in the waveguides were found to be about 50 dB/cm at 633 nm. On the other hand, it was found that the total losses for the wave-guiding present outside the two parallel tracks, written at 96 μJ per pulse energy, were about 74 dB/cm. This indicates that the waveguide structures are more efficient than the single track waveguide structures.

The high losses in the waveguides are explained by material defects such as color centers (linear optical absorption). It was previously shown that color centers related to oxygen vacancies are produced during the YSZ fabrication process due to the reducing nature of the current activated pressure assisted densification process (CAPAD) [136]. As shown by Alaniz et al. [136] the vacancy concentration (and thus the resulting optical absorption coefficient) can be tuned by annealing of the YSZ samples in air at 750°C. The color center concentration (i. e., the optical absorption) decreases as the annealing time increases. Therefore, samples with long enough annealing time treatment can be used in order to improve the optical quality (transmittance) of the waveguides; work in this direction is underway. It is worth mentioning here that the transmittance of the YSZ ceramic increases for longer than visible wavelengths [133, 136]. Therefore, longer wavelengths would minimize optical losses in these waveguides. This is particularly relevant for optical communications applications of the waveguides presented throughout this work. Another important observation in the this study is the fact that light confinement in the channel waveguides is possible for both TM and TE polarizations. Nevertheless, we found better light confinement for light polarized parallel to the inscribed damaged tracks, as it can be clearly seen in Fig. 4.17. Notice that a larger amount of light escapes from the waveguide for light polarized perpendicular to the inscribed damaged tracks.

In addition with the results and despite the losses find them in this structures, it is also important to emphasize the fact that this is a versatile material and has a great potential for optical devices integration. It has shown too that is possible to write waveguide-like structures in this material using unamplified femtosecond laser pulses of a few nJ; a new method in which waveguide-like structures are created by femtosecond laser irradiation which cause a decreasing of the oxygen vacancies concentration thereby increasing the refractive index has been proposed [75]. Therefore, this makes it possible to write optical waveguides in this material either through amplified and unamplified femtosecond laser pulses.
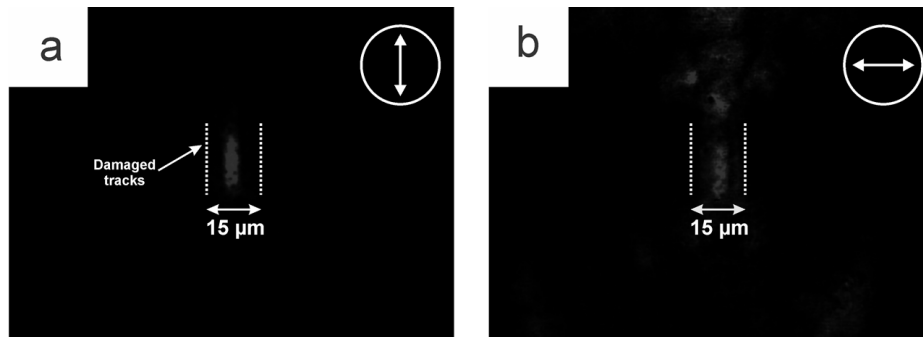
Fig. 4.17 CCD image of the near-field modes of the double scan waveguide: (a) linear polarization parallel to the inscribed damaged tracks, (b) linear polarization perpendicular to the inscribed damaged tracks.
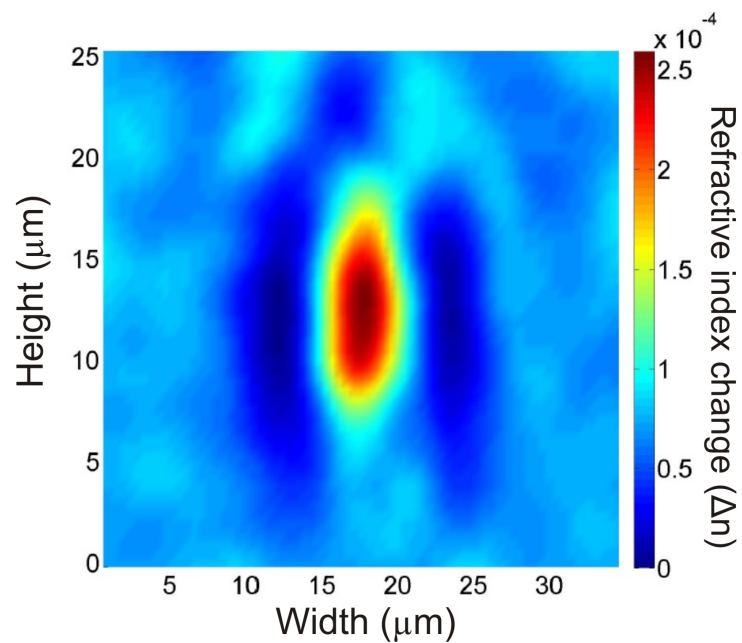
Fig. 4.18 Refractive index profile recovered using the inverse Helmholtz technique for a single mode channel waveguide written at 96 μJ/pulse, scan speed of 50 μm/s and a separation between tracks of 15 μm.

Refractive index contrast

The magnitude of the refractive index contrast (Δn) was estimated by experimentally measuring the numerical aperture of the waveguide, then assuming a step index profile, according with the method described in section 3.6. For a double line waveguide written at 96 μJ/pulse, scan speed of 50 μm/s and a measured N.A. of 0.058 a $\Delta n \approx 7.7 \times 10^{-4}$ was obtained. In order to corroborate this value the inverse Helmholtz technique was employed according to the method explained in section 3.6. Figure 6 shows the refractive index profile recovered using the inverse Helmholtz technique. It can be observed from Fig. 4.17 that there is good agreement with the calculated Δn obtained by measuring the channel waveguide numerical aperture experimentally, which is in the order of 10^{-4}. It can also be seen that there is a refractive index decrement right on the damaged tracks, surrounded by a small refractive index increment which could explain the waveguiding seen in the top vicinity of a single damaged track (Fig. 4.16 (c)). It is important to note that the minimum value in the scale of the refractive index change equals zero. This is due to the fact that the applied computing method makes the assumption that the refractive index of the bulk material (n_B) equals the effective index of the waveguide (n_{eff}) in order to determine (Δn). Therefore the absolute value of the refractive index decrement right on the damaged tracks cannot be correctly estimated.

Micro-Raman Analysis

Finally, In order to obtain information about the effects that ultrahigh irradiance femtosecond laser pulses have on the crystalline structure of the YSZ ceramic, micro-Raman measurements across the laser processed regions was carried out. Fig. 4.19 shows the Raman spectra obtained from a double line waveguide written at 96 μJ/pulse, scan speed of 50 μm/s and a separation between tracks of 15μm. Spectra from three distinct zones were taken in order to identify any laser-induced modifications to the crystalline structure of the YSZ ceramic. Measurements on the damaged tracks, on a spot far from the laser-irradiated region (bulk), and in between the damaged tracks, i. e. guiding zone (see Fig. 4.15) were taken. It can be clearly seen from the Raman spectra in Fig. 4.19 that the YSZ ceramic stands the laser interaction without any significant induced phase changes. Notice though, that the intensity of the spectra for the damaged track zone is lower in comparison to the intensity of the spectrum of the non-irradiated region. This effect has been studied before and is in general related to defects creation [29]. It is important to note here that this spectra intensity behavior is consistent for all the fabricated waveguides in the present study (6.4–96 μJ/pulse).
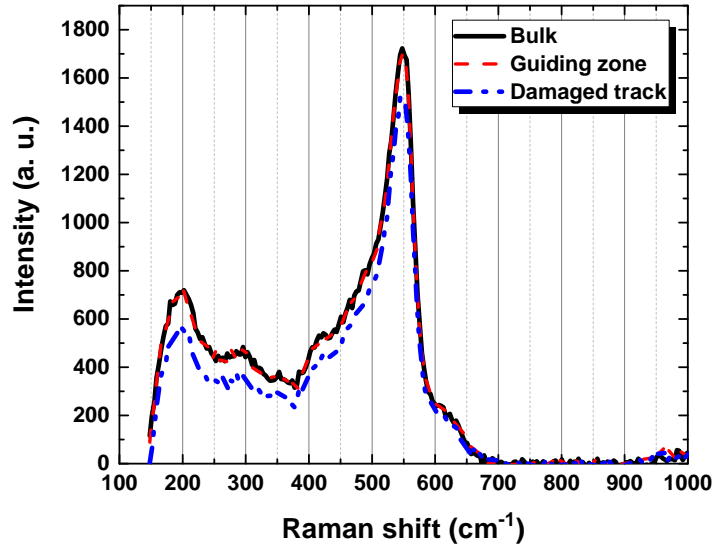
Fig. 4.19 Micro-Raman spectra of a channel waveguide in YSZ, written at 96 μJ/pulse, scan speed of 50 μm/s and a separation between tracks of 15 μm.

4.4.4   Conclusion

It has been demonstrated that it is possible to fabricate double scan waveguides in the nanostructured YSZ ceramic, by using amplified femtosecond laser pulses. Interestingly, it was found that light confinement occurs not only within the double line structure, but also in the close proximity to a single damaged track outside the double scan structure. There is a spatial mode dependence on the channel waveguide width; in the studied cases single mode propagation was observed only for the 15 μm width waveguides. The propagation loss of the fabricated waveguides are constant for the whole range of irradiation conditions used for this study (6.4–96 μJ/pulse and 15-50 μm/s), such losses were determined to be about 5 dB/mm at 633 nm. A positive refractive index change ($\Delta n \approx 7.7 \times 10^{-4}$) was laser-induced at the core of the waveguide structures. Micro-Raman analysis of the channel waveguide structures and its surroundings revealed that the crystalline nature and phase of the YSZ samples are not compromised by the ultrahigh peak irradiance laser-interaction. This could be expected since YSZ possesses a remarkably stable crystalline structure.

Chapter 5

New schemes for ultrafast laser inscribed waveguides

5.1 Ultrafast laser inscribed, stress-induced waveguides. Double beam technique

5.1.1 Introduction and motivation

As mentioned previously, the material modifications that can be induced by laser irradiation are classified in Type I or Type II, depending on whether the irradiation conditions are below or above the optical damage threshold, respectively [79]. In the case of crystals [61], the most usual technique for producing waveguides is the so-called *double-line* approach, which is based on Type II modifications [156]. In this approach, two parallel laser-damage lines are created close to each other, resulting in a refractive index increase in the area between both lines, due to the stress-field (lattice compression) induced by the ultrashort pulse irradiation [88]. This technique has been applied to a large number of crystals for the fabrication of different active photonic devices, for instance waveguide lasers [29, 34, 90, 89] or wavelength converters [28, 96]. Nonetheless, in the application of this technique the mechanical waves created in the focal region produced many times an asymmetrical stress field that tends to deform the modes of the waveguides due to incubation effects related to the existence of pre-damaged states.

In this section a new approach consisting in the fabrication of stress-induced optical waveguides produced by the simultaneous irradiation with two femtosecond laser beams generated with an interferometer is proposed. This technique is proposed in order to generate more symmetric stress patterns (i.e. more symmetric modes) and the reduction of the propagation

losses which are explained in terms of the fact that simultaneous inscription allows for a drastic reduction in the magnitude of incubation effects.

5.1.2 Experiments

Waveguide fabrication

For the fabrication of the waveguides the experimental setup explained in section 3.2 was used. In this case, an interferometer with a variable delay line was arranged to produce two collinear beams with nearly equalized mean power (see Fig. 5.1). The optical paths of both beams were adjusted in order to get the best temporal overlap (delay 0 between pulses of the two beams) by optimizing the contrast of the produced interference patterns. Both beams were focused through a $20\times$ microscope objective at $100\,\mu$m beneath the sample surface, which was placed on a computer-controlled motorized three-axis stage. The use of an interferometer allows a fine and continuous control on the focal separation. Additionally, the interferometer allows the introduction of an arbitrary delay between both pulses if required.
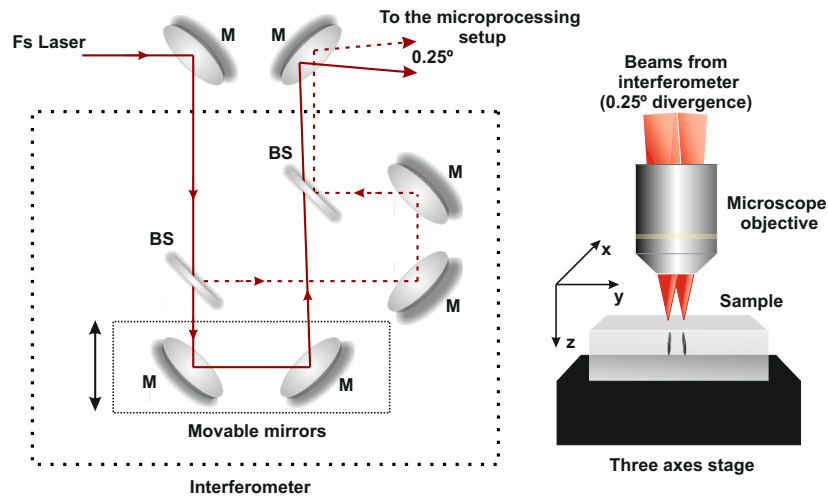
Fig. 5.1 Schematic of the simultaneous DB irradiation experiments. (a) Interferometer that produces the two beams (M: mirrors, BS: 50-50 beam-splitter); (b) The two beams focused through the microscope objective inside the crystal. (The divergence between the two beams has been exaggerated in the pictures for the sake of clarity).

Two sets of experiments were carried out: the one, with simultaneous double beam (DB) irradiation, and the other with single beam (SB) irradiation (standard fabrication technique). In the first one (DB), both beams were slightly misaligned (symmetrically, with less than 0.25° of divergence) in the interferometer in order to get two separated focal spots after the microscope objective, with the distance required between them in each experiment (15 μm, 20 μm or 30

μm). The experiments were done in Nd:YAG that is one of the most widely used gain media for solid-state lasers due to its outstanding fluorescence, thermal and mechanical properties. Nd:YAG has been the subject of a number of previous studies on optical waveguide inscription with femtosecond lasers [90, 157] and it is very well characterized. The sample was cut to dimension 100 mm^3 and polished down to optical quality. The beams were focused inside the crystal through one of the largest faces at a depth of 150 μm. The sample was then scanned once at constant velocity resulting in two parallel damage tracks simultaneously written in the crystal in a single step. In the second set of experiments (SB), one of the beams was blocked in the interferometer, and then, two parallel scans of the sample were done with the other beam in order to produce two parallel damage tracks at the same separation than in the corresponding DB experiment. In both DB as SB experiments, different scanning velocities (25-100 μm/s) and pulse energies (0.2-0.9 μJ) were used in order to explore the effect of the laser irradiation parameters on the waveguide performances. Fig. 5.2 shows an optical micrograph of waveguides fabricated by double and single beam irradiation. As it can be clearly seen there is a slight difference between the size of the tracks for single beam irradiation. The details of this results will be discussed later.
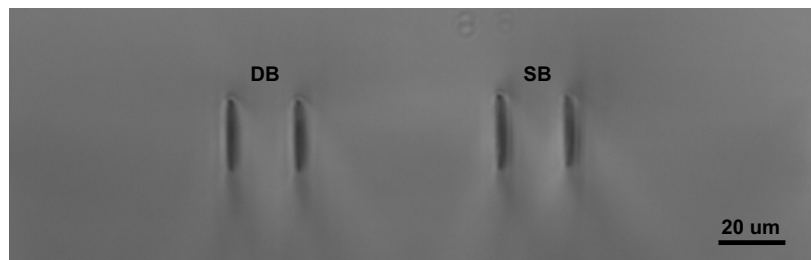
Fig. 5.2 Optical micrograph of waveguides fabricated by double (lefft) and single (right) beam irradiation using a pulse energy of 0.9 μJ and a scanning velocitie of 25 μm/s.

Optical waveguide characterization

The modal profiles of the fabricated waveguides were investigated with an end-fire coupling setup at 633 nm. Light at input face of the waveguides was polarized parallel to the inscribed tracks in order to minimize transmission losses (see Fig. 5.1). Waveguide propagation losses were evaluated by measuring the output and input powers, taking into account losses at the input and output microscope lenses, Fresnel reflections at the crystal interfaces, and the modal overlap between the injected light and the modal profile as it is mentioned in section 3.5.2. The refractive index change (n) induced by the stress field in the waveguide core was estimated by

measuring the numerical aperture of the guided mode in the far-field and assuming in a rough estimation a step-index profile, according to the method mentioned in section 3.6.

Micro-luminescence measurements

Micro-luminescence imaging of the stress-induced waveguides were obtained in a home-made confocal fluorescence microscope. A single-mode fiber coupled laser diode (808 nm) was used as an excitation source. The beam laser was focused into the sample by using a single microscope objective with a numerical aperture of 0.85, leading to an excitation laser spot radius of 0.5 μm approximately. 808 nm radiation excites Nd^{3+} ions from their ground state ($^4I_{9/2}$) up to their $^4F_{5/2}$ excited state from which non radiative de-excitations down to the $^4F_{3/2}$ metastable state take place. The subsequent $^4F_{3/2} \rightarrow {}^4I_{9/2}$ emission is collected by the same microscope objective and, after passing through different spectral and spatial filters is spectrally analyzed by a high-resolution spectrometer. In this work special attention to the spatial variation of the intensity was paid, spectral position and bandwidth of the narrow emission lines centered at around 940 nm as they have been demonstrated in the past to be excellent indicators of the local damage, stress and disorder in the Nd:YAG network, respectively [88].]. For the acquisition of fluorescence and structural images of the waveguides, the Nd:YAG sample was scanned in three dimensions by placing it on an XYZ piezo-stage while keeping the 808 nm excitation spot fixed. The spatial variation of peak intensity, position and width (used for damage, stress and disorder imaging) were obtained by using the LabSpec software. Graphical representation of data was performed by using the WSXM software [158].

5.1.3   Results and discussion

Firstly, the modal profiles of the fabricated waveguides were analyzed. Guidance was observed for the three track separations but the fabrication parameters (pulse energy/scanning velocity) that minimized the measured losses were different (see Fig. 2): 0.44 μJ, 25μm/s for 15 μm (WG1) and 20 μm (WG2) track separation, and 0.90 μJ, 100μm/s for 30 μm track (WG3) separation. As it can be seen in the figure, the modal profiles for DB waveguides were highly symmetrical and single mode in all the cases. However, SB waveguides show more irregular profiles, effect that is particularly noticeable for small track separations for which asymmetric multimode profiles are obtained.

Concerning the propagation losses, in all the measurements DB waveguides showed superior performance with a loss reduction between 5% and 30% with respect to SB waveguides. In particular, propagation loss as low as 0.15 ± 0.1 dB/cm was measured for the DB-WG2 and 0.15 ± 0.1 dB/cm for SB-WG2. This value obtained for DB waveguides improves previously

reported values for Nd:YAG stress-induced waveguides [90]. In contrast, the refractive index increase estimated from Eq. 1 was larger for the SB waveguide $\approx 8 \times 10^{-4}$ (SB waveguide $\approx 4 \times 10^{-4}$). This behavior is surprising, as one would expect a larger refractive increase induced in the material when two mechanical waves (compressive) were produced simultaneously from both damage tracks to the center of the waveguide. Nevertheless this effect could be tentatively explained taking into account that the refractive index change estimated here should be considered as an average value in the whole structure. In the case of SB irradiation, the second damage track is produced on a pre-modified volume of the YAG network so a larger modification (refractive index change) would be expected, this leading to a larger overall refractive index change. The effect of the incident laser polarization on the supported waveguide modes was also investigated. In all the cases, the guidance is better for polarization parallel to the damage tracks and poor for the perpendicular one, although a slightly more isotropic behavior is found for DB waveguides (see as example Fig. 5.3g).
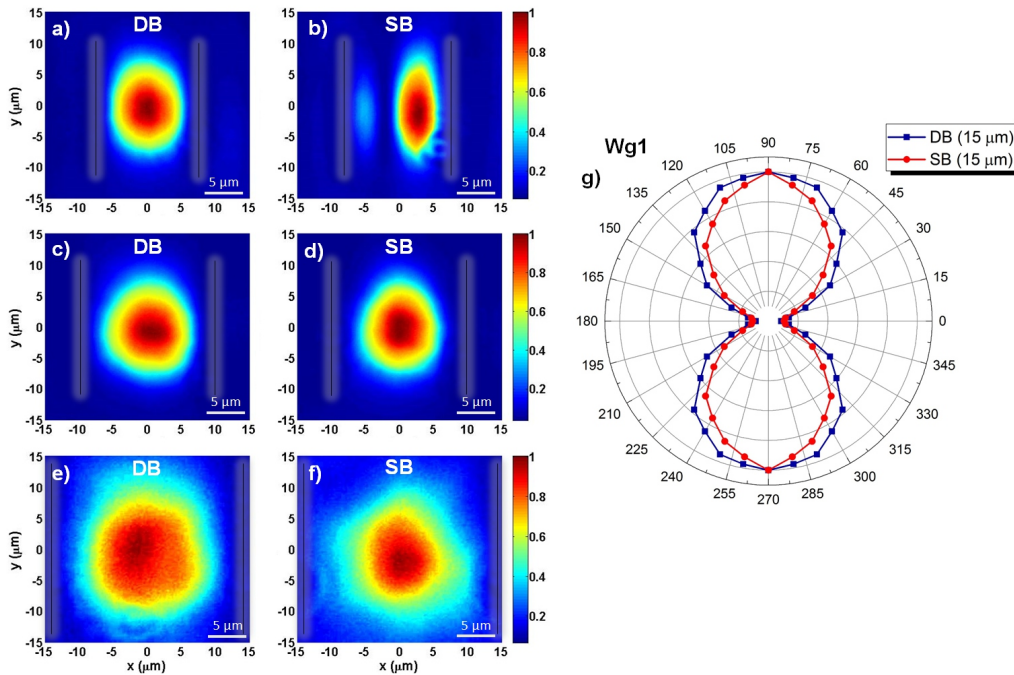
Fig. 5.3 (a-f) Modal profiles of the waveguides at 633 nm and polarization parallel to the damage tracks (approximate positions shown by vertical lines). (a-b) WG1 (15 ?m track separation, 0.44 μJ pulse energy and 25 μm/s scanning velocity) for DB and SB fabrication, (c-d) WG2 (20 μm track separation and same irradiation conditions), and (e-f) WG3 (30 μm track separation, 0.90 μJ pulse energy and 100 μm/s scanning velocity). g) Polarization dependence of the transmitted power (normalized) for WG1 (0 corresponds to polarization perpendicular to damage tracks).

To gain insight in the mechanisms underlying the different behaviors observed, luminescence maps were taken for the different waveguides. In Fig 5.4 we show the peak position (Top panel) and intensity (Bottom panel) maps corresponding to WG1 (15 μm track separation). As explained in detail in previous references (see [88]) these maps can be unequivocally correlated to the spatial distribution of residual stress and damage, respectively. Independently on the inscription method, the double filament structures are characterized by a localized damage at the filaments that is accompanied by a compressive stress at filaments and in their surroundings (such compressive stress is denoted by a redshift in the emission lines). This fact indicates that in both inscription procedures the mechanism leading to waveguide formation is the same: the refractive index increment created at filaments and between them due to compressive stress.
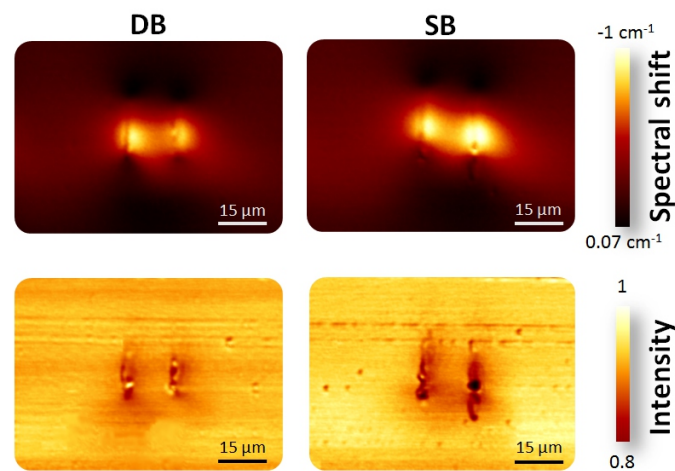
Fig. 5.4 Micro-luminescence maps of WG1 obtained by DB (left) and SB (right) inscription. Top panels show the spatial variation of the stress-induced spectral shift of Nd:YAG emission lines. These maps clearly reveal a larger symmetry of the stress-field pattern in the case of DB inscription. Bottom panels represent the spatial distribution of the Nd:YAG luminescence intensity that is related to the spatial variation of laser-induced damage in the Nd:YAG crystal lattice

However, clear differences can be appreciated: as it is expected, the simultaneous irradiation (DB) to produce both damage tracks leads to a more symmetrical stress field and, also, to a more similar damage distribution in both tracks of the waveguide (see Fig. 5.6). Such creation of highly symmetrical stress patterns leads, consequently, to a more symmetrical refractive index increase distribution in all the studied cases. In the standard double-scan approach (SB) the stress field is asymmetric due to the presence of the so-called incubation effect: the inscription of the first damage track leads to the appearance of a modified volume in the Nd:YAG that is not only restricted to the laser focal volume but that, indeed, extends several microns from it.

Therefore, the inscription of the second damage filament is not performed on an unperturbed Nd:YAG volume (as it was in the case of the first filament) but, on the contrary, it is performed on a pre-modified Nd:YAG lattice so that the resulting structural effects (stress, damage and disorder) are completely different [156]. This effect is particularly relevant for small track separations. This makes both inscription methods non-equivalent leading to the appearance of asymmetrical structural maps and, hence, to asymmetrical refractive index patterns. Thus, in such case, only certain irradiation conditions lead to symmetrical modal profiles (see Fig. 5.3d). The effect of the SB fabrication in two subsequent sample scans affects even to the different aspect ratio and vertical positions of the damage tracks, as it can be seen in the microscope images shown in a number of papers (see for instance [29, 156, 88, 34, 90, 89]). As an example Fig. 5.5 shows a comparison between a waveguide fabricated by double beam irradiation versus a waveguide fabricated with single beam irradiation reported in [116]. On the other hand, a more homogeneous stress distribution in the volume between the damage tracks is produced with DB irradiation, what means a more uniform refractive index increase in the waveguide region. This behavior could explain the greater extension observed in the modal profiles of DB waveguides. In such case, the reported estimations of the refractive index increase for both DB and SB waveguides would not lead to comparable values as they correspond to very different index profiles.
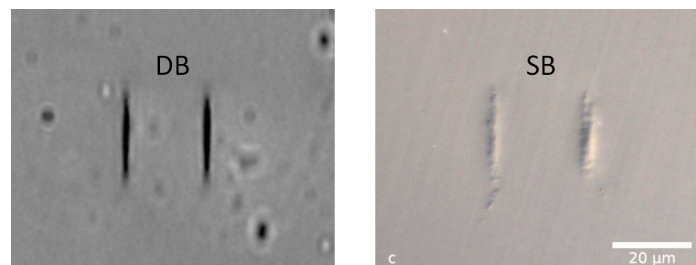
Fig. 5.5 Comparision between double and single beam irradiation [116] showing the different aspect ratio and vertical position of the damaged tracks.

5.1.4 Conclusion

In summary, an study of stress-induced waveguides fabricated in Nd:YAG by simultaneous double beam irradiation with femtosecond pulses has been presented. The setup is based on an interferometer that allows the perfect equalization of the energy of the two beams, the adjustment of delay 0 between them, and the fine control of the separation between focal spots. The waveguides fabricated in this approach are compared to those fabricated with the traditional double scan technique (SB), and the modal profiles and optical performances are
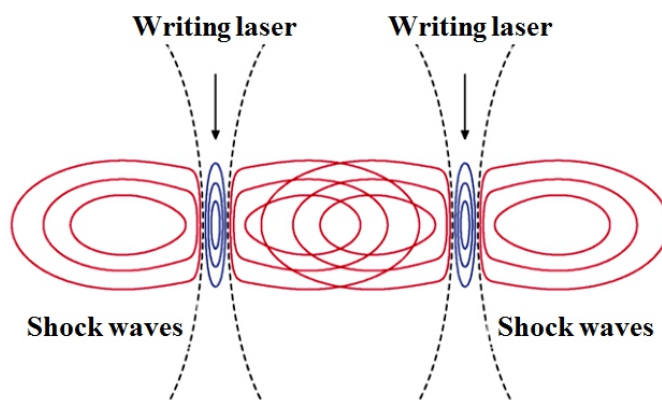
Fig. 5.6 Schematic diagram of the waveguide fabrication. The two parallel irradiation induces a symmetrical stress patterns which generate an index-increased regions that overlap in the middle surrounded by a refractive index decrement in the focal area. Picture taken from [87].

different in both cases. The stress field (derived from micro-luminescence maps) induced with simultaneous (DB) irradiation is symmetrical, leading to symmetrical, single-mode and larger modal profiles in all the studied irradiation conditions. Moreover, with DB irradiation a significant reduction of propagation losses was achieved. Measurements performed on the numerical aperture of the waveguides report that SB technique produces a larger refractive index increase in comparison to the DB. However, the different refractive-index profiles that are expected in both waveguide approaches make these estimations difficult to compare.

5.2   Depressed-cladding waveguides. 3D waveguide arrays: honeycomb waveguides

5.2.1   Introduction and motivation

In the last years, depressed-cladding waveguides [31] has become one of the most versatile structures that can be inscribed with Type II modification (see Chapter 2). These waveguides consist of a large number of parallel damage tracks that form a cladding with a certain geometry (with a decreased refractive index), and a central core whose refractive index remains almost unaffected by the femtosecond laser irradiation. Fig. 5.7 shows a typical depressed caldding waveguide fabricated in Nd:YAG crystal together with the schematic diagram of a cladding waveguide. There are a lot of works demonstrating such waveguides in a large number of crystals for different applications (i.e. waveguide lasers or frequency converters) [159–163]. In this section an study of the fabrication of waveguide arrays based on depressed-cladding structures produced by direct femtosecond laser inscription in a sample of Nd:YAG crystal is presented. The results show a very good performance of the fabricated structures and suggest a promising potential use in photonic applications such as photonic lanterns.
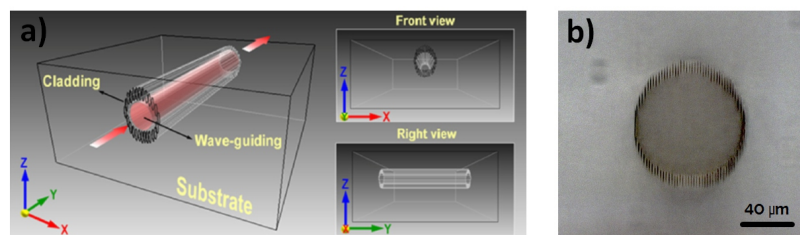
Fig. 5.7 a) Schematic diagram of a depressed cladding waveguide [104]. b) Optical micrograph of the cross-section of a typical circular cladding waveguide fabricated in a Nd:YAG crystal.

5.2.2   Experiments

Waveguide fabrication

For the waveguide inscription in the crystal, the femtosecond laser system mentioned in section 3.2 was used. In this case, the beam was focused through a $50\times$ microscope objective (N.A. = 0.6). The sample, a 1 cm long Nd:YAG crystal, was placed in a 3-axes motorized stage with a resolution of 0.1 μm. The threshold energy to produce a damage track at a depth of 200 μm from the surface was found to be 0.19 μJ under our experimental conditions. To inscribe the structures, we have used a pulse energy of 0.28 μJ, large enough to ensure the

successful inscription of damage tracks at all the required depths of the sample (between 150 and 330 μm), but keeping the damage of the material in a reasonable level such that cracks are not produced. The sample was scanned with the stage at a constant velocity of 500 μm/s. The arrays consisted of seven adjacent hexagonal waveguides, each one formed by 30 parallel tracks with a lateral separation of 2 μm. It is important to point it out that this small separation was chosen after several proves in order to minimize the light leakage through the cladding boundaries. These parameters produced a single hexagonal structure with a diameter of about 22 μm. With the aim of demonstrating their ability to be used as photonic lanterns, the design is as follows. The central waveguide is straight from the input to the output faces, and the adjacent 6 waveguides are composed by three parts: a 2-mm straight part (all the waveguides parallel to the central one), a 6 mm straight segment that separates each waveguide radially from the center, and a final 2 mm straight part again in the same direction as the initial part as it is shown in Fig. 5.8. For this study, three arrays were inscribed with different final separations between the waveguides: WA0 with no separation between waveguides (straight array), WA1 with a separation of d=20 μm, and WA2 with a separation of d=40 μm.
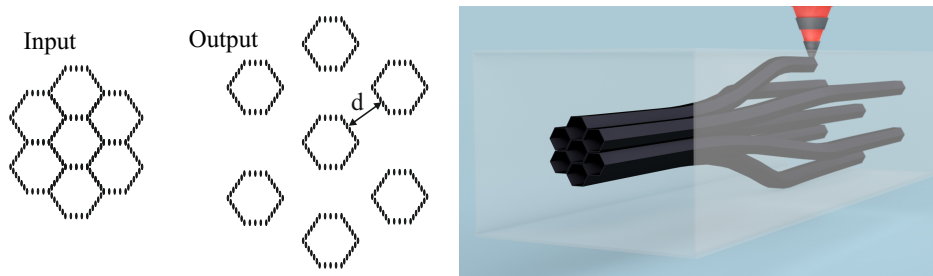
Fig. 5.8 Schematic diagram of the fabrication of hexagonal waveguide arrays based on depressed-cladding structures produced by femtosecond laser direct inscription.

Optical Waveguide Characterization

As before, the ability of the fs-laser written structures to behave as an optical waveguide was investigated with an end-fire coupling setup at 633 nm, at 800 nm and with white light from a phosphor-based light emitting diode (LED), focused at the input face of the crystal through a $10\times$ microscope objective and the near-field modal profiles were recorded by imaging the output face of the waveguides through a $20\times$ microscope objective onto a CCD camera (see Fig. fig:endfire). The transmittance measurements were conducted using a calibrated photodiode. In this case, an iris was placed in front of the detector in order to suppress light transmitted through the bulk outside of the waveguide. The size of the iris was fixed by imaging the output face of the waveguides on the CCD and matching the diameter of the iris to that of every

single hexagonal structure. Propagation losses in all the inscribed waveguides was estimated following the procedure described in section 3.5.4. Polarization dependence of the waveguides was carried out employing half-wave plates to control the polarization of incident laser beam. The magnitude of the refractive index contrast (Δn) between damage tracks and waveguide core was estimated by experimentally measuring the numerical aperture of a single hexagonal waveguide as it is explained in section 3.6.

Micro-Luminescence Measurements

Microluminescence maps of the structures were obtained using the same home-made confocal fluorescence microscope described in section 5.1.2 and by following such procedure.

5.2.3   Results and discussion

Firstly, in order to investigate the wave-guiding properties of the written structures, coupling of white light was performed. Fig. 5.9 shows an optical micrograph of the arrays with different separations between central and adjacent waveguides. As it can be clearly seen, the waveguides present a good confinement of incoherent white light. Furthermore, it is possible to observe that there is no damage of the material in the vicinity of the tracks, even in the zone where the waveguides overlap (in the case of WA0) which assures a good optical confinement and minimizes losses. The modal profiles are homogeneous, showing a nearly flat-top structure clearly confined by the damage tracks with negligible effect on the separation parameter *d*.
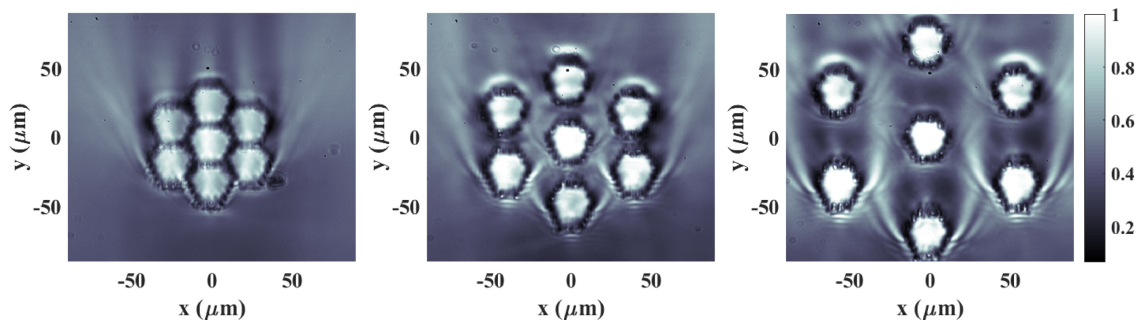
Fig. 5.9 Optical micrographs of the output face of the waveguide arrays showing confinement for white light for different separations between central and adjacent waveguides (from left to right, WA0, WA1 and WA2). The input faces of the three arrays are identical to the output face of WA0 (picture on the left).

Moreover, experiments to characterize the modal behavior of the waveguides at 633 nm were carried out. Fig. 4 shows the modal profiles for WA1 and WA2 arrays under TE polarization

which, in this case, represents polarization perpendicular to the damage tracks. Measurements of every single waveguide in order to observe differences between the central and adjacent waveguides were performed (it should be pointed out that we did not see evidence of coupling of light between adjacent waveguides when only one of them was being excited). For this purpose, images of the modes corresponding to the central and two external waveguides (top and top-right) were taken. It is possible to see in Fig. 5.10 that there are some differences between modes of adjacent waveguides in comparison with the central one. It can be seen that, at this wavelength, the behavior of the waveguides is multimode, although it is possible to excite only the lower mode in the central waveguide. The other waveguides (external) suffer the bending of the structure and this leads to the excitation of higher order modes. Moreover, it can be seen that in these cases light tends to concentrate near the cladding, maybe due to some residual stress induced during the waveguide fabrication as it will be discussed later. Concerning the isotropy of the waveguides (polarization dependence), it was found that waveguides support both TE and TM polarization, with a slight polarization dependence in all of them, being more pronounced in the case of the central ones which, as previously mentioned, could be due to a larger accumulation of mechanical stress induced during the inscription. However, the optical confinement is good in all the cases.

Concerning the propagation losses, measurements for 633 nm light are summarized in Table 5.1. As it can be seen, the obtained values fluctuate between 1.6 and 3.0 dB/cm for the different waveguides and polarizations.In this case, the scattered light imaging method described in section 3.5.3 was also used in some waveguides to do a double check of the results. From these measurements some conclusions can be extracted. Firstly, the magnitude of the waveguide losses is similar to those previously reported for other cladding structures in other crystals [159, 163, 164]. Concerning Nd:YAG, very different values have been reported in previous works, that range from 0.12 [165] to 2.0 dB/cm [166], depending on the waveguide diameter and on the coupling wavelength. Due to the small size of the waveguides described in our work (22 μm diameter) and the coupling wavelength used in our studies (633 nm) our results are in good agreement with [166] (30 μm diameter and same wavelength). Even larger core waveguides [167] may exhibit similar propagation losses values. Secondly, there is no significant difference in the behavior of TE and TM polarizations, as reported in previous works [168]. Finally, the bends of the waveguides have negligible effect in the losses within the accuracy of this measurements. It should be pointed out that the maximum divergence angle of the waveguides is smaller than 0.5° and this ensures a low level of losses.

Regarding the refractive index contrast induced in the damage tracks, a value of $\approx 4.2 \times 10^{-3}$ at 633 nm for one of the straight waveguides was obtained. It should be stressed that, in this case, this value represents a rough estimation due to the assumption of a step index profile
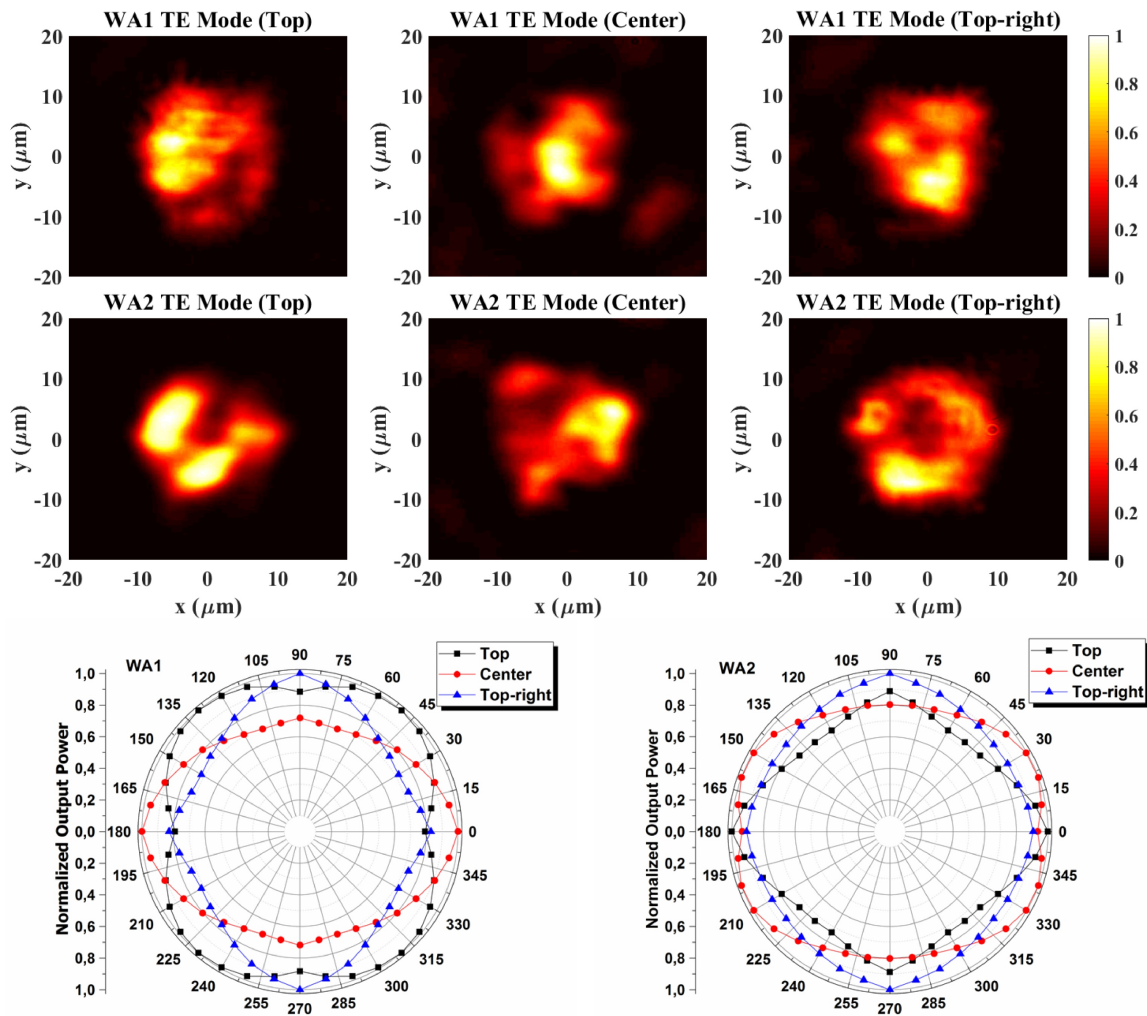
Fig. 5.10 Near field modes at 633 nm for WA1 and WA2 hexagonal waveguides together with their respective maps of polarization dependence, where 0° corresponds to TE polarization. The dots in the polar maps correspond to the measured power at the output face of the waveguide for every polarization angle, normalized to the maximum output value.

Table 5.1 Propagation loss for central and adjacent hexagonal cladding waveguides

Waveguide	α(dB/cm) ± 0.2	
	TE	TM
WA1		
Top	2.7	3.0
Center	3.2	2.6
Top-right	3.0	2.6
WA2		
Top	2.4	2.8
Center	2.7	2.2
Top-right	3.0	1.6

of the waveguides, but that magnitude is in fairly good agreement with previously reported values in Nd:YAG cladding waveguides when large numerical aperture focusing optics is used in the fabrication [166].

The modal characterization at 800 nm for WA2 is shown in Fig.5.11. As it can be seen from the images, the waveguide behavior at this wavelength is nearly single-mode, and distortions of the modal profiles are found only at the external waveguides, due to the effect of the bending. However, the confinement is very good and it was found that the guidance is independent of the incident polarization showing an isotropic behavior in all of the written structures.

Additionally, using the experimentally measured refractive index contrast (Δn), a reconstruction of the refractive index profile was carried out. Using this refractive index profile, modal behavior of a straight hexagonal waveguide was calculated by using the finite-difference time-domain method. In Fig. 5.12, the simulated TE mode at 800 nm for a straight hexagonal waveguide (neglecting the dependence with wavelength of Δn) together with the experimentally measured mode corresponding to the TE mode center of Fig. 5.11 are shown. By direct comparing Fig. 5.12 (a) and (b), it is possible to conclude a very good agreement between the simulated and the experimentally measured mode. This indicates that the values used for the reconstruction of the refractive index profile of the waveguide are reasonable.

In order to gain insight in the properties and behavior of the inscribed structures, luminescence maps were taken for the waveguides arrays. Fig. 5.13 shows the 2D spatial distribution of intensity, induced energy shift, and line width of the $^4F_{3/2} \rightarrow ^4I_{9/2}$ inter-Stark level emission line of Nd^{3+} ions around 940 nm for the input face of the arrays of WA2. In previous works, this emission line has been demonstrated to be an excellent indicative of sensitive changes in the material such as strain, volume changes, and disorder. The measurements are concentrated mainly in the central area of the array provided it is the most critical region due to the large
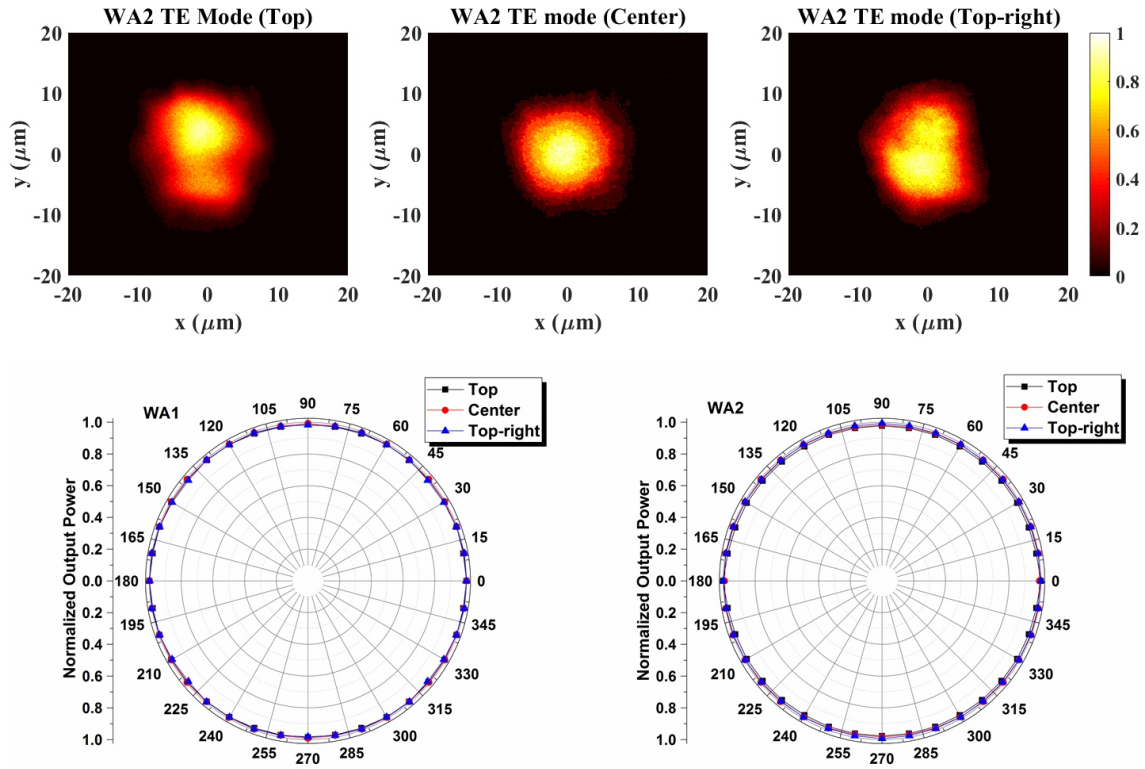
Fig. 5.11 Near field modes at 800 nm for WA2 hexagonal waveguides together with their respective polarization dependence maps. The dots in the polar maps correspond to the measured power at the output face of the waveguide for every polarization angle, normalized to the maximum output value.

accumulation of laser impacts of the adjacent waveguides. As it can be seen in Fig. 5.13 (a), there is a clear reduction in the luminescence intensity at the damage tracks, revealing the presence of lattice defects and imperfections in this region. Thanks to the large numerical aperture of the focusing optics employed in the fabrication, the waveguides cores remain almost unaffected. Concerning the spectral position of the emission (Fig. 5.13 (b)) it can be seen an energy redshift (compression) at the damage tracks and under them, and a slight blueshift (dilatation) above them. These effects are related to the stress fields created in the crystal lattice during the irradiation. It should be pointed out that the magnitude of the energy shifts is smaller than the values reported in literature for other cladding structures (see Ref. [168]), however, the extension of the affected areas is larger in these structures. The mean reason for this effect could be explained in terms of the large density of laser impacts that are used for the fabrication of the waveguide arrays (very small separation between tracks and overlap between claddings of the adjacent waveguides) that lead to a cumulative effect on the stress fields. This
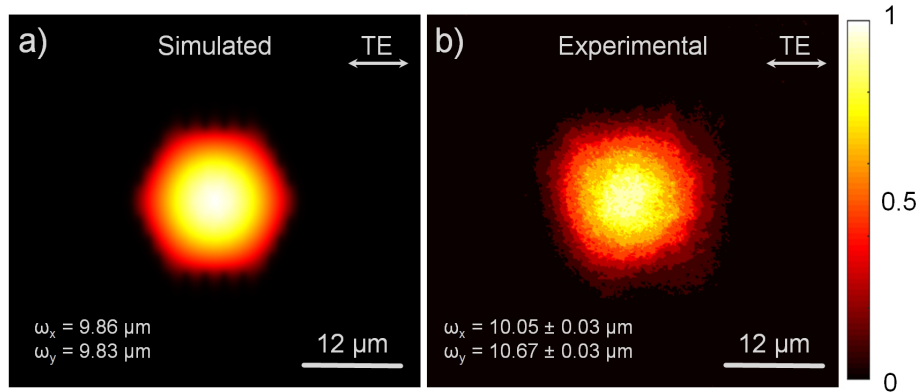
Fig. 5.12 (a) Calculated modal profile at 800 nm of a hexagonal straight waveguide and, b) measured mode profile at 800 nm for TE polarization. ω_x and ω_y correspond to the mode width sizes, measured at full width at half maximum (FWHM) intensity level, in the horizontal and vertical directions respectively

inhomogeneous distribution of compressed and dilated areas, could be responsible for the selective concentration of the modal profiles in certain areas of the cladding waveguides (see Fig. 5.10). Fig. 5.13 (c) shows the spectral broadening, that is higher in the zones were more disorder was induced during the fabrication, which correspond with the zones of quenched emission intensity in Fig. 5.13 (a).
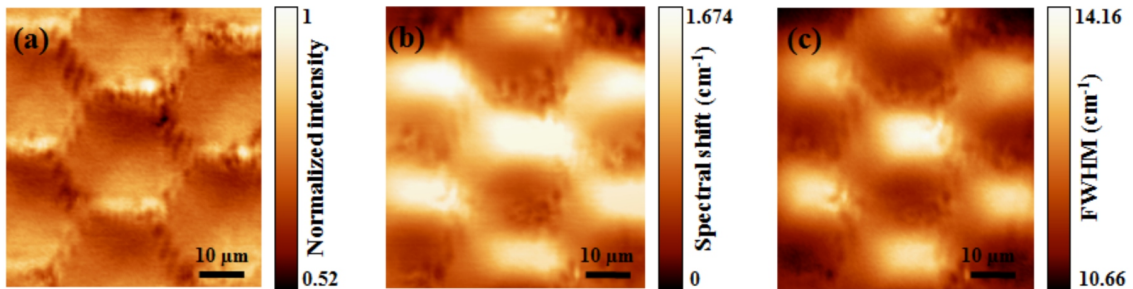
Fig. 5.13 Micro-luminescence maps of the input face of the waveguide arrays. The images represent the 2D spatial dependence of the intensity (a, peak position (b), and peak width (c) corresponding to the emission line of Nd^{3+} at 940 nm.

5.2.4   Conclusions

In conclusion, 3D arrays of hexagonal cladding waveguides have been successfully designed and fabricated by direct irradiation with femtosecond pulses. The arrays consisted of 7 waveguides

that separate radially along the propagation direction. For this study, a Nd:YAG crystal was chosen due to the possibility to microscopically analyze the material modifications induced during the irradiation with the femtosecond laser. The optical characterization of the structure reveals a complex multimodal propagation for the visible, and a nearly single-mode behavior for the NIR; the transmitted power through the waveguides shows a slightly dependence on the incidence laser beam polarization. The measured propagation losses of the waveguides in the arrays are in the range of 1.6-3.0 dB/cm, with no appreciable effect of the waveguide bends. Micro-luminescence maps have shown that the induced damage during the waveguides fabrication is concentrated at the tracks, while a residual stress/strain field affects larger areas of the structures. This results suggest that the reported waveguide arrays could be used for practical applications in photonics, such as photonic lanterns. Optimization of the modal behavior at the required operation wavelength can be achieved by conveniently adjusting the size of the cladding waveguides.

5.3   Photonic lattice-like structures

5.3.1   Introduction and motivation

Nowadays, femtosecond laser processing has become a widely applied method to fabricate waveguides and photonic devices in transparent materials. One of the objectives of the researchers in this field is to fabricate devices capable of manipulating the guided beam for the control of the spatial properties of the beam. Since the femtosecond laser processing allows the fabrication of waveguides at arbitrary depths inside a transparent material it is possible to explore a large number of designs for a specific application. In this section, the implementation of 3D waveguides based on photonic lattice-like structures, which are composed of a series of inscribed tracks that formed a hexagonal structure with a core of unmodified material, capable of efficient light guiding, is introduced. The introduction of axial track defects in the structures enables the possibility to use this kind of structures for efficient beam manipulation and in principle, to construct arbitrary devices for any purpose, see for instance [169, 170]. It is important to point it out that the structures presented here can be considered as depressed cladding waveguides, since the external damaged tracks act as an effective cladding by improving the light confinement. Furthermore it must be stressed that these waveguides are fabricated with Type II modifications, therefore, there is refractive index decrease in the tracks.
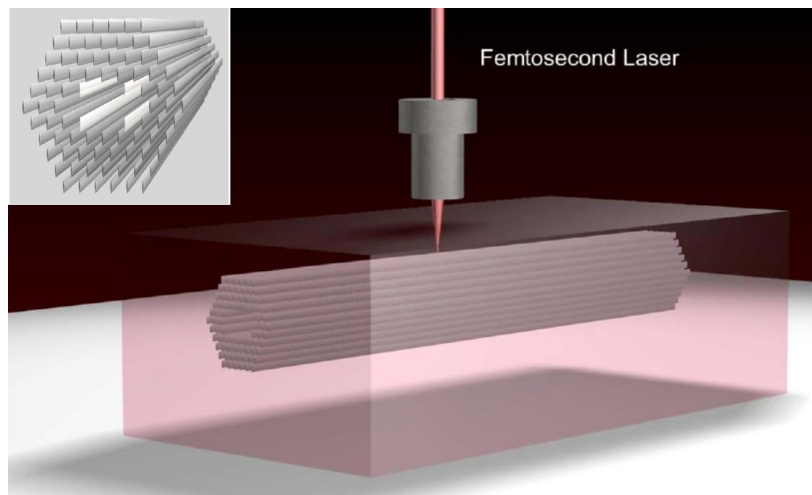
Fig. 5.14 Fabrication schematic plot of the photonic lattice-like structures. The inset image represents the cross section of the waveguide where the core is surrounded by a hexagonal track array [169].

5.3.2   Experiments

Waveguide fabrication

For the inscription of the waveguides, laser system described in section 3.2 which emits pulses with a duration of 120 fs centered at 795 nm and a repetition rate of 1kHz were used. To control the incident pulse energy a halfwave plate followed by a linear polarized in addition with a calibrated density filter were used. The sample was translated perpendicularly to the laser beam with constant speeds within the range from 300 to 800 μm/s, and the pulse energy varied between 0.25 and 0.5 μJ. In this case better results was found for a pulse energy of 0.4 μJ and scan speeds of 500 and 750 μm/s. The laser beam was focused through a 50$\times$ microscope objective 150 μm beneath the sample surface, which was moved by a computer controlled three-axes stage. For the study, 20 mm long waveguides were fabricated. The sample was a YAG crystal with dimensions 20 $\times$ 10 $\times$ 2 mm^3 and polished down to optical quality. Fig. 5.14 shows an schematic setup showing the process of fabrication of the waveguides.

Optical waveguide characterization

The optical properties of the inscribed waveguides were characterized by the end- fire technique. The beam laser was focused at the input face of the waveguide through a 10$\times$ microscope objective and the waveguide modes were recorded by imaging the output face of the waveguides through a 20$\times$ microscope objective onto a CCD camera. The waveguide loss characterizations were carried out by measuring the transmittance of the waveguides considering Fresnel reflections at the crystal interfaces. Further information about the experimental arrangement can be found in section 3.5.4.

5.3.3   Results and discussion

Fig. 5.15 (a) shows an optical micrograph of how the cross section of the inscribed structures looks like. The cross section of the structures is composed of eleven layers formed by several damaged tracks with a lateral separation of 6 μm forming a hexagonal structure with a diameter of $\approx$ 60 μm that emulates a photonic crystal fiber [171]. The dimension of the tracks varies depending on the laser inscription parameters. For lower scan speeds the damage region is increased while the longitude of the damaged tracks increased for higher per pulse energies. Different track separations were tested, finding better results for a separation of 6 μm which avoid cracks in the sample due to the overlapping of the damaged tracks and, at the same time, minimizes the light leakage between the tracks. The damaged tracks have a transverse

and longitudinal length of $\approx$2 and 4.7 μm respectively. The structure presents only one axial "defect" at the center which makes a core with a diameter of approximately 12 μm.
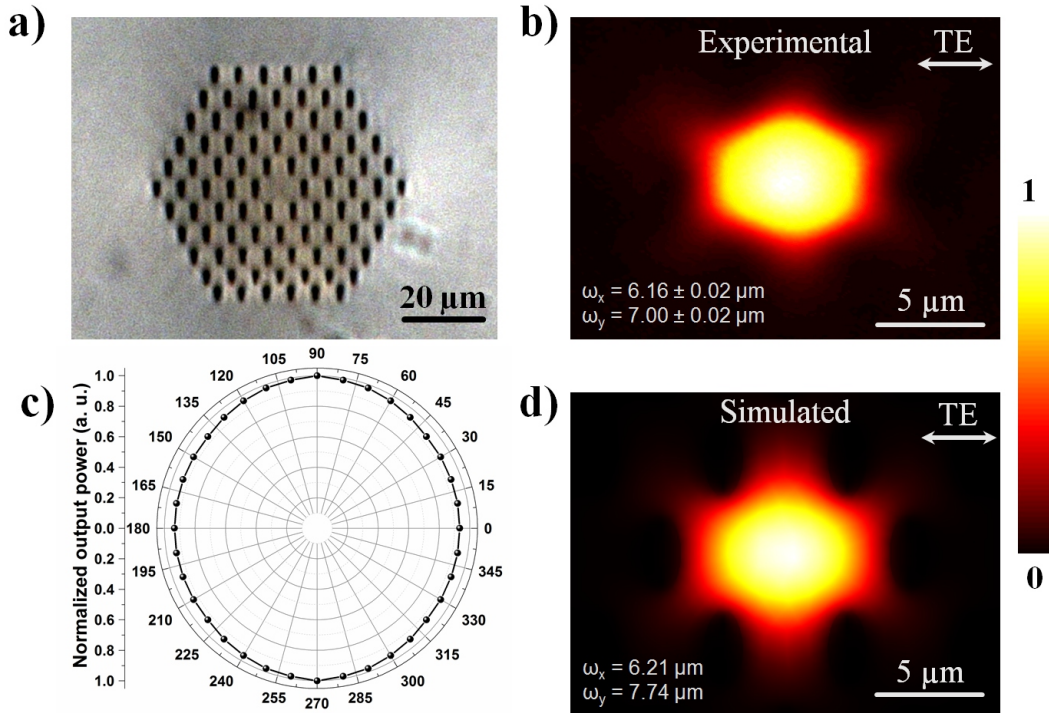
Fig. 5.15 Depressed hexagonal cladding waveguide with photonic structure fabricated with 0.4 μJ and a scan speed of 750 μm/s.

Fig. 5.15 (b) shows the near-field mode profile corresponding to polarization perpendicular to the damaged tracks (TE). It was found that this kind of structure support modes along both TE and TM polarizations. To obtain information of the polarization effects of the guidance, measurements at all angle light transmission were carried out by changing the polarization of the input beam (Fig. 5.15 (c)). In this case, it was found that the structures are polarization-independent, presenting an isotropic light confinement behavior.Concerning the propagation loss, it was determined to be an average value of 3 dB/cm at 633 nm. This value is comparable with the conventional depressed cladding waveguides fabricated in crystals as Nd:YAG [166], and can be reduced by coupling light of higher wavelengths [169]. Tab. 5.2 presents values of propagation loss for structures fabricated with different parameters. As it can be seen in the case of the TE polarization propagation loss seems to decrease for higher scan speeds, however, in the case of TM polarization there is only slight changes which suggest a better performance for waveguide fabricated at higher speed scans under the conditions of this experiments.

It is important to point it out that some differences were found depending on the numbers of layers of the structures resulting in slight changes such as the shape of the guided modes

Table 5.2 Values of propagation loss for different hexagonal cladding waveguides at 633 nm.

Waveguide	E (μJ)	Scan speed (μm/s)	α(dB/cm) ± 0.2	
			TE	TM
Wg1	0.36	500	4.3	2.8
Wg2	0.36	750	3.5	3.1
Wg3	0.4	500	3.9	2.7
Wg4	0.4	750	3.0	2.9

and light confinement. Regarding the refractive index contrast between irradiated zones and unmodified material, it was found a $\Delta n \approx 9 \times 10^{-3}$. This value was corroborated by carrying out a simulation shown in Fig. 5.15 (d). As it can be clearly seen there is a good agreement between the simulated and the measured near-field modes.

By seeing Fig. 5.15 (b) and (d) it is possible to note that light seems to escape from the core of the waveguide at this wavelength. Taking this characteristic into account a series of waveguides with multiple cores were fabricated to verify if light that leaks from the center could be coupled to additional adjacent cores. For this purpose simulations were carried out to verify the feasibility of the structure to convert a single beam into several light beams without the necessity of split the guided beam. These kind of structures opens the possibility to use them in the field of stellar interferometry as well as where multiple outputs are required [172–174]. This kind of structures also could be applied for the fabrication of photonic lanterns which are fabricated using multicore fibers [175].

As an example, Fig. 5.16 shows an optical micrograph of some multicore structures used in the study. The structures were fabricated using the same parameters of the waveguide shown in Fig. 5.15 and by introducing defects at different positions of the cross section. In this case the structures were firstly simulated and then the results were corroborated with the experimental data. Concerning optical loss propagation, the results were similar to those of the single core structure. On the other hand, the intensity of the adjacent modes, changes depending on the distribution of the defects. In the case of the structure of the Fig. 5.16 (a), adjacent modes present a decrement of 47% with respect to the central one. Structure of 5.16 (b) seems to be more efficient since it presents a decrement in the adjacent modes of 23% with respect to the central mode. By observing the experimental data it is possible to see adjacent modes with lower intensity. This is due to the position of the input beam at the end-face of the structure which is very sensible to slight misalignment. However, it is possible to conclude a good agreement of the experimental data by observing the simulation in Fig. 5.16 (b) were adjacent modes are more intense that adjacent modes of (a).
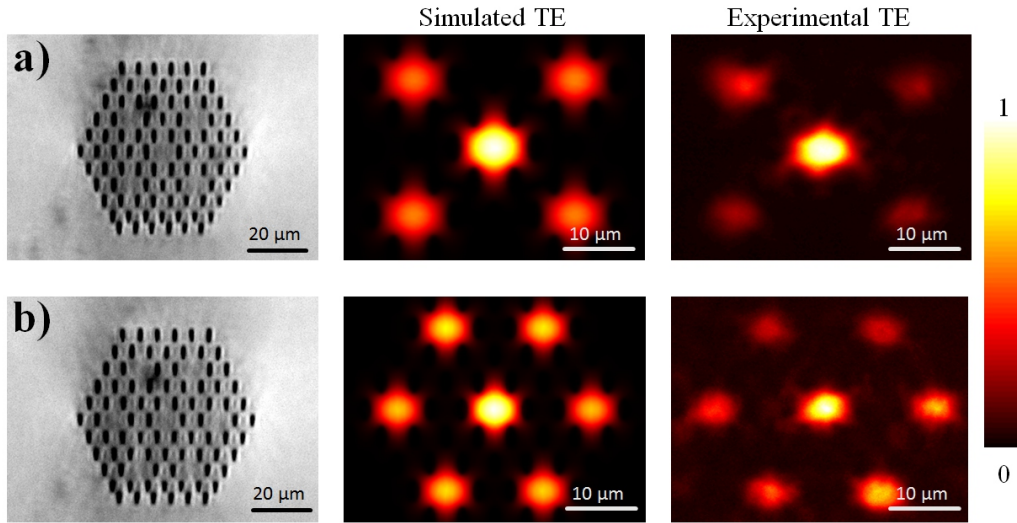
Fig. 5.16 Multicore depressed hexagonal cladding waveguide with photonic structure fabricated with 0.4 μJ and a scan speed of 750 μm/s.

Taking into account the versatility of this kind of structures a design for waveguides with superficial interaction was fabricated. This kind of structures are mainly proposed for their implementation the fabrication of integrated photonic sensors [176] offering the possibility to directly fabricate the waveguide near the surface of the sample without the necessity of a post-processing of the sample once the waveguide is fabricated. The structures were fabricated under similar parameters previously mentioned. In this case the structure is composed of six layers of tracks with five defects in the center forming a core of $\approx 20\mu$m that forms half of a hexagonal waveguide (see Fig. 5.17). For these experiments the laser beam was focused 20 μm beneath the surface sample and the largest layer was inscribed $\approx 7\mu$m from the surface. Better results in this case were found for per pulse energy of 0.8 μJ and scan speeds of 750 and 1000 μm/s. Fig. 5.17 (b) shows the TE near-field mode profile of the waveguide. As the previously waveguides presented before these waveguide support modes along both TE and TM polarizations. In the case of the polarization-dependence, it was found an almost isotropic behavior which can be clearly seen in Fig. 5.17 (c).

Concerning the refractive index contrast it was found a value of Δn $\approx 9.5 \times 10^{-3}$ which was corroborated by a simulation shown in Fig. 5.17 where it is possible to see a good agreement with the experimental near-field mode. On the other hand, propagation loss results to be reduced for scan speeds of 1000 μm/s. As an example, Table 5.3 shown some values of propagation loss for structures fabricated at different scan velocities.

Additionally, these kind of waveguides have been successfully demonstrated to be excellent and feasible structures for beam manipulation in both passive and active regimes citepJia2014.
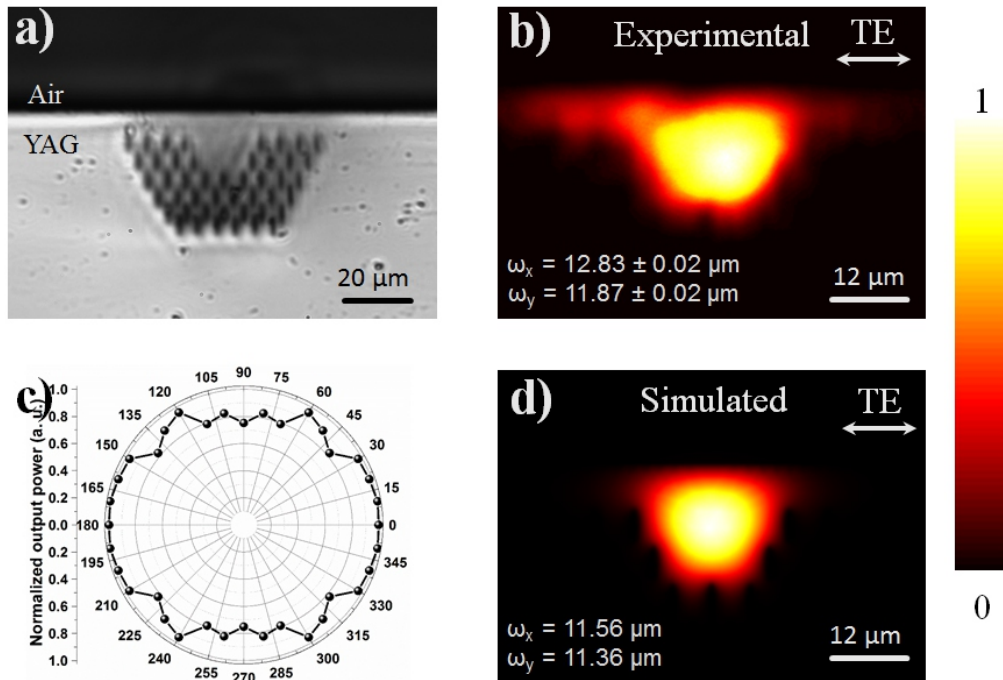
Fig. 5.17 Half-hexagonal depressed cladding waveguide fabricated near to the surface with 0.8 μJ and a scan speed of 1000 μm/s..(a) Optical micrograph of the photonic lattice like structure. b) Measured near-field modal profile. Polarization dependence of the half-hexagonal structure. d) Simulated near-field modal profile.

Table 5.3 Values of propagation loss for different half-hexagonal cladding waveguides at 633 nm.

Waveguide	E (μJ)	Scan speed (μm/s)	α(dB/cm) ± 0.15	
			TE	TM
Wg1	0.8	750	3.9	2.3
Wg2	0.8	1000	2.7	2.1

The process is relatively simple, light propagates through a first photonic element or structure with certain axial defects. In order to implement beam manipulation, additional axial defects or tracks are added or/and removed in appropriated positions along the whole cross section of the structure to obtain the desired device. The great feature of this kind of structures is the fact that complex photonic devices can be integrated in a monolithic structure. Fig. 5.18 a composed photonic structure for beam splitting.
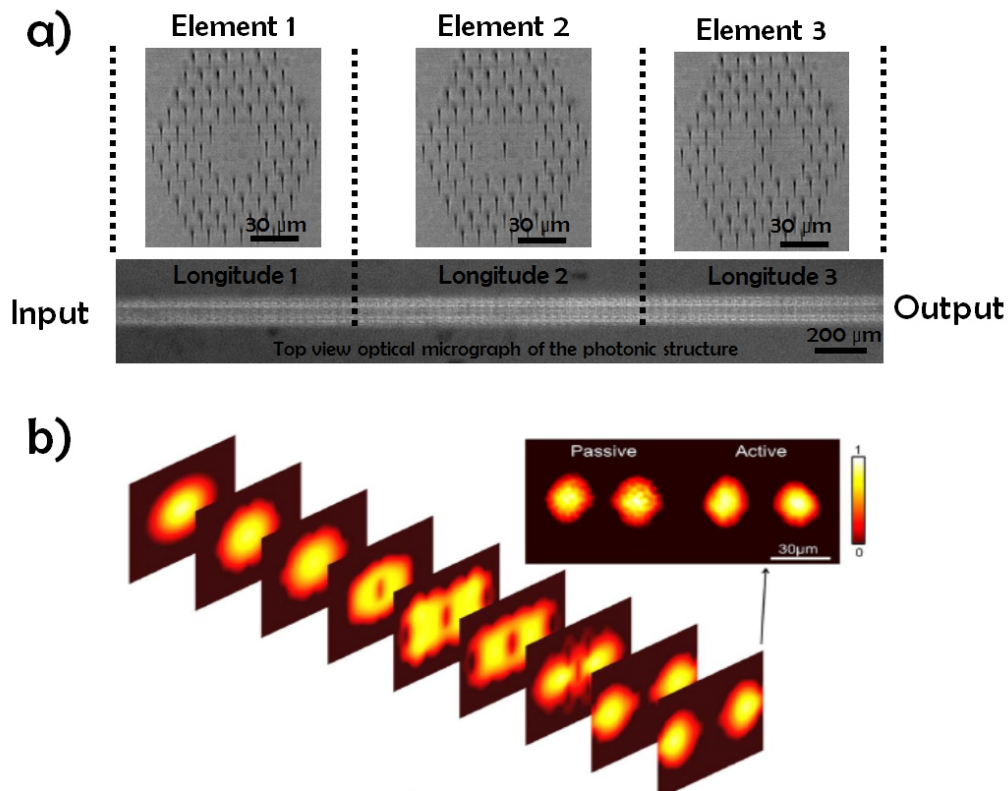
Fig. 5.18 a) Optical micrograph of the cross section of the femtosecond laser written photonic structures or elements and a topview micrograph of the whole structure. The fabrication of a beam splitter can be made by a combination of three different elements. b) Simulated beam profile evolution as light propagates along the photonic structure and measured intensity distributions of the beam splitter in both passive and active regimes at 1064 nm [169].

5.3.4 Conclusion

In conclusion, it has been designed a new kind of waveguides with hexagonal photonic lattice-like structure. The versatility of the structures has been demonstrated by introducing several axial defects that acts as a guiding core. In this kind of waveguide the input beam can be

converted into several beams without the necessity of splitting the input beam. On the other hand, the capability of the hexagonal structures was tested by designing waveguides with a larger core, which were successfully proven as a superficial interaction waveguide. The fabricated structures in this work present similar optical properties such as loss propagation, polarization-dependence and refractive index contrast.

Chapter 6

Temporal characterization of ultrafast laser inscribed waveguides

6.1 Introduction and motivation

Ultrashort laser pulses allow the fabrication of optical waveguides integrated in transparent dielectrics for the confinement and control of light. However, this kind of waveguides have been mainly used with continuous laser sources, and there are only a few studies on the response of the devices to the propagation of femtosecond pulses [177, 178]. The interest of manufacturing photonic devices for controlling pulse propagation is huge due to the possibility to perform complex functions, such as pulse splitting, amplification, or frequency conversion, in compact structures. In this section, a system in to characterize the propagation of ultrashort laser pulses (spectrally and temporally)through ultrafast laser inscribed waveguides by analyzing the dispersion properties is proposed. For the study, some of the waveguides analyzed in the previous chapter with different transverse geometry, such as stress-induced, depressed cladding waveguides and photonic lattice-like structures were used.

6.2 Spectral interferometry

The technique used in this study to characterize the propagation of the pulses in the waveguides is based on spectral interferometry (SI) [179] which is a well-known method to characterize ultrashort laser pulses. In this technique, is necessary a previous knowledge of a reference pulse. In this case the reference pulse can be characterized by using well-known standard techniques such as Frequency Resolved Optical Gating (FROG) [180] or Spectral Phase Interferometry for Direct Electric-field Reconstruction (SPIDER) [181] among others. The SI technique consists

in measuring the spectral interferences of two collinear beams (reference and test) with a certain delay between them. As a result, the spectrum of both beams consist in the sum of the spectra with an additional interference term which contains the information of the phase difference between the beams. The period of the interference fringes is given by the inverse of the delay (τ). For a sign criterion where the reference travels before the test, the resulting spectrum is given by [182]

$$S = S_{ref} + S_{test} + 2\sqrt{S_{ref}S_{test}}\cos\left(\phi_{test} - \phi_{ref} - \omega\tau\right), \qquad (6.1)$$

where S and ϕ correspond with the spectrum an the phase as a function of the angular frequency respectively. The procedure to find the test pulse phase is found trough the Fourier Transform Spectral Interferometry (FTSI) algorithm [179] . The first step consists in applying an inverse Fourier transform to the interference spectrum, which generates three peaks in the time domain (see Fig. 6.1). One peak is centered at $t = 0$ corresponding to the continuous contribution of each spectrum, and the other two centered at $t = \pm\tau$ that corresponds to the interference term. The next step consists in the filtering of one lateral peak. Then the filtered peak is returned to the spectral domain using the Fourier Transform, from where the phase difference between the test and reference ($\phi_{test} - \phi_{ref}$) is extracted. Therefore, by knowing the reference phase, the test spectral phase can be calculated and characterized in the temporal domain by applying an inverse Fourier transform. On the other hand, the delay is calculated from the position of the lateral peak and the term ωt is added to the retrieved phase. Further information and details of the FTSI algorithm can be found in [183].

It must be pointed out that the time delay (τ) must be high enough to prevent an overlap between the central and the lateral peaks, yet at the same time, it must be small enough to allow the fringes to be resolved by the spectrometer. Another important aspect is the fact that both test and reference spectral amplitude must be comparable to obtain well contrasted fringes [184].

6.3   Experiments

6.3.1   Waveguides fabrication

For the inscription of the waveguides, the femtosecond laser mentioned in section 3.2 was used. The laser beam was focused through a microscope objective several hundreds of microns beneath the sample surface, which was moved by a computer controlled three-axes stage. For the study, 20 mm long waveguides of double-scan (stress-induced waveguides) [185]
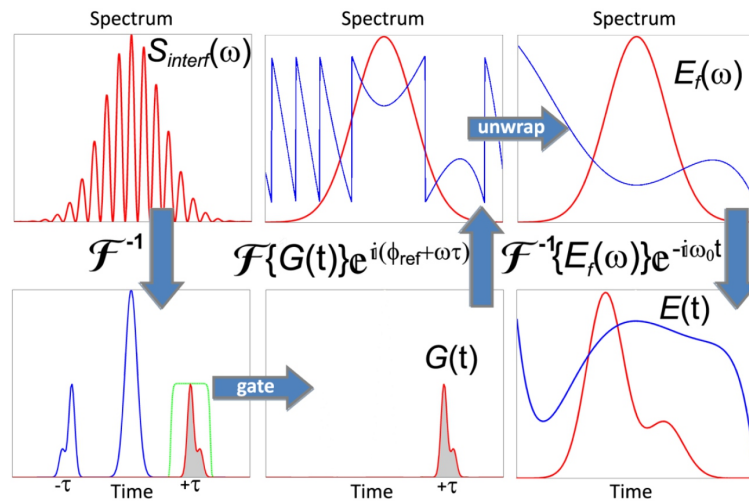
Fig. 6.1 Schematic diagram of the algorithm implemented for the Fourier transform Spectral Interferometry. Picture taken from [183].

and depressed cladding [?] with different geometries and sizes of the transverse section, were fabricated. Fig. 6.2 shows some fs laser inscribed waveguides used in the study. The waveguides were inscribed in a YAG crystal cut with dimensions $20 \times 10 \times 2$ mm^{3}and polished down to optical quality.
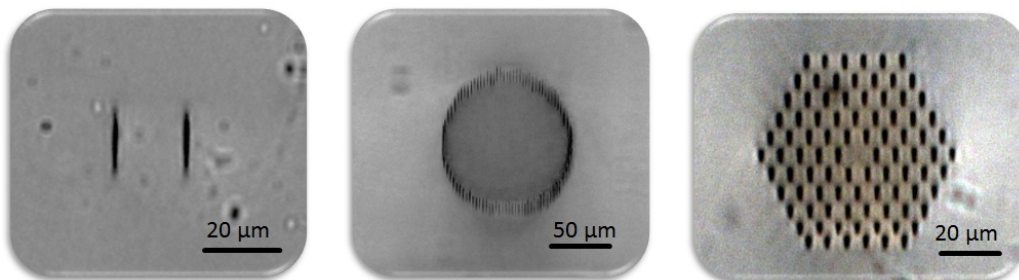
Fig. 6.2 Optical micrograph of ultrafast laser in-scribed waveguides. From left to right: stress-induced, circular depressed cladding, and photonic lattice-like waveguides.

6.3.2   Optical waveguide characterization

As before the optical properties of all inscribed waveguides were characterized by the end-fire technique using a $10\times$ microscope objective and the waveguide modes were recorded by imaging the output face of the waveguides through a $20\times$ microscope objective onto a

CCD camera. The waveguide loss characterizations were carried out according to the method described in section 3.5.

6.3.3   Temporal waveguide characterization

For the temporal characterization of the waveguides a fiber&free propagation mixed set-up [182] based in spectral interferometry was used. For the experiments, the same femtosecond laser at 795 nm used for the fabrication of the waveguides was coupled to the waveguides. In this case the beam was spatially filtered to suppressed additional spatial noise from the system and have a homogeneous reference pulse. For this purpose a system composed of lenses and a pinhole was used. To corroborate the effectivity of the filtering the spectrum of the beam was taken before and after the filter using a micro-metric stage in order to transversely scanned the spatial profile of the beam and the spectrum was acquired at every position. this experiments were carried out using an optical fiber directly connected to the spectrometer. Fig. 6.3 shows the spectra before and after the spatial filter. As it can be seen, there is a clear improvement of the beam after the filtering where there is not displacement of the spectra as function of the spatial position. It must be stressed that precautions were taken in order not to produce nonlinear effects at the focus in the air or to induce damage in the pinhole.
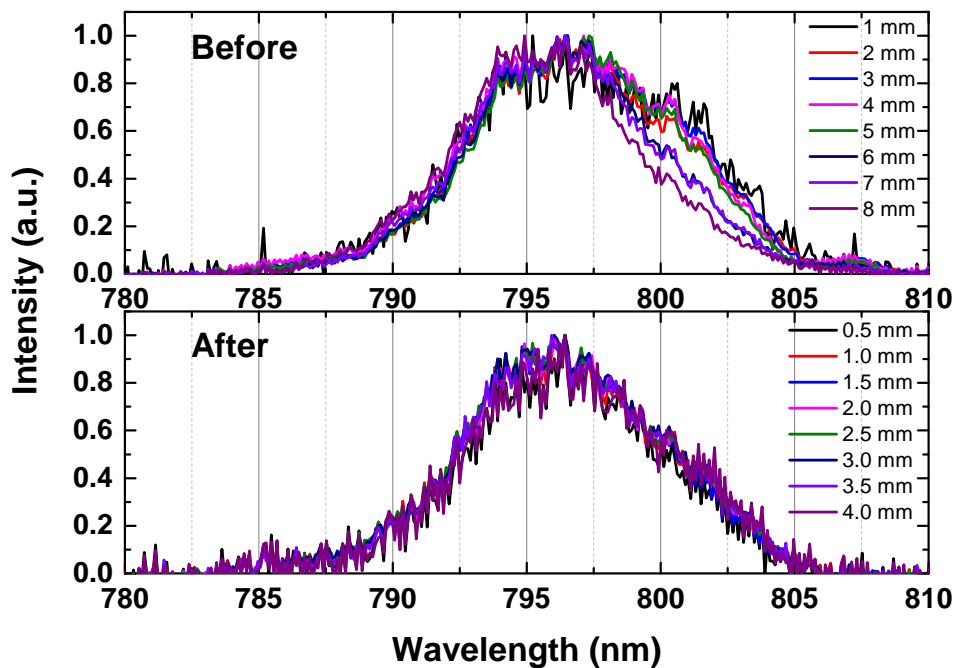
Fig. 6.3 Spectra before and after the spatial filtering of the reference beam.

On the other hand for the temporal characterization of the waveguides the pulse energy was controlled by using neutral density filters and fixed to be several orders of magnitude below the damage threshold of the sample and preventing nonlinear propagation effects. Linear polarization was used in all the experiments. Fig. 6.4 shows the experimental setup for the temporal characterization of the waveguides. The arrangement employs a single-mode fiber optic coupler which is composed by two input ports and a single output port coupled to a spectrometer. For the measurements, the laser beam is split, then one of the replicas (test) is coupled to the waveguides through the end-fire setup and the other (reference) is sent to another identical arrangement of lenses in such a way that they follow approximately the same optical path. The beams are then coupled to each fiber arm, where one of them is used to control the relative delay between the reference and test beams through its longitudinal position. According to Eq. 6.1, for all measurements a positive delay of 2 ps was introduced between the beams. For this purpose the reference arm was always put 600 μm before the test arm. Finally a calibration to compensate slight differences in the length of the arms of the fiber coupler that can introduce different dispersions on the beams was carried out. The calibration was carried out by taking a spectral interferometry measurement without a sample in the system. This measurement was then taken into account in the algorithm to retrieve the spectral phase. Additionally, spectral measurements of the YAG sample outside the waveguides was also carried out and taken into account.
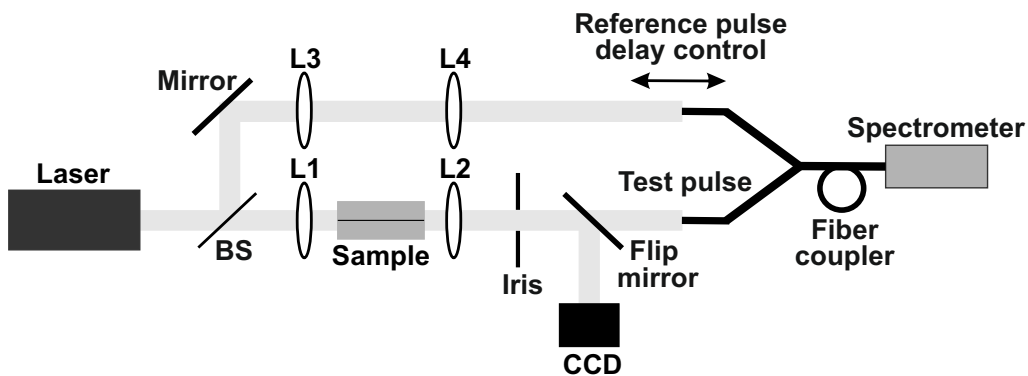
Fig. 6.4 Experimental setup for both optical and temporal characterization of the fs laser inscribed waveguides.

6.4   Results and discussion

6.4.1   Optical characterization

Firstly, the modal behavior of every fabricated waveguide was analyzed. For this study, waveguides with different mode size and behavior (single and multimode) were chosen. Fig. 6.5 shows the modal profile corresponding to some of the structures used in the study. Regarding the propagation loss of the structures this was similar to those found for waveguides described in the previous chapter. In the case of circular cladding waveguides an average value of 2 dB/cm was found. On the other hand, a value in the order of 10^3 for refractive index contrast (Δn) between the damaged tracks and the waveguide core was found for most of the inscribed structures.
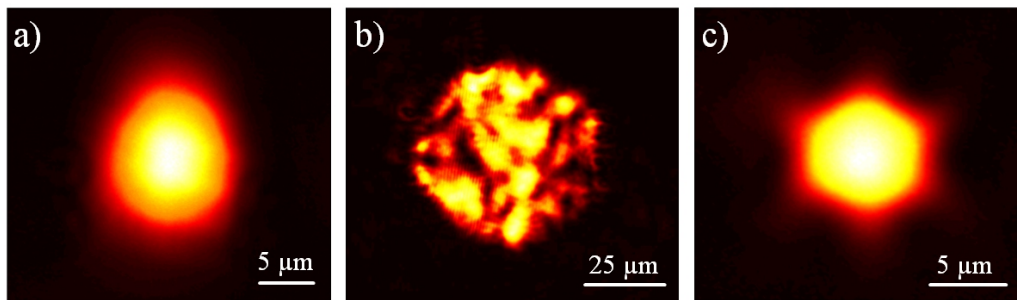
Fig. 6.5 Modal profiles at 633 nm of the ultrafast laser inscribed waveguides corresponding to: a) Stress induced (double line), b) Circular depressed cladding, and hexagonal cladding waveguides (photonic lattice-like structures).

6.4.2   Temporal characterization

The time resolved measurement procedure consists on taking both spectra separately, reference and test (from the sample), and the interference between both. As an example, Fig. 6.6 shows the measured spectra (reference pulse, test pulse and interferences) for a hexagonal waveguide with core size of 12 μm (see 6.2). As it can be clearly seen, it is possible to obtain good contrast fringes, which indicates the capability of the system for the characterization of ultrafast laser inscribed waveguides. By analyzing the results [182], spectral phase differences can be extracted.

The effect on time of propagation within several samples and types of waveguides (single mode, multimode, diverse geometry: double scan, depressed cladding, hexagonal cladding, Half-hexagonal cladding) was studied. As an example, Fig. 6.7 shows the dispersion effect on

the temporal duration of a circular depressed cladding waveguide (middle picture at 6.2) over a 100 fs pulse. The pulse at the exit of the waveguide is temporally broadened, presenting a duration of 131 fs (FWHM) and an overall positive chirp.
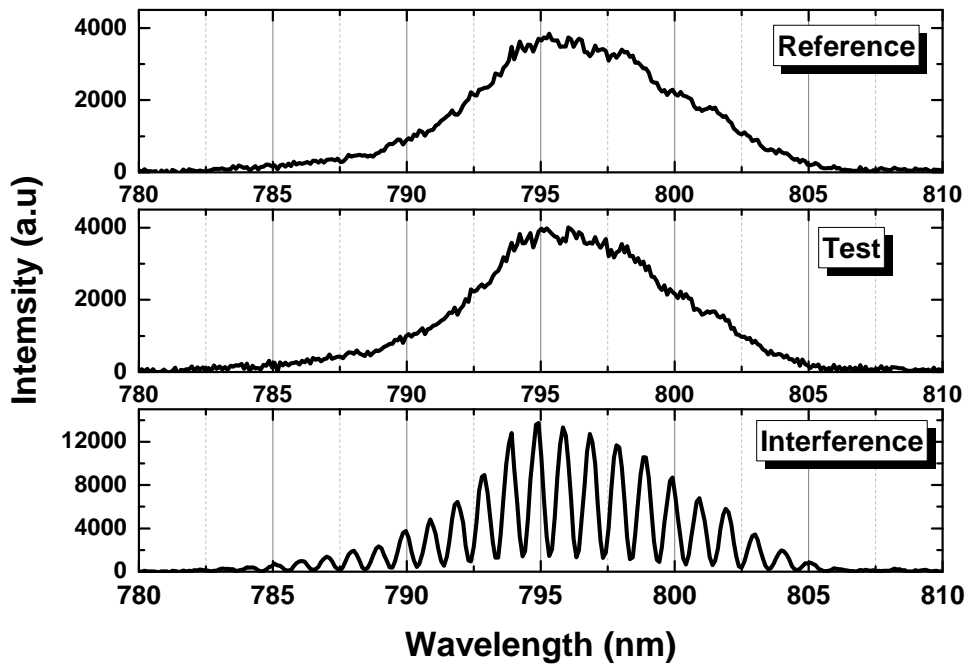
Fig. 6.6 Measured spectra for a photonic lattice-like structure with a core size of 12 μm.

On the other hand, it was found that the geometry of the waveguides has a major impact on the system overall dispersion and, thus, the effects on time domain over the pulse during its propagation. As a matter of fact, relevant results were found for the case of photonic lattice-like structures. In particular, these results were found for waveguides fabricated inside the sample in contrast with those that have an interaction with the surface (Half-hexagonal waveguides). Fig. 6.8 shows the effect of a hexagonal cladding waveguide (Fig. 6.2, picture on the right) on the pulse propagation. Considering an input pulse at Fourier limit conditions, the output pulse presents almost the same duration. This suggests that this kind of waveguide is able to compensate the material (YAG) inherent dispersion. This kind of behavior can be very useful for applications such as fabrication of photonic circuits conserving the pulse durations or more complex applications such as tailoring waveguides for solitonic pulse propagation, for instance.
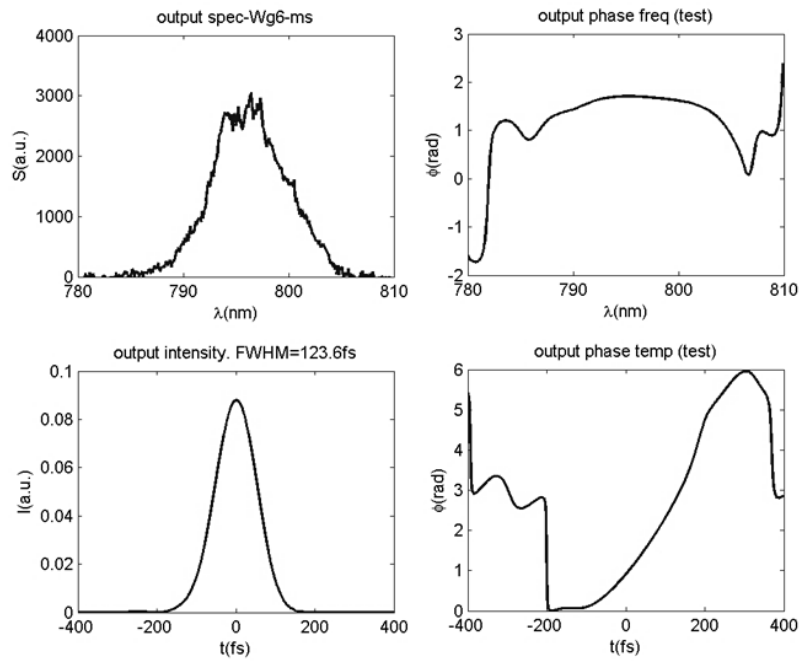
Fig. 6.7 Temporal characterization of the pulse propagating through a depressed cladding waveguide with a core size of 60 μm.
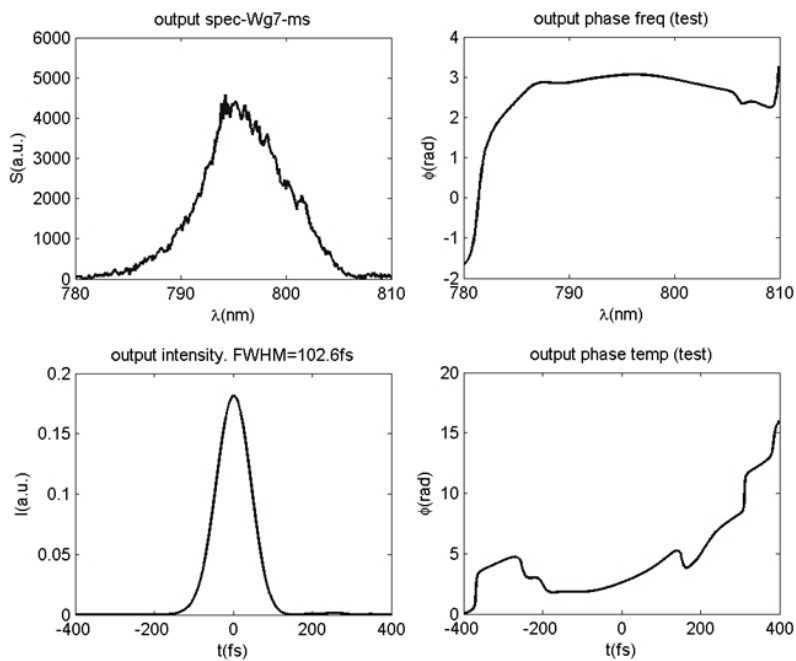
Fig. 6.8 Temporal characterization of the pulse propagating through a hexagonal cladding waveguide with a core size of 12 μm.

6.5   Conclusions

In conclusion, a study of the effect on the temporal features of ultrashort pulse propagation through waveguides fabricated in YAG by direct femtosecond laser irradiation has been presented. Waveguides with diverse geometry and size were used. It was found that in the case of photonic lattice-like structures, these have a minor impact over the time duration of the pulse during its propagation. This indicates that this kind of structure can compensate to some extent the material dispersion. The study was carried out using a system based on a fiber optic coupler interferometer. The main advantage of the system is the fact of being alignment-free since only a fiber coupler and a spectrometer are employed. The system was successfully proven for the temporal characterization of laser beams after their propagation for ultrafast laser inscribed waveguides.

Chapter 7

Conclusions

In summary, this work has been focused on the development and implementation of novel strategies for the fabrication of optical waveguides in transparent dielectric crystals by direct femtosecond laser inscription. New schemes for the fabrication and integration of photonic structures in optical materials, such as crystal and ceramics have been proposed and demonstrated. These new schemes successfully improve certain properties of the waveguides fabricated with "standard" techniques, such as propagation losses, modal profile quality, or 3D fabrication capabilities. The general conclusions of the present thesis are presented below.

- A new approach for the fabrication of stress-induced waveguides was proposed. The setup was based on an interferometer that allowed the perfect equalization of the energy of the two beams. The waveguides fabricated in this approach in Nd:YAG, were compared to those fabricated with the standard "double-line" technique, and the modal profiles and optical performances were shown to be different in both cases. Micro-luminescence characterization of the waveguides showed that the stress field induced with simultaneous irradiation was symmetrical, leading to symmetrical, single-mode and larger modal profiles in all the studied irradiation conditions. Moreover, waveguides fabricated by simultaneous double beam irradiation presented a significant reduction of propagation losses.

- Concerning depressed cladding waveguides, 3D arrays of hexagonal cladding waveguides have been successfully designed and fabricated by ultrafast laser inscription. The optical characterization of the structure revealed a complex multimodal propagation for the visible, and a nearly single-mode behavior for the NIR. No appreciable effects of the waveguide bends over the measured propagation losses of every single waveguide of the array were found. In this case, micro-luminescence maps showed that the induced damage during the waveguides fabrication was concentrated at the tracks, while a resid-

ual stress/strain field affects larger areas of the structures due to the inscription laser parameters. The results of the characterization suggest that this kind of structures could be used as photonic lanterns or for other 3D complex photonic circuits.

- A new kind of waveguides with hexagonal photonic lattice-like structure that emulates in shape the photonic crystal fibers have been designed and fabricated. The versatility of these structures has been demonstrated by introducing several axial defects that acts as a guiding core. In this kind of waveguide the input beam can be converted into several output beams, or a tailored shaping in the modal profile can be done. On the other hand, the capability of the hexagonal structures for 3D fabrication was tested by designing waveguides with a larger core, which were successfully proven as a superficial interaction waveguides. The structures fabricated in this work present similar optical properties such as loss propagation, polarization dependence and refractive-index contrast. Furthermore, it must be stressed that this kind of waveguides allows the beam manipulation by modifying the cross section of the waveguide through the whole structure. This feature provides an attractive method to fabricate monolithic microstructures with different photonic devices integrated as a single structure.

- A novel study of the effect on the temporal features of ultrashort pulse propagation through waveguides fabricated in a YAG crystal by direct femtosecond laser irradiation has been carried out. For the study, waveguides with diverse geometry and size were inscribed. Preliminary measurements suggest, as the most relevant result, that in photonic lattice-like structures the temporal features of the propagated pulses were maintained, thus compensating somehow the dispersive effect of the material. Numerical simulations must be carried out in order to confirm and to understand this effect

- Concerning the ultrafast laser irradiation of the nanostructured YSZ ceramic, that is a promising material for the integration of photonic devices for bio-medical applications, parameters such as the ablation threshold, incubation coefficient as well as the single-shot threshold and ablation rate were determined. Such parameters are necessary for the efficient micro-machining of the ceramic with femtosecond lasers. On the other hand, the nonlinear optical properties of YSZ ceramic were also estimated by the Z-scan technique. An inverse dependence between the oxygen vacancy concentration in the ceramics and the nonlinear optical coefficients was found. It was also estimated the components of the complex third-order optical susceptibility. Finally, it was demonstrated that it is possible to fabricate optical waveguides in the nanostructured YSZ ceramic by femtosecond laser irradiation. Micro-Raman analysis of the damaged tracks of the waveguide and its surroundings, revealed that the crystalline nature and phase of the YSZ ceramic are not

compromised by the ultrahigh peak irradiance laser-interaction which is also an important characteristic for the potential use of this material as host for waveguide lasers.

References

[1] K. Sugioka, "Progress in ultrafast laser processing and future prospects," *Nanophotonics*, vol. 6, pp. 393–413, jan 2017.

[2] K. M. Davis, K. Miura, N. Sugimoto, and K. Hirao, "Writing waveguides in glass with a femtosecond laser," *Optics Letters*, vol. 21, p. 1729, nov 1996.

[3] K. Miura, J. Qiu, H. Inouye, T. Mitsuyu, and K. Hirao, "Photowritten optical waveguides in various glasses with ultrashort pulse laser," *Applied Physics Letters*, vol. 71, no. 23, pp. 3329–3331, 1997.

[4] K. Hirao and K. Miura, "Writing waveguides and gratings in silica and related materials by a femtosecond laser," *Journal of Non-Crystalline Solids*, vol. 239, no. 1-3, pp. 91–95, 1998.

[5] Y. Sikorski, A. A. Said, P. Bado, R. Maynard, C. Florea, and K. A. Winick, "Optical waveguide amplifier in Nd-doped glass written with near-IR femtosecond laser pulses," *Electronics Letters*, vol. 36, no. 3, pp. 226–227, 2000.

[6] A. M. Streltsov and N. F. Borrelli, "Fabrication and analysis of a directional coupler written in glass by nanojoule femtosecond laser pulses," *Optics Letters*, vol. 26, no. 1, p. 42, 2001.

[7] K. Minoshima, A. M. Kowalevicz, E. P. Ippen, and J. G. Fujimoto, "Fabrication of coupled mode photonic devices in glass by nonlinear femtosecond laser materials processing," *Optics Express*, vol. 10, no. 15, pp. 645–652, 2002.

[8] C. Florea and K. A. Winick, "Fabrication and characterization of photonic devices directly written in glass using femtosecond laser pulses," *Journal of Lightwave Technology*, vol. 21, no. 1, pp. 246–253, 2003.

[9] S. Taccheo, G. D. Valle, R. Osellame, G. Cerullo, N. Chiodo, P. Laporta, O. Svelto, A. Killi, U. Morgner, M. Lederer, and D. Kopf, "Er:Yb-doped waveguide laser fabricated by femtosecond laser pulses," *Optics Letters*, vol. 29, no. 22, pp. 2626–2628, 2004.

[10] M. Kamata, M. Obara, R. R. Gattass, L. R. Cerami, and E. Mazur, "Optical vibration sensor fabricated by femtosecond laser micromachining," *Applied Physics Letters*, vol. 87, no. 5, pp. 1–4, 2005.

[11] Y. Tan, F. Chen, J. R. Vázquez de Aldana, H. Yu, and H. Zhang, "Tri-wavelength laser generation based on neodymium doped disordered crystal waveguide.," *Optics Express*, vol. 21, no. 19, pp. 22263–8, 2013.

[12] G. Salamu, F. Jipa, M. Zamfirescu, and N. Pavel, "Cladding waveguides realized in Nd:YAG ceramic by direct femtosecond-laser writing with a helical movement technique," *Optical Materials Express*, vol. 4, no. 4, p. 790, 2014.

[13] C. Cheng, H. Liu, Z. Shang, W. Nie, Y. Tan, B. d. R. Rabes, J. R. Vázquez de Aldana, D. Jaque, and F. Chen, "Femtosecond laser written waveguides with MoS_2 as satuable absorber for passively Q-switched lasing," *Optical Materials Express*, vol. 6, no. 2, p. 367, 2016.

[14] J. G. Ajates, C. Romero, G. R. Castillo, F. Chen, and J. R. V?zquez de Aldana, "Y-junctions based on circular depressed-cladding waveguides fabricated with femtosecond pulses in Nd:YAG crystal: A route to integrate complex photonic circuits in crystals," *Optical Materials*, vol. 72, pp. 220–225, oct 2017.

[15] T. Meany, "www.laserfocusworld.com," 2014.

[16] M. Lenzner, J. Krüger, S. Sartania, Z. Cheng, C. Spielmann, G. Mourou, W. Kautek, and F. Krausz, "Femtosecond Optical Breakdown in Dielectrics," *Physical Review Letters*, vol. 80, no. 18, pp. 4076–4079, 1998.

[17] A. Zoubir, C. Lopez, M. Richardson, and K. Richardson, "Femtosecond laser fabrication of tubular waveguides in poly(methyl methacrylate).," *Optics letters*, vol. 29, no. 16, pp. 1840–1842, 2004.

[18] A. H. Nejadmalayeri, P. R. Herman, J. Burghoff, M. Will, S. Nolte, and A. Tünnermann, "Inscription of optical waveguides in crystalline silicon by mid-infrared femtosecond laser pulses," *Optics Letters*, vol. 30, no. 9, p. 964, 2005.

[19] N. D. Psaila, R. R. Thomson, H. T. Bookey, S. Shen, N. Chiodo, R. Osellame, G. Cerullo, A. Jha, and A. K. Kar, "Supercontinuum generation in an ultrafast laser\ninscribed chalcogenide glass waveguide," *Optics Express*, vol. 15, no. 24, pp. 15776–15781, 2007.

[20] A. Ferrer, V. Diez-Blanco, A. Ruiz, J. Siegel, and J. Solis, "Deep subsurface optical waveguides produced by direct writing with femtosecond laser pulses in fused silica and phosphate glass," *Applied Surface Science*, vol. 254, no. 4, pp. 1121–1125, 2007.

[21] M. Ams, G. D. Marshall, P. Dekker, M. Dubov, V. K. Mezentsev, I. Bennion, and M. J. Withford, "Investigation of ultrafast laser-photonic material interactions: Challenges for directly written glass photonics," *IEEE Journal on Selected Topics in Quantum Electronics*, vol. 14, no. 5, pp. 1370–1388, 2008.

[22] D. M. Krol, "Femtosecond laser modification of glass," *Journal of Non-Crystalline Solids*, vol. 354, no. 2-9, pp. 416–424, 2008.

[23] M. Ams, G. D. Marshall, P. Dekker, J. A. Piper, and M. J. Withford, "Ultrafast laser written active devices," *Laser and Photonics Reviews*, vol. 3, no. 6, pp. 535–544, 2009.

[24] R. Mary, S. J. Beecher, G. Brown, R. R. Thomson, D. Jaque, S. Ohara, and A. K. Kar, "Compact, highly efficient ytterbium doped bismuthate glass waveguide laser," *Optics Letters*, vol. 37, no. 10, p. 1691, 2012.

[25] T. Pertsch, U. Peschel, F. Lederer, J. Burghoff, M. Will, S. Nolte, and A. Tünnermann, "Discrete diffraction in two-dimensional arrays of coupled waveguides in silica.," *Optics letters*, vol. 29, no. 5, pp. 468–70, 2004.

[26] J. C. Ng, C. Li, P. R. Herman, and L. Qian, "Femtosecond laser writing of a flat-top interleaver via cascaded Mach-Zehnder interferometers," *Opt. Express*, vol. 20, no. 16, pp. 17894–17903, 2012.

[27] G. D. Marshall, M. Ams, and M. J. Withford, "Direct laser written waveguide-Bragg gratings in bulk fused silica," *Optics Letters*, vol. 31, no. 18, p. 2690, 2006.

[28] J. Burghoff, C. Grebing, S. Nolte, and A. Tünnermann, "Efficient frequency doubling in femtosecond laser-written waveguides in lithium niobate," *Applied Physics Letters*, vol. 89, p. 081108, aug 2006.

[29] W. F. Silva, C. Jacinto, A. Benayas, J. R. Vazquez de Aldana, G. A. Torchia, F. Chen, Y. Tan, and D. Jaque, "Femtosecond-laser-written, stress-induced Nd:YVO4 waveguides preserving fluorescence and Raman gain.," *Optics letters*, vol. 35, no. 7, pp. 916–8, 2010.

[30] A. Benayas, W. F. Silva, C. Jacinto, E. Cantelar, J. Lamela, F. Jaque, J. R. Vázquez de Aldana, G. a. Torchia, L. Roso, a. a. Kaminskii, and D. Jaque, "Thermally resistant waveguides fabricated in Nd:YAG ceramics by crossing femtosecond damage filaments.," *Optics letters*, vol. 35, no. 3, pp. 330–2, 2010.

[31] A. G. Okhrimchuk, A. V. Shestakov, I. Khrushchev, and J. Mitchell, "Depressed cladding, buried waveguide laser formed in a YAG:Nd^3+ crystal by femtosecond laser writing," *Optics Letters*, vol. 30, p. 2248, sep 2005.

[32] J. R. Vázquez de Aldana, P. Moreno, and L. Roso, "Ultrafast lasers: A new frontier for optical materials processing," *Optical Materials*, vol. 34, pp. 572–578, jan 2012.

[33] C. B. Schaffer, A. Brodeur, J. F. Garci'a, and E. Mazur, "Micromachining bulk glass by use of femtosecond laser pulses with nanojoule energy," *Optics Letters*, vol. 26, no. 2, pp. 93–95, 2001.

[34] G. A. Torchia, A. Rodenas, A. Benayas, E. Cantelar, L. Roso, and D. Jaque, "Highly efficient laser action in femtosecond-written Nd:yttrium aluminum garnet ceramic waveguides," *Applied Physics Letters*, vol. 92, p. 111103, mar 2008.

[35] R. R. Gattass and E. Mazur, "Femtosecond laser micromachining in transparent materials," *Nature Photonics*, vol. 2, pp. 219–225, apr 2008.

[36] S. Maruo and J. T. Fourkas, "Recent progress in multiphoton microfabrication," *Laser and Photonics Reviews*, vol. 2, no. 1-2, pp. 100–111, 2008.

[37] S. Juodkazis, V. Mizeikis, and H. Misawa, "Three-dimensional microfabrication of materials by femtosecond lasers for photonics applications," *Journal of Applied Physics*, vol. 106, no. 5, 2009.

[38] Y. L. Zhang, Q. D. Chen, H. Xia, and H. B. Sun, "Designable 3D nanofabrication by femtosecond laser direct writing," *Nano Today*, vol. 5, no. 5, pp. 435–448, 2010.

[39] K. Sugioka and Y. Cheng, "Integrated microchips for biological analysis fabricated by femtosecond laser direct writing," *MRS Bulletin*, vol. 36, no. 12, pp. 1020–1027, 2011.

[40] Y. Liao, J. Song, E. Li, Y. Luo, Y. Shen, D. Chen, Y. Cheng, Z. Xu, K. Sugioka, and K. Midorikawa, "Rapid prototyping of three-dimensional microfluidic mixers in glass by femtosecond laser direct writing," *Lab on a Chip*, vol. 12, no. 4, p. 746, 2012.

[41] Y. Liao, Y. Shen, L. Qiao, D. Chen, Y. Cheng, K. Sugioka, and K. Midorikawa, "Femtosecond laser nanostructuring in porous glass with sub-50nm feature sizes," *Optics Letters*, vol. 38, no. 2, p. 187, 2013.

[42] D. Choudhury, J. R. Macdonald, and A. K. Kar, "Ultrafast laser inscription: Perspectives on future integrated applications," *Laser and Photonics Reviews*, vol. 8, no. 6, pp. 827–846, 2014.

[43] W. Sohler, H. Hu, R. Ricken, V. Quiring, C. Vannahme, H. Herrmann, D. Büchter, S. Reza, W. Grundkötter, S. Orlov, H. Suche, R. Nouroozi, and Y. Min, "Integrated Optical Devices in Lithium Niobate," *Optics and Photonics News*, vol. 19, p. 24, jan 2008.

[44] A. Crespi, R. Ramponi, R. Osellame, L. Sansoni, I. Bongioanni, F. Sciarrino, G. Vallone, and P. Mataloni, "Integrated photonic quantum gates for polarization qubits," *Nature Communications*, vol. 2, p. 566, nov 2011.

[45] R. Osellame, H. Hoekstra, G. Cerullo, and M. Pollnau, "Femtosecond laser microstructuring: an enabling tool for optofluidic lab-on-chips," *Laser & Photonics Reviews*, vol. 5, pp. 442–463, may 2011.

[46] D. Homoelle, S. Wielandy, A. L. Gaeta, N. F. Borrelli, and C. Smith, "Infrared photosensitivity in silica glasses exposed to femtosecond laser pulses," *Optics Letters*, vol. 24, no. 18, p. 1311, 1999.

[47] S. Nolte, M. Will, J. Burghoff, and A. Tuennermann, "Femtosecond waveguide writing: A new avenue to three-dimensional integrated optics," *Applied Physics A: Materials Science and Processing*, vol. 77, no. 1, pp. 109–111, 2003.

[48] A. M. Kowalevicz, V. Sharma, E. P. Ippen, J. G. Fujimoto, and K. Minoshima, "Three-dimensional photonic devices fabricated in glass by use of a femtosecond laser oscillator," *Optics Letters*, vol. 30, no. 9, p. 1060, 2005.

[49] A. Crespi, Y. Gu, B. Ngamsom, H. J. W. M. Hoekstra, C. Dongre, M. Pollnau, R. Ramponi, H. H. van den Vlekkert, P. Watts, G. Cerullo, and R. Osellame, "Three-dimensional Mach-Zehnder interferometer in a microfluidic chip for spatially-resolved label-free detection," *Lab on a Chip*, vol. 10, no. 9, p. 1167, 2010.

[50] A. Martinez, M. Dubov, I. Khrushchev, and I. Bennion, "Direct writing of fibre bragg gratings by femtosecond laser," *Electron. Lett.*, vol. 40, no. 19, 2004.

[51] R. Osellame, S. Taccheo, G. Cerullo, M. Marangoni, D. Polli, R. Ramponi, P. Laporta, and S. De Silvestri, "Optical gain in Er-Yb doped waveguides fabricated by femtosecond laser pulses," *Electronics Letters*, vol. 38, no. 17, p. 964, 2002.

[52] G. Della Valle, R. Osellame, N. Chiodo, S. Taccheo, G. Cerullo, P. Laporta, A. Killi, U. Morgner, M. Lederer, and D. Kopf, "C-band waveguide amplifier produced by femtosecond laser writing," *Optics Express*, vol. 13, no. 16, pp. 5976–5982, 2005.

[53] S. J. Beecher, R. R. Thomson, N. D. Psaila, Z. Sun, T. Hasan, A. G. Rozhin, A. C. Ferrari, and A. K. Kar, "320 Fs Pulse Generation From an Ultrafast Laser Inscribed Waveguide Laser Mode-Locked By a Nanotube Saturable Absorber," *Applied Physics Letters*, vol. 97, no. 11, pp. 2–4, 2010.

[54] M. Ams, P. Dekker, G. D. Marshall, and M. J. Withford, "Ultrafast laser-written dual-wavelength waveguide laser," *Optics Letters*, vol. 37, no. 6, p. 993, 2012.

[55] D. G. Lancaster, S. Gross, A. Fuerbach, M. J. Withford, and T. M. Monro, "2.1 μm waveguide laser fabricatedby femtosecond laser direct-writing in Ho 3 , Tm 3 : ZBLAN glass," *Optics Letters*, vol. 37, no. 6, pp. 996–998, 2012.

[56] T. Sabapathy, A. Ayiriveetil, A. K. Kar, S. Asokan, S. J. Beecher, . S. M. Eaton, H. Zhang, M. L. Ng, J. Li, W. J. Chen, S. Ho, and P. R. Herman, "Direct ultrafast laser written C-band waveguide amplifier in Er-doped chalcogenide glass," *Series in Optical Sciences Nat. Photonics J. Non-Cryst. Solids Am. B J. Optoelectron. Adv. Mater. Z. G. Ivanova, E. Cernoskova, Z. Cernosek, and M. Vlcek*, vol. 5, no. 737, pp. 23–34, 2003.

[57] T. T. Fernandez, S. M. Eaton, G. Della Valle, R. M. Vazquez, M. Irannejad, G. Jose, A. Jha, G. Cerullo, R. Osellame, and P. Laporta, "Femtosecond laser written optical waveguide amplifier in phospho-tellurite glass.," *Optics Express*, vol. 18, no. 19, pp. 20289–20297, 2010.

[58] K. Chaitanya Vishnubhatla, J. Clark, G. Lanzani, R. Ramponi, R. Osellame, and T. Virgili, "Femtosecond laser fabrication of microfluidic channels for organic photonic devices," *Applied Optics*, vol. 48, pp. G114–G118, nov 2009.

[59] R. Osellame, G. Cerullo, and R. Ramponi, *Femtosecond laser micromachining: photonic and microfluidic devices in transparent materials*. Topics in Applied Physics, Berlin, Heidelberg: Springer Science & Business Media, 2012.

[60] G. D. Marshall, A. Politi, J. C. F. Matthews, P. Dekker, M. Ams, M. J. Withford, and J. L. O'Brien, "Laser written waveguide photonic quantum circuits," vol. 17, no. 15, pp. 646–649, 2009.

[61] F. Chen and J. R. V. de Aldana, "Optical waveguides in crystalline dielectric materials produced by femtosecond-laser micromachining," *Laser & Photonics Reviews*, vol. 8, pp. 251–275, mar 2014.

[62] R. Thomson, C. Leburn, and D. Reid, *Ultrafast nonlinear optics*. Heidelberg, New York, Dordrecht, London: Springer International Publishing, 2013.

[63] Y. U. Peter and A. Cardona, *Fundamentals of semiconductors: physics and materials properties*. New York: Springer Science & Business Media, 2010.

[64] C. B. Schaffer, A. Brodeur, and E. Mazur, "Laser-induced breakdown and damage in bulk transparent materials induced by tightly focused femtosecond laser pulses," *Measurement Science and Technology*, vol. 12, no. 11, pp. 1784–1794, 2001.

[65] A. Oraevsky, L. Da Silva, A. Rubenchik, M. Feit, M. Glinsky, M. Perry, B. Mammini, W. Small, and B. Stuart, "Plasma mediated ablation of biological tissues with nanosecond-to-femtosecond laser pulses: relative role of linear and nonlinear absorption," *IEEE Journal of Selected Topics in Quantum Electronics*, vol. 2, no. 4, pp. 801–809, 1996.

[66] B. C. Stuart, M. D. Feit, A. M. Rubenchik, B. W. Shore, and M. D. Perry, "Laser-Induced Damage in Dielectrics with Nanosecond to Subpicosecond Pulses," *Physical Review Letters*, vol. 74, pp. 2248–2251, mar 1995.

[67] C. Chaleard, V. Detalle, S. Kocon, J.-L. Lacour, P. Mauchien, P. Meynadier, C. Nouvellon, P. Palianov, M. Perdrix, G. Petite, B. Salle, and A. F. Semerok, "Influence of laser pulse duration on the ablation efficiency of metals," in *Proc. SPIE* (V. I. Pustovoy, ed.), vol. 3404, pp. 441–448, may 1998.

[68] K. C. Phillips, H. H. Gandhi, E. Mazur, and S. K. Sundaram, "Ultrafast laser processing of materials: a review," *Advances in Optics and Photonics*, vol. 7, no. 4, p. 684, 2015.

[69] C. Momma, S. Nolte, B. N. Chichkov, F. v. Alvensleben, and A. T?nnermann, "Precise laser ablation with ultrashort pulses," *Applied Surface Science*, vol. 109-110, pp. 15–19, feb 1997.

[70] N. Anderson, L. Wang, and T. Erdogan, "www.semrock.com," 2010.

[71] R. R. Gattass, L. R. Cerami, and E. Mazur, "Micromachining of bulk glass with bursts of femtosecond laser pulses at variable repetition rates," *Optics Express*, vol. 14, no. 12, p. 5279, 2006.

[72] S. Eaton, H. Zhang, P. Herman, F. Yoshino, L. Shah, J. Bovatsek, and A. Arai, "Heat accumulation effects in femtosecond laser-written waveguides with variable repetition rate.," *Optics Express*, vol. 13, no. 12, pp. 4708–4716, 2005.

[73] S. M. Eaton, H. Zhang, M. L. Ng, J. Li, W.-J. Chen, S. Ho, and P. R. Herman, "Transition from thermal diffusion to heat accumulation in high repetition rate femtosecond laser writing of buried optical waveguides," *Optics Express*, vol. 16, no. 13, p. 9443, 2008.

[74] S. Juodkazis, H. Misawa, and I. Maksimov, "Thermal accumulation effect in three-dimensional recording by picosecond pulses," *Applied Physics Letters*, vol. 85, no. 22, pp. 5239–5241, 2004.

[75] G. R. Castillo-Vega, E. H. Penilla, S. Camacho-López, G. Aguilar, and J. E. Garay, "Waveguide-like structures written in transparent polycrystalline ceramics with an ultra-low fluence femtosecond laser," *Optical Materials Express*, vol. 2, no. 10, p. 1416, 2012.

[76] A. Benayas, W. F. Silva, A. Ródenas, C. Jacinto, J. Vázquez De Aldana, F. Chen, Y. Tan, R. R. Thomsom, N. D. Psaila, D. T. Reid, G. A. Torchia, A. K. Kar, and D. Jaque, "Ultrafast laser writing of optical waveguides in ceramic Yb:YAG: A study of thermal and non-thermal regimes," *Applied Physics A: Materials Science and Processing*, vol. 104, no. 1, pp. 301–309, 2011.

[77] J. W. Chan, T. R. Huser, S. H. Risbud, J. S. Hayden, and D. M. Krol, "Waveguide fabrication in phosphate glasses using femtosecond laser pulses," *Applied Physics Letters*, vol. 82, no. 15, pp. 2371–2373, 2003.

[78] R. R. Gattass and E. Mazur, ""Wiring" Light with Femtosecond Laser Pulses"," *Photonics Spectra*, vol. 38, pp. 58–64, 2004.

[79] S. Gross, M. Dubov, and M. J. Withford, "On the use of the Type I and II scheme for classifying ultrafast laser direct-write photonics," *Optics Express*, vol. 23, p. 7767, mar 2015.

[80] H. T. Bookey, R. R. Thomson, N. D. Psaila, A. K. Kar, N. Chiodo, R. Osellame, and G. Cerullo, "Femtosecond Laser Inscription of Low Insertion Loss Waveguides in Z-Cut Lithium Niobate," *IEEE Photonics Technology Letters*, vol. 19, pp. 892–894, jun 2007.

[81] J. R. Macdonald, R. R. Thomson, N. D. Psaila, S. J. Beecher, H. T. Bookey, and A. K. Kar, "Ultrafast laser inscription of low loss waveguides in polycrystalline ZnSe," *2010 23rd Annual Meeting of the IEEE Photonics Society, PHOTINICS 2010*, vol. 35, no. 23, pp. 56–57, 2010.

[82] A. H. Nejadmalayeri and P. R. Herman, "Ultrafast laser waveguide writing: Lithium niobate and the role of circular polarization and picosecond pulse width.," *Optics Letters*, vol. 31, no. 20, pp. 2987–2989, 2006.

[83] R. Osellame, G. Della Valle, N. Chiodo, S. Taccheo, P. Laporta, O. Svelto, and G. Cerullo, "Lasing in femtosecond laser written optical waveguides," *Applied Physics A: Materials Science and Processing*, vol. 93, no. 1, pp. 17–26, 2008.

[84] A. M. Streltsov and N. F. Borrelli, "Study of femtosecond-laser-written waveguides in glasses," *Journal of the Optical Society of America B*, vol. 19, p. 2496, oct 2002.

[85] C. Schaffer, J. Garcia, and E. Mazur, "Bulk heating of transparent materials using a high-repetition-rate femtosecond laser," *Applied Physics A: Materials Science & Processing*, vol. 76, pp. 351–354, mar 2003.

[86] J. W. Chan, T. Huser, S. Risbud, and D. M. Krol, "Structural changes in fused silica after exposure to focused femtosecond laser pulses," *Optics Letters*, vol. 26, no. 21, p. 1726, 2001.

[87] J. Burghoff, C. Grebing, S. Nolte, and A. Tünnermann, "Waveguides in lithium niobate fabricated by focused ultrashort laser pulses," *Applied Surface Science*, vol. 253, no. 19, pp. 7899–7902, 2007.

[88] A. Ródenas, G. A. Torchia, G. Lifante, E. Cantelar, J. Lamela, F. Jaque, L. Roso, and D. Jaque, "Refractive index change mechanisms in femtosecond laser written ceramic Nd:YAG waveguides: micro-spectroscopy experiments and beam propagation calculations," *Applied Physics B*, vol. 95, pp. 85–96, apr 2009.

[89] C. Zhang, N. Dong, J. Yang, F. Chen, J. R. Vázquez de Aldana, and Q. Lu, "Channel waveguide lasers in Nd:GGG crystals fabricated by femtosecond laser inscription," *Optics Express*, vol. 19, p. 12503, jun 2011.

[90] J. Siebenmorgen, K. Petermann, G. Huber, K. Rademaker, S. Nolte, and A. Tünnermann, "Femtosecond laser written stress-induced Nd:Y3Al5O12 (Nd:YAG) channel waveguide laser," *Applied Physics B*, vol. 97, pp. 251–255, oct 2009.

[91] Y. Tan, J. Guan, F. Chen, J. R. Vazquez de Aldana, G. A. Torchia, A. Benayas, and D. Jaque, "Waveguides and Laser Patterning," in *Advances in Optical Materials*, 2011.

[92] Y. Tan, Y. Jia, F. Chen, J. R. Vázquez de Aldana, and D. Jaque, "Simultaneous dual-wavelength lasers at 1064 and 1342nm in femtosecond-laser-written Nd:YVO_4channel waveguides," *Journal of the Optical Society of America B*, vol. 28, no. 7, p. 1607, 2011.

[93] Y. Tan, A. Rodenas, F. Chen, R. R. Thomson, A. K. Kar, D. Jaque, and Q. Lu, "70% slope efficiency from an ultrafast laser-written Nd:GdVO4 channel waveguide laser.," *Optics Express*, vol. 18, no. 24, pp. 24994–24999, 2010.

[94] Y. Ren, N. Dong, J. Macdonald, F. Chen, H. Zhang, and A. K. Kar, "Continuous wave channel waveguide lasers in Nd:LuVO4 fabricated by direct femtosecond laser writing," *Optics Express*, vol. 20, no. 3, p. 1969, 2012.

[95] T. Calmano, J. Siebenmorgen, F. Reichert, M. Fechner, A.-g. Paschke, N.-o. Hansen, K. Petermann, and G. Huber, "Crystalline Pr:SrAl12O19 waveguide laser in the visible spectral region," *Optics Letters*, vol. 36, p. 4620, dec 2011.

[96] F. Laurell, T. Calmano, S. Müller, P. Zeil, C. Canalias, and G. Huber, "Laser-written waveguides in KTP for broadband Type II second harmonic generation," *Optics Express*, vol. 20, p. 22308, sep 2012.

[97] S. Zhang, J. Yao, W. Liu, Z. Huang, J. Wang, Y. Li, C. Tu, and F. Lu, "Second harmonic generation of periodically poled potassium titanyl phosphate waveguide using femtosecond laser pulses.," *Optics Express*, vol. 16, no. 18, pp. 14180–14185, 2008.

[98] S. Zhang, J. Yao, W. Liu, Z. Huang, and F. Lu, "Second-harmonic generation to green using ultrafast fibre source and femtosecond written periodically poled waveguide," *Electronics Letters*, vol. 46, no. 18, p. 1290, 2010.

[99] C. Tu, Z. Huang, S. Zhang, M. Hu, Q. Wang, E. Li, Y. Li, and F. Lu, "Second harmonic generation by femtosecond Yb-doped fiber laser source based on PPKTP waveguide fabricated by femtosecond laser direct writing," *Optics Communications*, vol. 284, no. 1, pp. 455–459, 2011.

[100] S. J. Beecher, R. R. Thomson, D. T. Reid, N. D. Psaila, M. Ebrahim-Zadeh, and A. K. Kar, "Strain field manipulation in ultrafast laser inscribed BiB3O6 optical waveguides for nonlinear applications.," *Optics Letters*, vol. 36, no. 23, pp. 4548–4550, 2011.

[101] Y. Ren, J. R. Vázquez de Aldana, F. Chen, and H. Zhang, "Channel waveguide lasers in Nd:LGS crystals," *Optics Express*, vol. 21, p. 6503, mar 2013.

[102] Y. Jia, J. R. V. de Aldana, C. Romero, Y. Ren, Q. Lu, and F. Chen, "Femtosecond-Laser-Inscribed BiB3O6 Nonlinear Cladding Waveguide for Second-Harmonic Generation," *Applied Physics Express*, vol. 5, no. 7, p. 72701, 2012.

[103] Y. Jia, J. R. Vázquez de Aldana, and F. Chen, "Efficient waveguide lasers in femtosecond laser inscribed double-cladding waveguides of Yb:YAG ceramics," *Optical Materials Express*, vol. 3, no. 5, p. 645, 2013.

[104] Y. Ren, F. Chen, and J. R. Vázquez de Aldana, "Near-infrared lasers and self-frequency-doubling in Nd:YCOB cladding waveguides," *Optics Express*, vol. 21, no. 9, p. 11562, 2013.

[105] Y. Ren, G. Brown, A. Ródenas, S. Beecher, F. Chen, and A. K. Kar, "Mid-infrared waveguide lasers in rare-earth-doped YAG," *Optics Letters*, vol. 37, no. 16, p. 3339, 2012.

[106] Y. Ren, Y. Jiao, J. R. Vazquez De Aldana, and F. Chen, "Ti:Sapphire micro-structures by femtosecond laser inscription: Guiding and luminescence properties," *Optical Materials*, vol. 58, pp. 61–66, 2016.

[107] H.-D. Nguyen, A. Ródenas, J. R. Vázquez de Aldana, J. Martínez, F. Chen, M. Aguiló, M. C. Pujol, and F. Díaz, "Heuristic modelling of laser written mid-infrared LiNbO_3 stressed-cladding waveguides," *Optics Express*, vol. 24, no. 7, p. 7777, 2016.

[108] A. E. Siegman, *Lasers*. Mill Valley, CA, 37: University science books, 1986.

[109] B. Chang, P. R. Bolton, and D. N. Fittinghoff, "Closed-form solutions for the production of ions in the collisionless ionization of gases by intense lasers," *Physical Review A*, vol. 47, pp. 4193–4203, may 1993.

[110] J. F. Bourhis, "Fibre to waveguide connection," in *Critical Review Conference on Glass Integrated Optics and optical Fiber Devices* (S. Najafi, ed.), vol. CR53, pp. 335–366, SPIE, 1994.

[111] O. G. Ramer, "Single-Mode Fiber-to-Channel Waveguide Coupling," *Journal of Optical Communications*, vol. 2, pp. 122–127, jan 1981.

[112] F. Wang, "Precision measurements for propagation properties of high-definition polymer waveguides by imaging of scattered light," *Optical Engineering*, vol. 47, no. 2, pp. 024602–0246024, 2008.

[113] M. H. Jenkins, B. S. Phillips, Y. Zhao, M. R. Holmes, H. Schmidt, and A. R. Hawkins, "Optical characterization of optofluidic waveguides using scattered light imaging," *Optics Communications*, vol. 284, no. 16-17, pp. 3980–3982, 2011.

[114] R. G. Hunsperger, *Integrated Optics: Theory and Technology*, vol. 33 of *Springer Series in Optical Sciences*. Berlin, Heidelberg: Springer Berlin Heidelberg, 1982.

[115] J. M. Senior and M. Y. Jamro, *Optical Fiber Communications: Principles and Practice*. Pearson Education, 2009.

[116] T. Calmano, J. Siebenmorgen, O. Hellmig, K. Petermann, and G. Huber, "Nd:YAG waveguide laser with 1.3 W output power, fabricated by direct femtosecond laser writing," *Applied Physics B: Lasers and Optics*, vol. 100, no. 1, pp. 131–135, 2010.

[117] K. Morishita, "Index Profiling of Three-Dimensional Optical Waveguides by the Propagation-Mode Near-Field Method," *Journal of Lightwave Technology*, vol. 4, no. 8, pp. 1120–1124, 1986.

[118] L. Mccaughan and E. E. Bergmann, "Index Distribution of Optical Waveguides from Their Mode Profile," *Journal of Lightwave Technology*, vol. 1, no. 1, pp. 241–244, 1983.

[119] M. L. Von Bibra and A. Roberts, "Refractive index reconstruction of graded-index buried channel waveguides from their mode intensities," *Journal of Lightwave Technology*, vol. 15, no. 9, pp. 1695–1699, 1997.

[120] J. Helms, J. Schmidtchen, B. Schüppert, and K. Petermann, "Error Analysis for Refractive-Index Profile Determination from Near-Field Measurements," *Journal of Lightwave Technology*, vol. 8, no. 5, pp. 625–633, 1990.

[121] K. Morishita, "Refractive-Index-Profile Determination of Single-Mode Optical Fibers by a Propagation-," *Lightwave*, vol. LT-1, no. 3, pp. 445–449, 1983.

[122] I. Mansour and F. Caccavale, "An improved procedure to calculate the refractive index profile from the measured near-field intensity," *Journal of Lightwave Technology*, vol. 14, no. 3, pp. 423–428, 1996.

[123] T. C. Sum, *Waveguide fabrication using proton beam writing*. PhD thesis, 2004.

[124] R. W. Pryor, *Multiphysics modeling using COMSOL : a first principles approach*. Sudbury, Massachustts: Jones and Barlett publishers, 2011.

[125] H. Karakuzu, M. Dubov, and S. Boscolo, "Control of the properties of micro-structured waveguides in lithium niobate crystal," *Optics Express*, vol. 21, no. 14, pp. 17122–17130, 2013.

[126] X. Song, M. Xie, F. Zhou, G. Jia, X. Hao, and S. An, "High-temperature thermal properties of yttria fully stabilized zirconia ceramics," *Journal of Rare Earths*, vol. 29, no. 2, pp. 155–159, 2011.

[127] R. N. Chan, B. R. Stoner, J. Y. Thompson, R. O. Scattergood, and J. R. Piascik, "Fracture toughness improvements of dental ceramic through use of yttria-stabilized zirconia (YSZ) thin-film coatings," *Dental Materials*, vol. 29, no. 8, pp. 881–887, 2013.

[128] J. P. Feist, P. Y. Sollazzo, S. Berthier, B. Charnley, and J. Wells, "Application of an Industrial Sensor Coating System on a Rolls-Royce Jet Engine for Temperature Detection," *Journal of Engineering for Gas Turbines and Power*, vol. 135, no. 1, p. 012101, 2012.

[129] D. Clarke and C. Levi, "Materials design for the next generation thermal barrier coatings," *Annual Review of Materials Research*, vol. 33, no. 1, pp. 383–417, 2003.

[130] D. R. Clarke and S. R. Phillpot, "Thermal barrier coating materials," *Materials Today*, vol. 8, no. 6, pp. 22–29, 2005.

[131] J. I. Eldridge, C. M. Spuckler, and J. R. Markham, "Determination of scattering and absorption coefficients for plasma-sprayed yttria-stabilized zirconia thermal barrier coatings at elevated temperatures," *Journal of the American Ceramic Society*, vol. 92, no. 10, pp. 2276–2285, 2009.

[132] N. Q. Minh, "Ceramic Fuel Cells," *Journal of the American Ceramic Society*, vol. 76, no. 3, pp. 563–588, 1993.

[133] G. R. Castillo, *Processing of ceramics using pulsed lasers.* M. sc., CICESE, 2011.

[134] Y. Damestani, C. L. Reynolds, J. Szu, M. S. Hsu, Y. Kodera, D. K. Binder, B. H. Park, J. E. Garay, M. P. Rao, and G. Aguilar, "Transparent nanocrystalline yttria-stabilized-zirconia calvarium prosthesis," *Nanomedicine: Nanotechnology, Biology, and Medicine*, vol. 9, no. 8, pp. 1135–1138, 2013.

[135] S. Casolco, J. Xu, and J. Garay, "Transparent/translucent polycrystalline nanostructured yttria stabilized zirconia with varying colors," *Scripta Materialia*, vol. 58, pp. 516–519, mar 2008.

[136] J. E. Alaniz, F. G. Perez-Gutierrez, G. Aguilar, and J. E. Garay, "Optical properties of transparent nanocrystalline yttria stabilized zirconia," *Optical Materials*, vol. 32, no. 1, pp. 62–68, 2009.

[137] Y. Jee, F. M. Becker, and M. R. Walser, "Laser-induced damage on single-crystal metal surfaces," *J. Opt. Soc. Am. B*, vol. 5, no. 3, pp. 648–659, 1988.

[138] G. Dumitru, V. Romano, H. P. Weber, M. Sentis, and W. Marine, "Femtosecond ablation of ultrahard materials," *Applied Physics A: Materials Science and Processing*, vol. 74, no. 6, pp. 729–739, 2002.

[139] J. Byskov-Nielsen, J. M. Savolainen, M. S. Christensen, and P. Balling, "Ultra-short pulse laser ablation of metals: Threshold fluence, incubation coefficient and ablation rates," *Applied Physics A: Materials Science and Processing*, vol. 101, no. 1, pp. 97–101, 2010.

[140] R. L. Sutherland, D. G. Mclean, and S. Kirkpatrick, *Handbook of Nonlinear Optics with contributions by*. New York: Marcel Dekker, second ed., 2003.

[141] F. Kajzar and J. Messier, "Third-harmonic generation in liquids," *Physical Review A*, vol. 32, no. 4, pp. 2352–2363, 1985.

[142] F. Kajzar, J. Messier, I. Girling, and I. R. Peterson, "Optical third-harmonic generation from Langmuir-Blodgett merocyanine dye thin films," *Electronic Letters*, vol. 22, no. 23, pp. 1230–1231, 1986.

[143] D. J. Hagan, J. Young, E. W. V. Stryland, and S. Member, "Degenerate Four-Wave Mixing Measurements of High Order Nonlinearities in Semiconductors," *IEEE Journal of Quantum Electronics*, vol. 27, no. October, pp. 2274–2280, 1991.

[144] I. V. Kityk, A. Fahmi, B. Sahraoui, G. Rivoire, and I. Feeks, "Nitrobenzene as a material for the fast-respond degenerate four-wave mixing," *Optical Materials*, vol. 16, no. 4, pp. 417–429, 2001.

[145] M. J. Moran, C. Y. She, and R. L. Carman, "Interferometric Measurements of the Non-linear Refractive-Index Coefficient Relative to CS2 in Laser-System-Related Materials," *IEEE Journal of Quantum Electronics*, vol. 11, no. 6, pp. 259–263, 1975.

[146] Y. J. Ding, C. L. Guo, G. A. Swartzlander, J. B. Khurgin, and A. E. Kaplan, "Spectral measurement of the nonlinear refractive index in ZnSe using self-bending of a pulsed laser beam," *Optics Letters*, vol. 15, p. 1431, dec 1990.

[147] M. Sheik-bahae, A. a. Said, T.-h. Wei, D. J. Hagan, E. W. V. Stryland, and S. Member, "Special 30th Anniversary Feature Sensitive Measurement of Optical Nonlinearities Using a Single Beam," *IEEE LEOS Newsletter*, no. February, pp. 17–26, 2007.

[148] J. T. Gopinath, M. Soljačić, E. P. Ippen, V. N. Fuflyigin, W. A. King, and M. Shurgalin, "Third order nonlinearities in Ge-As-Se-based glasses for telecommunications applications," *Journal of Applied Physics*, vol. 96, no. 11, pp. 6931–6933, 2004.

[149] M. Dinu, F. Quochi, and H. Garcia, "Third-order nonlinearities in silicon at telecom wavelengths," *Applied Physics Letters*, vol. 82, no. 18, pp. 2954–2956, 2003.

[150] R. del Coso and J. Solis, "Relation between nonlinear refractive index and third-order susceptibility in absorbing media," *Journal of the Optical Society of America B*, vol. 21, no. 3, p. 640, 2004.

[151] R. Rangel-Rojo, L. Stranges, A. K. Kar, M. A. Mendez-Rojas, and W. H. Watson, "Saturation in the near-resonance nonlinearities in a triazole-quinone derivative," *Optics Communications*, vol. 203, no. 3-6, pp. 385–391, 2002.

[152] M. J. Weber, *Handbook of optical materials*, vol. 23. New York: CRC Press LLC, 2003.

[153] R. R. Thomson, S. Campbell, I. J. Blewett, A. K. Kar, and D. T. Reid, "Optical waveguide fabrication in z-cut lithium niobate (LiNbO3) using femtosecond pulses in the low repetition rate regime," *Applied Physics Letters*, vol. 88, no. 11, pp. 28–30, 2006.

[154] C. N. Borca, V. Apostolopoulos, F. Gardillou, H. G. Limberger, M. Pollnau, and R. P. Salathé, "Buried channel waveguides in Yb-doped KY(WO4)2 crystals fabricated by femtosecond laser irradiation," *Applied Surface Science*, vol. 253, no. 19, pp. 8300–8303, 2007.

[155] F. Bain, A. Lagatsky, and R. Thomson, "Ultrafast laser inscribed Yb: KGd (WO4) 2 and Yb: KY (WO4) 2 channel waveguide lasers," *Opt. Express*, vol. 17, no. 25, pp. 3–8, 2009.

[156] J. Burghoff, H. Hartung, S. Nolte, and A. Tünnermann, "Structural properties of femtosecond laser-induced modifications in LiNbO3," *Applied Physics A*, vol. 86, pp. 165–170, nov 2006.

[157] H. Liu, J. R. Vázquez de Aldana, B. del Rosal Rabes, and F. Chen, "Waveguiding microstructures in Nd:YAG with cladding and inner dual-line configuration produced by femtosecond laser inscription," *Optical Materials*, vol. 39, pp. 125–129, jan 2015.

[158] I. Horcas, R. Fernández, J. M. Gómez-Rodríguez, J. Colchero, J. Gómez-Herrero, and a. M. Baro, "WSXM : A software for scanning probe microscopy and a tool for nanotechnology," *Review of Scientific Instruments*, vol. 78, p. 013705, jan 2007.

[159] R. He, Q. An, Y. Jia, G. R. Castillo-Vega, J. R. Vázquez de Aldana, and F. Chen, "Femtosecond laser micromachining of lithium niobate depressed cladding waveguides," *Optical Materials Express*, vol. 3, no. 9, p. 1378, 2013.

[160] H. Liu, Y. Jia, F. Chen, and J. R. Vázquez de Aldana, "Continuous wave laser operation in Nd:GGG depressed tubular cladding waveguides produced by inscription of femtosecond laser pulses," *Optical Materials Express*, vol. 3, p. 278, feb 2013.

[161] Y. Jia, J. R. Vázquez de Aldana, Q. Lu, D. Jaque, and F. Chen, "Second harmonic generation of violet light in femtosecond-laser-inscribed BiB_3O_6 cladding waveguides," *Optical Materials Express*, vol. 3, p. 1279, sep 2013.

[162] W. Nie, Y. Jia, J. R. Vázquez de Aldana, and F. Chen, "Efficient Second Harmonic Generation in 3D Nonlinear Optical-Lattice-Like Cladding Waveguide Splitters by Femtosecond Laser Inscription," *Scientific Reports*, vol. 6, p. 22310, apr 2016.

[163] G. Salamu and N. Pavel, "Power scaling from buried depressed-cladding waveguides realized in Nd:YVO4 by femtosecond-laser beam writing," *Optics & Laser Technology*, vol. 84, pp. 149–154, oct 2016.

[164] N. Pavel, G. Salamu, F. Jipa, and M. Zamfirescu, "Diode-laser pumping into the emitting level for efficient lasing of depressed cladding waveguides realized in Nd:YVO_4 by the direct femtosecond-laser writing technique," *Optics Express*, vol. 22, p. 23057, sep 2014.

[165] A. Okhrimchuk, V. Mezentsev, A. Shestakov, and I. Bennion, "Low loss depressed cladding waveguide inscribed in YAG:Nd single crystal by femtosecond laser pulses," *Optics Express*, vol. 20, p. 3832, feb 2012.

[166] H. Liu, F. Chen, J. R. Vázquez de Aldana, and D. Jaque, "Femtosecond-laser inscribed double-cladding waveguides in Nd:YAG crystal: a promising prototype for integrated lasers," *Optics Letters*, vol. 38, p. 3294, sep 2013.

[167] N. Pavel, G. Salamu, F. Voicu, F. Jipa, M. Zamfirescu, and T. Dascalu, "Efficient laser emission in diode-pumped Nd:YAG buried waveguides realized by direct femtosecond-laser writing," *Laser Physics Letters*, vol. 10, p. 095802, sep 2013.

[168] H. Liu, Y. Jia, J. R. Vázquez de Aldana, D. Jaque, and F. Chen, "Femtosecond laser inscribed cladding waveguides in Nd:YAG ceramics: fabrication, fluorescence imaging and laser performance.," *Optics express*, vol. 20, pp. 18620–9, aug 2012.

[169] Y. Jia, C. Cheng, J. R. Vázquez de Aldana, G. R. Castillo, B. d. R. Rabes, Y. Tan, D. Jaque, and F. Chen, "Monolithic crystalline cladding microstructures for efficient light guiding and beam manipulation in passive and active regimes," *Scientific Reports*, vol. 4, p. 5988, may 2015.

[170] Y. Jia, C. Cheng, J. R. Vazquez de Aldana, and F. Chen, "Three-Dimensional Waveguide Splitters Inscribed in Nd:YAG by Femtosecond Laser Writing: Realization and Laser Emission," *Journal of Lightwave Technology*, vol. 34, pp. 1328–1332, feb 2016.

[171] P. Russell, "Photonic Crystal Fibers," *Science*, vol. 299, no. 2003, pp. 358–362, 2003.

[172] H.-K. Hsiao, K. A. Winick, J. D. Monnier, and J.-P. Berger, "An infrared integrated optic astronomical beam combiner for stellar interferometry at 3-4 μm," *Optics Express*, vol. 17, p. 18489, oct 2009.

[173] A. Ródenas, G. Martin, B. Arezki, N. Psaila, G. Jose, A. Jha, L. Labadie, P. Kern, A. Kar, and R. Thomson, "Three-dimensional mid-infrared photonic circuits in chalcogenide glass," *Optics Letters*, vol. 37, no. 3, p. 392, 2012.

[174] R. R. Thomson, R. J. Harris, T. A. Birks, G. Brown, J. Allington-Smith, and J. Bland-Hawthorn, "Ultrafast laser inscription of a 121-waveguide fan-out for astrophotonics," *Optics Letters*, vol. 37, p. 2331, jun 2012.

[175] T. A. Birks, I. Gris-Sánchez, S. Yerolatsitis, S. G. Leon-Saval, and R. R. Thomson, "The photonic lantern," *Advances in optics and photonics*, vol. 7, pp. 107–167, aug 2015.

[176] J. Martínez García, *Mid-infrared integrated photonic sensors of water and ice films for harsh environments*. Ph.d., Universitat Rovira i Virgili, 2017.

[177] J. E. McCarthy, H. T. Bookey, N. D. Psaila, R. R. Thomson, and A. K. Kar, "Mid-infrared spectral broadening in an ultrafast laser inscribed gallium lanthanum sulphide waveguide," *Optics Express*, vol. 20, pp. 1545–1551, jan 2012.

[178] G. Demetriou, J.-P. Bérubé, R. Vallée, Y. Messaddeq, C. R. Petersen, D. Jain, O. Bang, C. Craig, D. W. Hewak, and A. K. Kar, "Refractive index and dispersion control of ultrafast laser inscribed waveguides in gallium lanthanum sulphide for near and mid-infrared applications," *Optics Express*, vol. 24, no. 6, p. 6350, 2016.

[179] L. Lepetit, G. Chériaux, and M. Joffre, "Linear techniques of phase measurement by femtosecond spectral interferometry for applications in spectroscopy," *Journal of the Optical Society of America B*, vol. 12, p. 2467, dec 1995.

[180] D. Kane and R. Trebino, "Characterization of arbitrary femtosecond pulses using frequency-resolved optical gating," *IEEE Journal of Quantum Electronics*, vol. 29, no. 2, pp. 571–579, 1993.

[181] C. Iaconis and I. A. Walmsley, "Spectral phase interferometry for direct electric-field reconstruction of ultrashort optical pulses," *Optics Letters*, vol. 23, p. 792, may 1998.

[182] B. Alonso, Í. J. Sola, Ó. Varela, J. Hernández-Toro, C. Méndez, J. San Román, A. Zaïr, and L. Roso, "Spatiotemporal amplitude-and-phase reconstruction by Fourier-transform of interference spectra of high-complex-beams," *Journal of the Optical Society of America B*, vol. 27, p. 933, may 2010.

[183] B. Alonso Fernández, *Spatio temporal characterization of ultrashort laser pulses*. Phd, Universidad de Salamanca, 2012.

[184] B. Alonso, Í. J. Sola, Ó. Varela, C. Méndez, I. Arias, J. San Román, A. Zaïr, and L. Roso, "Spatio-temporal characterization of laser pulses by spatially resolved spectral interferometry," *Optica Pura y Aplicada*, vol. 43, no. 1, pp. 1–7, 2010.

[185] J. Burghoff, S. Nolte, and A. Tünnermann, "Origins of waveguiding in femtosecond laser-structured LiNbO3," *Applied Physics A*, vol. 89, pp. 127–132, aug 2007.

Appendix A

Resumen en castellano

Microprocesado de dieléctricos transparentes con pulsos ultracortos. Nuevos esquemas de fabricación de dispositivos fotónicos

A.1   Resumen

El microprocesado de materiales transparentes con pulsos láser ultracortos ha atraído un creciente interés en la investigación debido a las propiedades únicas de la interacción láser-materia a escalas de tiempo ultracortas. En particular, la posibilidad de producir modificaciones locales controladas del índice de refracción en dieléctricos abrió la puerta a la microfabricación 3D de circuitos fotónicos integrados. En este trabajo se presentan nuevas estrategias para la optimización de las técnicas para la fabricación de guías de ondas ópticas en materiales cristalinos, así como para su caracterización. El uso de estas estrategias es una contribución al desarrollo tecnológico para la fabricación de dispositivos fotónicos complejos. Las estructuras fotónicas fabricadas están basadas en modificaciones Tipo II en cristales, en este contexto distintas técnicas tales como *Guias con estrés inducido* y *Guias depressed cladding* fueron utilizadas. En el caso de las guías de onda con estrés inducido, se utilizó un nuevo esquema de fabricación en el que se utilizó un interferómetro para generar dos haces láser de femtosegundos que, enfocados con cierta separación lateral dentro del cristal, producen simultáneamente dos tracks de daño con un solo barrido. Por otra parte, se presenta la fabricación de arreglos de guías de onda basados en guías depressed cladding. Los arreglos consisten en guías de ondas hexagonales divergentes entre sí y con distintas separaciones entre ellas a la salida del cristal. Los resultados muestran un rendimiento óptimo de las estructuras fabricadas y sugieren un

uso potencial en aplicaciones fotónicas tales como linternas fotónicas, las cuales pueden ser fácilmente implementadas en otros materiales transparentes. También se presenta un nuevo tipo de estructuras llamadas guías con estructura fotónica que emulan en forma, a las fibras de cristal fotónico. Estas estructuras presentan características atractivas tales como el hecho de poder manipular su sección transversal a lo largo de la guía de onda introduciendo defectos axiales que permitan la manipulación del haz de una manera controlada y reproducible. Esta importante característica ofrece la posibilidad de fabricar estructuras monolíticas. También se presenta un estudio de las modificaciones inducidas por pulsos de femtosegundos en la cerámica nanoestructurada YSZ, un material prometedor para aplicaciones biomédicas, así como el estudio y la integración de guías de ondas ópticas en este material. Además, se caracterizaron propiedades tales como el umbral de ablación y las propiedades ópticas no lineales. Finalmente, se presenta un estudio preliminar de las características temporales pulsos ultracortos al propagarse en distintos tipos de guías de onda.

A.2   Introducción

A.2.1   Microprocesado de materiales con pulsos láser ultracortos

El microprocesado con pulsos láser ultracortos es un proceso mediante el cual los pulsos de un láser de femtosegundos, son utilizados para micro-estructurar la superficie o el interior de materiales sólidos. Una de las características más interesantes de este tipo de láseres son las altas intensidades pico que pueden alcanzar al ser enfocados. Estas intensidades generalmente están en el rango de 10^{12} - 10^{15} W/cm^2 con lo cual es posible inducir fácilmente absorción no lineal en materiales transparentes. Por lo tanto, si el haz láser es enfocado dentro de un material transparente (véase Fig. A.1), la absorción no lineal queda limitada a una pequeña región entorno al foco, permitiendo modificaciones de muy alta precisión y procesado 3D del material [1]. En particular, la interacción de pulsos de femtosegundos con dieléctricos transparentes ha generado gran interés en las dos últimas décadas debido principalmente al hecho poder inducir cambios localizados en el índice de refracción permitiendo la fabricacion de estructuras fotónicas complejas dentro del material sin dañar su superficie [2–14]. Hoy en día, esta técnica es conocida como **Inscripción laser ultrarrápida** (ULI) y se ha consolidado como una tecnología de fabricación de dispositivos fotónicos tridimensionales (3D).
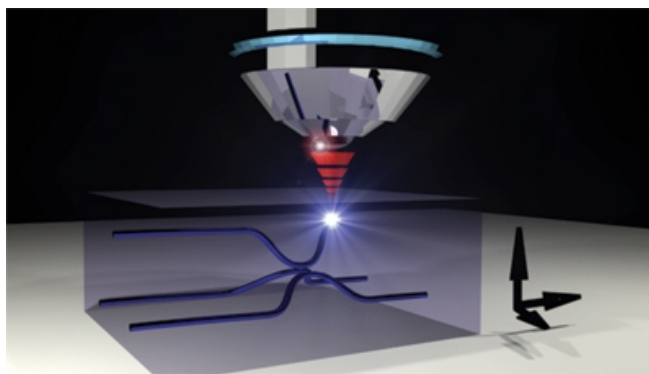
Fig. A.1 Imagen esquemática del proceso de inscripción láser ultrarrápido; La absorción no lineal ocurre en el foco del láser, dando como resultado un depósito de energía altamente localizado. Esto permite la fabricación de estructuras fotónicas 3D de un material transparente.[15].

A.2.2   Motivación y antecedentes

La inscripción láser ultrarrápida se caracteriza por una transferencia de energía del campo óptico intenso láser al material a través de un proceso conocido como optical breakdown [16]

el cual provoca la ionización de un gran número de electrones. Como resultado, la energía adquirida por los electrones es transferida al material. A medida que esta energía es depositada y convertida en energía térmica, el material puede experimentar modificaciones estructurales o de fase, dejando detrás cambios localizados tales como el índice de refracción. La inscripción láser ultrarrápida se caracteriza por una transferencia de energía del campo óptico intenso láser al material a través de un proceso conocido como optical breakdown[16] el cual provoca la ionización de un gran número de electrones. Como resultado, la energía adquirida por los electrones es transferida al material. A medida que esta energía es depositada y convertida en energía térmica, el material puede experimentar modificaciones estructurales o de fase, dejando detrás cambios localizados tales como el índice de refracción. Este principio fue utilizado por el grupo de Hirao en Japón [2] para fabricar por primera vez una guía de onda óptica en el interior de un material transparente utilizando pulsos láser de femtosegundos. Para ello, enfocaron el haz láser dentro de una muestra de vidrio y ésta fue trasladada con respecto al foco, generando así un canal en el cual se había conseguido un contraste positivo del índice de refracción, y en el que la luz podía ser acoplada y propagada. Desde este trabajo pionero, la inscripción láser ultrarrápida se extendió a una gran variedad de materiales transparentes [17–24]. Desde entonces la investigación y el desarrollo con respecto a la fabricación de dispositivos fotónicos basados en guías de onda ópticas ha avanzado rápidamente hasta hoy.

En general, existen dos tipos principales de modificaciones en dieléctricos transparentes mediante la irradiación con pulsos femtosegundos que pueden ser utilizadas para la fabricación de guías de ondas. En el primero, el cambio del índice de refracción se crea justo en el volumen de enfoque del haz incidente. Esta modificación fue la primera en ser investigada y, en general, requiere el uso de energías de pulso bajas (unos pocos nJ), por lo tanto puede ser llevado a cabo sólo con el uso de un oscilador de femtosegundos [6]. Cabe mencionar que esta es la técnica común para la fabricación de guías de onda en vidrios. Las guías de onda fabricadas por esta técnica han sido utilizadas para la implementación de dispositivos complejos tales como arreglos de guías de onda acopladas, [26] o redes de Bragg [27]. El segundo tipo de modificacion implica el uso de pulsos láser amplificados con energía típicamente del orden de μJ. En este caso se produce un track de daño severo a lo largo del volumen de enfoque que induce una disminución del índice de refracción sobre el mismo. Además, se induce un aumento local del índice de refracción en la zona circundante al daño. Este aumento puede ser fácilmente manipulado haciendo una segunda irradiación a unas cuantas micras de la primera. Como resultado, el cambio del índice de refracción puede ser incrementado o manipulado fácilmente. Esta técnica es utilizada para la fabricación de guías de ondas en cristales. Este tipo de modificacion se utiliza especialmente para la fabricación de dispositivos activos [25] con características atractivas como el hecho de preservar las propiedades espectrales y anisotrópicas

del material [28, 29] así como la resistencia a altas temperaturas [30]. Este tipo de modificación también es utilizada para la fabricación de las denominadas guías de onda de depressed cladding. Para este tipo de guías, se realizan un gran número de irradiaciones paralelas entre sí, delimitando un área del material que no es irradiado y donde el área irradiada actúa como una barrera para la luz [31]. La Fig. A.2 muestra algunas guías de onda fabricadas con distintos tipo de modificaciones inducidas por láser de femtosegundos. Los mecanismos responsables de la inscripción láser ultrarrápida, así como sus propiedades ópticas, dependen de las propiedades del material y de las condiciones de irradiación, tales como la energía por pulso, duración del pulso, tasa de repetición, polarización, condiciones de enfoque y velocidad de traslación. Todos estos parámetros pueden ser optimizados para fabricar el tipo de guía de onda deseado con ciertas propiedades, es decir, si la guía es mono/multi modo, contraste de índice de refracción, o pérdidas ópticas [32].
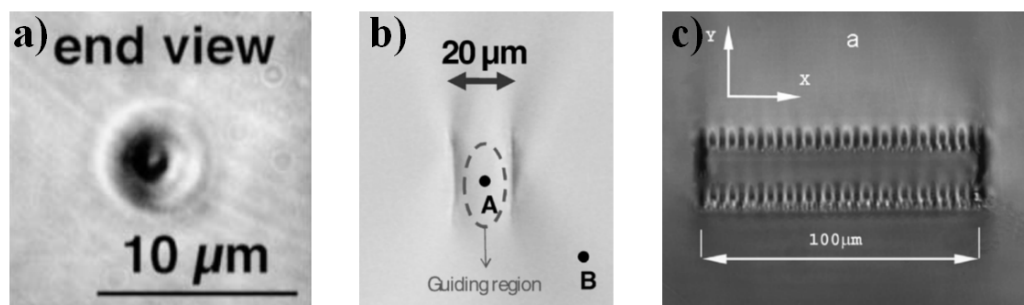
Fig. A.2 Micrografía óptica de la sección transversal de guías de onda fabricadas utilizando distintos tipos modificaciones inducidas por láser de femtosegundos. a) Guía de onda fabricada en vidrio utilizando un oscilador de femtosegundos (pulsos sin amplificar) [33]. b) Guía de onda fabricada con pulsos amplificados en una cerámica transparente utilzando dos track de daño parallelos [34]. c) Guía depressed cladding fabricada en un cristal de Nd:YAG utilizando varios tracks de daño en paralelo [31].

Hoy en día, la inscripción láser ultrarrápida (ULI) se ha establecido como una de las técnicas más rápidas y eficientes para la fabricación de estructuras 3D en materiales transparentes [35–41], lo cual es imposible realizar con cualquier otra técnica convencional basada en procesos fotolitográficos [23]. En este sentido, el proceso ULI presenta algunas ventajas en comparación con las técnicas estándar, por ejemplo, es un proceso de un solo paso que no requiere el uso de plantillas o post-procesado para su desarrollo. A pesar del hecho de que la mayor parte de las estructuras fotónicas fabricadas por ULI no presenten aún los altos estándares de calidad obtenidos por los métodos tradicionales, debe destacarse que ULI ofrece características importantes y atractivas, siendo una de las más interesantes la posibilidad de fabricar o inscribir de manera directa prácticamente cualquier microestructura 3D en cualquier

profundidad de la muestra. Además, también es posible inscribir estructuras con distintas funcionalidades integradas como una estructura monolítica. Además, en los últimos años, ULI también ha sido empleado como una herramienta importante para la fabricación de componentes optofluídicos diseñados en arquitecturas compactas para aplicaciones de laboratorio en un chip [42]. Las ventajas de la capacidad de inscripción 3D hacen de ULI una técnica de fabricación importante con impacto en una amplia variedad de aplicaciones en diferentes áreas que van desde la astrofotónica, las telecomunicaciones ópticas, la biofotónica, la óptica cuántica y el procesamiento de la información [43–45]. Se ha comprobado que ULI es un método excelente para la fabricación de guías de onda en una amplia gama de materiales, incluyendo cristales, cerámicas y polímeros orgánicos.

Existe una gran cantidad de trabajos reportados sobre la fabricacion de dispositivos pasivos fabricados por ULI, haciendo uso de la capacidad de fabricación en 3D. Algunos de estos dispositivos son, por ejemplo, divisores de potencia [46, 47], acopladores [6, 48], interferómetros Mach-Zehnder [7, 49] o redes de Bragg [50]. Hoy en día, se han desarrollado una gran variedad de trabajos interesantes en dieléctricos transparentes que implementan múltiples geometrías y configuraciones que ofrecen una amplia gama de posibilidades para aplicaciones versátiles en diversas áreas de interés. Algunos de estos interesantes trabajos son por ejemplo, láseres de onda continua o pulsados [53–55], amplificadores ópticos [56, 57], chips microfluídicos [58, 59] y dispositivos fotónicos cuánticos [60].

En resumen, las estructuras fotónicas 3D en materiales transparentes fabricados por ULI son una parte esencial de una gran variedad de dispositivos fotónicos, importantes para aplicaciones en distintas áreas de interes. La posibilidad de confinar la luz y fabricar dispositivos fotónicos activos (como láseresde guía de onda o convertidores de frecuencia) integrados en este tipo de materiales, permite el diseño de experimentos compactos, hasta hace poco insospechados. Por otra parte, cabe señalar que, aunque los fundamentos de ULI son bien conocidos y han sido ampliamente estudiados en la literatura, queda mucho trabajo por hacer en términos de optimización de las técnicas de fabricación de guías de onda, así como el desarrollo tecnológico para la fabricación de dispositivos complejos. El presente trabajo aporta nuevos conocimientos en ambos aspectos

A.3 Metodología

En general, la fabricación de las guías de onda se realizó en primer lugar, probando el efecto de la irradiación láser a diferentes energías por pulso, profundidad de la muestra y condiciones de enfoque (apertura numérica). Una vez que estas pruebas se realizaron y analizaron con distintas técnicas de microscopía, las guías de ondas se produjeron utilizando los parámetros

más apropiados de acuerdo al tipo de técnica de fabricación a utilizar. Después de fabricar las guías de onda, se analizaron sus propiedades acoplando un láser de baja potencia, con el que se tomaron imágenes de los modos confinados. Para el acoplamiento de pulsos ultracortos en las guías de onda, fue necesario cambiar la óptica de enfoque y configurar un sistema específico. En cuanto a los estudios sobre cada material específico, la variación de los parámetros del láser tales como la energía por pulso, el tamaño del haz y la velocidad de barrido permitieron inducir cambios en las propiedades ópticas del material tales como el índice de refracción. Una vez identificados los parámetros de irradiación, se fabricaron estructuras de guías de onda en distintos dieléctricos transparentes tales como cristales y cerámicas.

A.4 Objectivos

Los objetivos principales de este trabajo de tesis son los siguientes:

- *Avanzar en las técnicas de microfabricación de guías de onda en materiales ópticos que son actualmente el "estado del arte" en este campo.*

- *Proponer y demostrar nuevos esquemas de fabricación e integración de elementos fotónicos en materiales ópticos, entre los que se encuentran vidrios, cristales y cerámicas.* Se proponen nuevas geometrías y técnicas de estructuración que mejoren ciertas propiedades de las guías de onda, como la potencia máxima soportada, pérdidas, o calidad del perfil modal.

- *Diseñar y analizar la posibilidad de fabricar dispositivos tipo guía de onda para su aplicación en el ámbito de los láseres de pulsos cortos.* Las guías de onda integradas en materiales ópticos se han utilizado fundamentalmente en el régimen continuo o de pulsos largos, pero existen muy pocos estudios sobre las posibilidades que ofrecen en el control de pulsos de femtosegundos. En este objetivo se pretende estudiar el comportamiento de las guías de onda al acoplar pulsos de femtosegundos, así como las propiedades ópticas no lineales de las mismas

- *Estudiar las modificaciones inducidas por pulsos de femtosegundos en la cerámican nanoestructurada YSZ, así como el estudio y la integración de guías de ondas ópticas en este material.* Esta cerámica tiene una gran variedad de aplicaciones en ambientes exigentes y sólo recientemente se ha considerado para aplicaciones ópticas. En este trabajo, además de la inscripción láser ultrarrápida de guías de onda en este material se presenta una caracterización de sus propiedades ópticas ópticas no lineales.

A.5   Organización de la tesis

Esta tesis se compone de siete capítulos,

En el *Capítulo 2* se discuten los conceptos básicos del microprocesado de materiales con pulsos láser ultracortos. Se describe el arreglo experimental básico para dicho procesado y se describen además las diferencias básicas entre el microprocesado con pulsos de larga duración (ns) y pulsos ultra-cortos (ps-fs), así como los mecanismos físicos implicados en la interacción. Además, se presentan las distintas técnicas para la fabricación de dispositivos fotónicos utilizando pulsos ultracortos.

En el *Capítulo 3* se presentan las técnicas experimentales utilizadas durante el desarrollo de esta tesis. Estas incluyen el montaje experimental para la fabricación de las guías de onda, así como las configuraciones y técnicas necesarias para la caracterización de las guías de ondas fabricadas.

El *Capítulo 4* presenta un estudio de la respuesta de la cerámica nanoestructurada YSZ a la irradiación con pulsos láser ultracortos. Se presenta un estudio de sus propiedades de micromecanizado así como un análisis de sus propiedades ópticas no lineales. Además, se presenta también un estudio sobre la fabricación de guías de onda en este material con el fin de determinar sus características para ser utilizadas como material óptico.

En general, el *Capítulo 5* presenta los resultados y el análisis relacionados con nuevos esquemas para la fabricación e implementación de dispositivos fotónicos fabricados en dieléctricos transparentes por irradiación con pulsos láser de femtosegundos. En particular, se presentan la técnica de irradiación simultánea con dos haces laser, arreglos de guías de onda tipo depressed cladding y guías de onda con estructura fotonica.

El *Capítulo 6* analiza el efecto de los pulsos láser ultracortos sobre las guías de onda fabricadas. En este capítulo, se propone un sistema para caracterizar la propagación de pulsos láser ultracortos (espectra y temporalmente) a través de guías de ondas fabricadas por láser de femtosegundos analizando las propiedades de dispersión.

Finalmente, en el *Capítulo 7* se reportan las conclusiones generales sobre este trabajo de tesis.

A.6   Resultados y conclusiones

En resumen, este trabajo se ha centrado en el desarrollo e implementación de nuevas estrategias para la fabricación de guías de ondas ópticas en cristales dieléctricos transparentes por inscripción directa con láser de femtosegundos. Se han propuesto y demostrado nuevos esquemas para la fabricación e integración de estructuras fotónicas en materiales ópticos, tales como cristales y cerámicas. Estos nuevos esquemas mejoran con éxito ciertas propiedades de las guías de onda fabricadas con técnicas "estándar", tales como pérdidas de propagación, calidad del perfil modal o capacidades de fabricación en 3D. Las conclusiones generales de la presente tesis se presentan a continuación.

- Se propuso una nueva técnica para la fabricación de guías de ondas inducidas por estrés mecánico. La configuración se basó en un interferómetro que permitió igualar la energía de dos haces. Las guías de ondas fabricadas con esta tecnica en Nd: YAG, se compararon con las fabricadas con la técnica estándar de "doble línea" y los perfiles modales, así como las propiedades ópticas fueron distintas en ambos casos. La caracterización por micro-luminiscencia de las guías de onda mostró que el campo estrés mecánico inducido con irradiación simultánea de dos haces era simétrico, lo que resultó en perfiles modales simétricos, guías monomodo y mayores modos en todas las condiciones de irradiación estudiadas. Además, las guías de onda fabricadas por irradiación simultánea de doble haz presentaron una reducción significativa de las pérdidas de propagación.

- Con respecto a las guías de onda tipo depressed cladding, se diseñaron y fabricaron con éxito arreglos 3D de guías de onda hexagonales por inscripción láser ultrarrápida. La caracterización óptica de las guías reveló una compleja propagación multimodo en el rango visible, y un comportamiento cercano al monomodo para el NIR. No se encontraron efectos apreciables de las pérdidas de propagación en la curvatura de las guías las cuales fueron medidas en cada una de las guías de onda de los arreglos 3D. En este caso, los mapas de micro-luminiscencia mostraron que el daño inducido durante la fabricación de las guías de ondas se concentró en los tracks, mientras que un campo de estrés y deformación residual afectó a áreas mayores de las estructuras debido a los parámetros láser de la inscripción. Los resultados de la caracterización sugieren que este tipo de estructuras podrían ser usadas como linternas fotónicas o incluso para otros circuitos fotónicos 3D complejos.

- Se ha diseñado y fabricado un nuevo tipo de guías de onda con estructura de fotonica que emula en forma a las fibras de cristal fotónico. La versatilidad de estas estructuras ha sido demostrada introduciendo varios defectos axiales que actúan como núcleo de la guía.

En este tipo de guías, el haz de entrada puede ser convertido en multiples haces de salida, así como realizar modificaciones del perfil modal. Por otra parte, se probó la capacidad de las estructuras hexagonales para la fabricación en 3D mediante el diseño de guías de onda con un núcleo de mayor tamaño, éstas fueron probadas con éxito como guías de onda con interacción de superficie. Las estructuras fabricadas en este trabajo presentan propiedades ópticas similares, tales como pérdidas de propagación, dependencia de la polarización y contraste del índice de refracción. Además, debe destacarse que este tipo de guías de onda permite la manipulación del haz modificando la sección transversal de las guías a lo largo de toda la estructura. Esta característica proporciona un método atractivo para fabricar microestructuras monolíticas con diversos dispositivos fotónicos integrados en una sola estructura.

- Se ha llevado a cabo un estudio novedoso sobre el efecto en las características temporales de pulsos ultracortos al propagarse en guías de onda fabricadas en un cristal de YAG por irradiación directa con láser de femtosegundos. Para el estudio, se fabricaron guías de onda con geometría y tamaño diversos. Las mediciones preliminares sugieren, como resultado más relevante, que en las guías de onda con estructuras fotónica las características temporales de los pulsos propagados no se ven afectadas, compensando de alguna manera el efecto dispersivo del material. Cabe destacar que todavía deben realizarse simulaciones numéricas con el fin de confirmar y comprender este efecto.

- Con respecto a la irradiación con pulsos láser ultracortos de la cerámica nanoestructurada YSZ, la cual es un material interesante para la integración de dispositivos fotónicos en aplicaciones biomédicas, se determinaron parámetros tales como el umbral de ablación, el coeficiente de incubación, el umbral de single-shot y la tasa de ablación. Tales parámetros son necesarios para el micro-mecanizado eficiente de la cerámica con láseres de femtosecondos. Por otro lado, las propiedades ópticas no lineales de la cerámica YSZ también se estimaron mediante la técnica de Z-scan. Se encontró una dependencia inversa entre la concentración de vacancias de oxígeno en la cerámica y los coeficientes ópticos no lineales. También se estimaron los componentes de la susceptibilidad óptica de tercer orden. Finalmente, se demostró que es posible fabricar guías de ondas ópticas en la cerámica YSZ mediante la irradiación láser de femtosegundos. El análisis micro-Raman de los tracks y sus alrededores, reveló que la naturaleza cristalina y la fase de la cerámica YSZ no se ven comprometidos por la interacción láser lo cual es también una característica importante para el uso potencial de este material como host para láseres de guía de onda.